Aus dem

Pathologischen Institut

Institut der Ludwig-Maximilians-Universität München

Direktor: Prof. Dr. Frederick Klauschen

Phenomics and Transcriptomics of the Hematopoietic Niche for Understanding Malignant Transformation in GATA2 Deficiency

Dissertation
zum Erwerb des Doktorgrades der Naturwissenschaften
an der Medizinischen Fakultät der
Ludwig-Maximilians-Universität München

vorgelegt von
Franziska Elisabeth Schreiber-Teichert

aus
München

Jahr
2024

Mit Genehmigung der Medizinischen Fakultät
der Ludwig-Maximilians-Universität München

Betreuer:	Prof. Dr. Andreas Jung
Zweitgutachter:	Prof. Dr. Roland Kappler
Dekan:	Prof. Dr. med. Thomas Gudermann
Tag der mündlichen Prüfung:	02. Februar 2026

Contents

Zusammenfassung

Die GATA2 Defizienz bei Kindern ist eine komplexe Multisystemerkrankung mit einem erhöhten Risiko für die Entstehung eines myelodysplastischen Syndroms (MDS) und Progression zur akuten myeloischen Leukämie. Bei der Behandlung von Patienten mit GATA2 Defizienz stellt das begrenzte Verständnis von Mechanismen der malignen Transformation eine große Herausforderung dar und erschwert fundierte therapeutische Entscheidungen. Die Notwendigkeit, zwischen raschem Fortschreiten und stabiler Krankheit zu unterscheiden, unterstreicht den Bedarf für weitere Forschung zur Ermittlung von Einflussfaktoren auf den Krankheitsverlauf.

Diese Arbeit untersucht systematisch potenzielle Mechanismen der Transformation bei pädiatrischem MDS in Verbindung mit GATA2 Defizienz. Wir charakterisieren Knochenmarksbiopsien von 57 Kindern mit refraktärer Zytopenie des Kindesalters oder MDS mit Blastenüberschuss, mit und ohne GATA2 Mutationen, anhand quantitativer und qualitativer Analyse von Multiplex Immunfluoreszenz, traditioneller Immunhistochemie, Genexpressionsanalyse und RNA-*in situ* Hybridisierung.

Durch umfassende Analyse der Hämatopoese, der hämatopoetischen Nische, ihrer Mikroumgebung und ihres Transkriptoms trägt unsere Studie zu einem ganzheitlicheren Verständnis der Krankheit bei. Wir identifizieren erhöhte Histon Trimethylierung und deregulierte Apoptose als potenzielle Triebkräfte der malignen Transformation und bieten damit eine Grundlage für den Einsatz von Venetoclax und Azacitidin zur Behandlung von Patienten mit fortgeschrittener GATA2 Defizienz. Darüber hinaus bilden unsere Ergebnisse einen Rahmen für die weitere Erforschung des Zusammenspiels zwischen Immunantwort und Inflammation, indem sie die Induktion von NLRP3 und TIM-3 bei fortgeschrittener GATA2 Defizienz aufzeigen.

Zusammenfassend lässt sich sagen, dass diese Studie unser Verständnis der pädiatrischen GATA2 Defizienz erheblich erweitert und wertvolle Erkenntnisse zur Optimierung von Diagnose- und Therapiestrategien liefert. Diese Beobachtungen ermöglichen die Anpassung von Therapien und können einen Beitrag zur Verbesserung der Patientenversorgung liefern.

Abstract

Pediatric GATA2 deficiency is a complex, multisystem disorder with an elevated risk of developing myelodysplastic syndrome (MDS) and progression to acute myeloid leukemia. The limited understanding of mechanisms driving malignant transformation poses a significant challenge in managing patients with GATA2 deficiency, hindering informed therapeutic decisions. The imperative to distinguish between rapid progression and stable disease emphasizes the need for further research to elucidate factors influencing disease trajectory.

This thesis systematically investigates potential mechanisms driving transformation in pediatric MDS linked to GATA2 deficiency. Employing quantitative and qualitative analyses of data from multiplex immunofluorescence, traditional immunohistochemistry, gene expression profiling, and RNA-*in situ* hybridization, we characterize bone marrow biopsies from 57 children with refractory cytopenia of childhood or MDS with excess blasts, with and without GATA2 mutations.

By comprehensively integrating data from the hematopoiesis, the hematopoietic niche, its microenvironment, and transcriptome, our study contributes to a more holistic understanding of the disease. We identify increased histone trimethylation and deregulated apoptosis as potential drivers of malignant transformation, offering a foundation for utilizing venetoclax and azacitidine in the treatment of patients with advanced GATA2 deficiency. Additionally, our findings establish a framework for advancing research on the interplay between immune response and inflammation, by revealing the induction of NLRP3 and TIM-3 in advanced GATA2 deficiency.

In summary, this research significantly advances our understanding of pediatric GATA2 deficiency, offering valuable insights for refining diagnostic and therapeutic strategies. These observations facilitate the customization of therapies, with the potential to contribute to improved patient care.

List of Figures

List of Tables

List of Abbreviations

The following table presents an alphabetical list of all abbreviations used throughout this work.

Table 1: List of abbreviations.

Abbreviation	Description
µL	Microliter(s)
µm	Micrometer(s)
µM	Micromolar
®	Registered trademark
™	Trademark
AML	Acute myeloid leukemia
APS	Ammonium peroxydisulphate
ASC	Apoptosis-associated speck-like protein
AZA	Azacitidine
BCL2	BCL2 apoptosis regulator
Bcl-XL	BCL2 like 1
BSA	Bovine serum albumin
CASP1	Caspase 1
CASP3	Caspase 3
CCL18	C-C motif chemokine ligand 18
CD117	KIT proto-oncogene, receptor tyrosine kinase
CD123	Interleukin 3 receptor subunit alpha
CD14	CD14 molecule
CD163	CD163 molecule
CD20	Membrane spanning 4-domains A1
CD3	CD3 epsilon subunit of T cell receptor complex
CD34	CD34 molecule

CD42b	Glycoprotein Ib platelet subunit alpha
CD71	Transferrin receptor
CD8	CD8 subunit alpha
CO_2	Carbon dioxide
CTLA-4	Cytotoxic T lymphocyte antigen 4
DAB	Diaminobenzidine
DAPI	4,6-Diamidino-2-phenylindole
ddH_2O	Bidestilled water
DMSO	Dimethyl sulfoxide
DTT	Dithiothreitol
E-Cadherin	Cadherin 1
EPX	Eosinophil peroxidase
EZH2	Enhancer of zeste 2 polycomb repressive complex 2 subunit
FFPE	Formalin-fixed, paraffin-embedded
FOXP3	Forkhead box P3
g	Gramm(s)
GATA2	GATA binding protein 2
GATA2-EB	MDS-EB with $GATA2^{mut}$
$GATA2^{mut}$	GATA2 mutation
GATA2-RCC	RCC with $GATA2^{mut}$
$GATA2^{WT}$	GATA2 wild-type
GSDMD	Gasdermin D
h	Hour(s)
H_2O_2	Hydrogen peroxide
H3K27me3	Trimethylation of histone H3 at lysine 27
HRP	Horseradish peroxidase
HSC(s)	Hematopoietic stem cell(s)
IκBα	NFKB inhibitor alpha
ICC	International Consensus Classification

IDO	Indoleamine 2,3 dioxygenase
IHC	Immunohistochemistry
IKZF1	Ikaros family zinc finger 1
IL18	Interleukin 18
IL1B	Interleukin 1 beta
kDa	Kilo Dalton
Ki-67	Marker of proliferation Ki-67
L	Liter(s)
LCTF	Liquid crystal tunable filter
LAG-3	Lymphocyte activation gene 3 protein
LYL1	LYL1 basic helix-loop-helix family member
M	Molar
mA	Milli ampere
MCL1	MCL1 apoptosis regulator, BCL2 family member
MCT	Tryptase alpha/beta 1 (alias mast cell tryptase)
MDS	Myelodysplastic syndrome(s)
MDS-EB	Myelodysplastic syndrome with excess blasts
mg	Milligrams
mIF	Multiplex immunofluorescence
min	Minute(s)
mL	Milliliter(s)
mM	Millimolar
MPO	Myeloperoxidase
MSI	Multispectral image
n	Number, amount
NLRP3	NLR family pyrin domain containing 3
PBS	Dulbecco's Phosphate Buffered Saline
PD-1	Programmed cell death 1

PLIN1	Perilipin 1
PMA	Phorbol 12-myristate 13-acetate
PMSF	Phenylmethylsulfonyl fluoride
ProTaqs I	ProTaqs Antigen Enhancer I, pH 6.0
PVDF	Polyvinylidene difluoride
RCC	Refractory cytopenia of childhood
Rpm	Rounds per minute
RT	Room temperature
RUNX1	RUNX family transcription factor 1
S100A8	S100 calcium binding protein A8
S100A9	S100 calcium binding protein A9
SAMD9	Sterile alpha motif domain containing 9
SAMD9L	Sterile alpha motif domain containing 9 like
SCF	KIT ligand (alias stem cell factor)
SD	Standard deviation
SDS	Sodium dodecyl sulfate
TIM-3	Hepatitis A virus cellular receptor-2 (alias T cell immunoglobulin and mucin domain 3)
TdT	DNA nucleotidylexotransferase
TEMED	N,N,N‘,N‘-tetramethylethylenediamine
TRS6	Dako Target Retrieval Solution
TSA	Tyramide signal amplification
TUF	TUF Target Unmasking Fluid
V	Volt
VEN	Venetoclax
WHO	World Health Organisation
ZF	Zinc finger(s)
ZF2	Zinc finger 2

1. Introduction

1.1 Myelodysplastic Syndromes: Contrasting Characteristics in the Adult and Pediatric Disease Landscape

Myelodysplastic syndromes (MDS) represent a diverse spectrum of clonal hematopoietic stem cell disorders characterized by ineffective dysplastic hematopoiesis leading to peripheral cytopenia. The clinical presentation of MDS is highly heterogeneous, encompassing a wide range of severity in cytopenia, blast cell count, and overall prognosis. Irrespective of these variations, patients affected with MDS share a common need for rigorous clinical surveillance, as the potential for malignant progression into secondary acute myeloid leukemia (AML) is a persistent concern.

Contrasting to the adult population, MDS is a relatively rare disease entity in children, constituting approximately 4% of all pediatric hematologic malignancies (Hasle et al., 1999; Hasle et al., 1995). The estimated incidence of pediatric MDS hovers between 1.8 and 4 cases per million children (Hofmann, 2015). Importantly, the pediatric manifestation of MDS exhibits distinctive characteristics with respect to its morphological, cytogenetic, and mutational profiles when juxtaposed against the disease in adults (Bejar et al., 2011; Malcovati et al., 2014). For instance, somatic mutations within the spliceosomal machinery, which are frequently encountered in adult MDS patients (e.g. a gene commonly affected is *SF3B1*), are rarely observed in the pediatric MDS context and do not constitute a pivotal etiological factor (Hirabayashi et al., 2012).

Refractory cytopenia of childhood (RCC) emerges as the most prevalent subtype of pediatric MDS, accounting for approximately 50% of all cases (Niemeyer & Baumann, 2008; Passmore et al., 2003). Children frequently present with neutropenia and/or thrombocytopenia at the time of diagnosis, while in adult MDS, anemia is often the predominant clinical feature (Kardos et al., 2003). At the cytogenetic level, typical aberrations found in adults, such as complex karyotypes or isolated deletion del5(5q), are infrequent in the pediatric cohort (Göhring et al., 2010; Hasle

et al., 1999; Passmore et al., 2003). Conversely, monosomy 7 surfaces as the most common chromosomal alteration in pediatric patients (Kardos et al., 2003). Histomorphological, pediatric MDS also diverges greatly from its adult counterpart, characterized predominantly by hypocellular bone marrow, unilinear or multilinear dysplasia, micromegakaryocytes and frequently patchy distribution of the erythropoiesis (Baumann et al., 2012; Hofmann, 2015).

In response to the pronounced disparities between pediatric and adult MDS, there has been a concerted effort within the scientific community to establish a distinct classification framework tailored to the pediatric population. Following the first formal classification introduced in 1976 by the French-American-British-Cooperative Group, which laid the foundation for the World Health Organisation (WHO) classification introduced in 2000, it wasn't until 2003 when Hasle and colleagues pioneered pediatric-specific guidelines, culminating in the establishment of the first diagnostic criteria for pediatric MDS (Hasle et al., 2003). Subsequently, building upon this pediatric-centred approach, the 2008 WHO classification officially recognized a separate pediatric MDS classification for the first time.

Recent years have witnessed significant advances in the field, with the International Consensus Classification (ICC) delineating further refinements in the classification of pediatric MDS in 2023, expanding the definitions of RCC and myelodysplastic syndrome with excess blasts (MDS-EB) in the pediatric population (Rudelius et al., 2023).

In accordance to the ICC guidelines (Rudelius et al., 2023), RCC is defined by the presence of persistent cytopenia and dysplastic changes in at least two hematopoietic lineages or in ≥ 10% of cells within a single lineage (Table 2). The threshold for blast cells is set at < 5% in the bone marrow and < 2 % in peripheral blood, and approximately 80% of RCC cases are associated with a hypocellular bone marrow.

MDS-EB, on the other hand, is characterized by the presence of 5 – 19% blasts in the bone marrow or 2 – 19% in peripheral blood (Table 2). However, rather than relying solely on predefined blast percentage thresholds, it is recommended that clinical attention be directed toward genetic lesions and the overall clinical course when defining MDS and AML in pediatric patient populations (Rudelius et al., 2023).

Table 2: Diagnostic criteria for the classification of pediatric MDS, excerpt and modified from the ICC guidelines (Rudelius et al., 2023).

	Cytopenia	Dysplastic lineages	Blast count
RCC	≥ 1	≥ 1 (at least two lineages or in ≥ 10% of cells in one lineage)	< 5% bone marrow < 2% peripheral blood
MDS-EB	0 – 3	0 – 3	5 – 19% bone marrow 2 – 19% peripheral blood

RCC: refractory cytopenia of childhood, MDS-EB: myelodysplastic syndrome with excess blasts

1.2 The Role of Genetic Predisposition Syndromes for Pediatric MDS

In recent years, a growing body of evidence has illuminated the role of underlying genetic predisposition syndromes in the development of MDS among children. This emerging understanding has delineated three prominent categories of these predisposing syndromes, comprising MDS arising from inherited bone marrow failure conditions like Fanconi anemia or dyskeratosis congenita (Alter et al., 2010), the sterile alpha motif domain containing 9 (SAMD9) and sterile alpha motif domain containing 9 like (SAMD9L) syndromes (Asou et al., 2009; Pastor et al., 2018), and GATA binding protein 2 (GATA2) deficiency (Hahn et al., 2011; Pasquet et al., 2013; Wlodarski et al., 2016).

Within the framework of inherited bone marrow failure syndromes, it is noteworthy that MDS or MDS-associated AML typically manifests as a secondary complication (Peffault de Latour & Soulier, 2016; Shimamura & Alter, 2010). Conversely, children harboring germline mutations in *SAMD9*, *SAMD9L*, and *GATA2* often present with RCC *a priori* (Sahoo et al., 2020).

With regard to primary MDS of childhood, a significant proportion of cases can be attributed to the presence of germline *SAMD9* and *SAMD9L* mutations. These mutations have been observed to manifest with varying prevalence, reported at 8% within a large multi-institutional cohort (Sahoo et al., 2018) and as high as 17% in a single institution report (Schwartz et al., 2017).

In addition to the SAMD9 and SAMD9L syndromes, GATA2 deficiency emerges as the most prevalent predisposing condition in children affected with primary MDS. A

comprehensive study, encompassing more than 500 patient samples, has underscored the prominence of germline mutations in the *GATA2* gene as the foremost genetic anomaly predisposing children to MDS, accounting for 15% of advanced and 7% of all primary pediatric MDS cases (Wlodarski et al., 2016). This finding highlights the central role of *GATA2* mutations in the etiology of pediatric MDS, emphasizing the need for further investigations into their molecular mechanisms and clinical implications.

1.3 The Significance of the Multifaceted Transcription Factor GATA2 in Hematopoiesis and Disease

GATA2 serves as a principal transcription factor crucial for early hematopoiesis, playing a pivotal role in driving the generation and maintenance of hematopoietic stem cells (HSCs). In contrast to other hematopoietic transcription factors like RUNX family transcription factor 1 (RUNX1), which primarily functions in HSC generation, GATA2 also assumes a critical role in HSC survival (M. J. Chen et al., 2009; de Pater et al., 2013). This underscores the unique and ongoing necessity of GATA2 function in HSCs across all developmental stages (de Pater et al., 2013; Ling et al., 2004).

With its two zinc fingers (ZF), GATA2 shows the capacity to engage GATA DNA motifs within a multitude of genes (Doré et al., 2012; Linnemann et al., 2011). Its substantial contribution for the control of HSCs involves collaboration with a complex network of hematopoietic transcription factors, where GATA2 effectively modulates the activity of other regulatory proteins in a dose-dependent manner (Bresnick et al., 2012; Ling et al., 2004; Rodrigues et al., 2005; Wilson et al., 2010).

The landscape of *GATA2* germline mutations encompasses missense mutations within the second ZF (ZF2) or noncoding variants within a regulatory region of the *GATA2* gene, both resulting in haploinsufficiency (Hahn et al., 2011; Ostergaard et al., 2011). Additionally, truncating mutations, which presumably lead to the loss of ZF2, have been reported (Dickinson et al., 2011). As of 2020, over 300 variants in the *GATA2* gene have been identified (Bresnick et al., 2020). Despite this substantial number, the specific association of these mutations with clinical or histomorphological phenotypes remains enigmatic.

Consequently, individuals with germline mutations in *GATA2* present with a wide spectrum of clinical manifestations, comprising immunodeficiency, MDS/AML, pulmonary disease, and vascular or lymphatic dysfunction (Kazenwadel et al., 2012; Spinner et al., 2014). The phenotypes of GATA2 deficiency encompass complex diseases with overlapping characteristics, including Emberger syndrome with lymphedema (Mansour et al., 2010; Ostergaard et al., 2011), familial or pediatric MDS/AML (Donadieu et al., 2018; Hahn et al., 2011; Sahoo et al., 2020; Wlodarski et al., 2016), monocytopenia and mycobacterial infections syndrome (Hsu et al., 2011; Pasquet et al., 2013; Vinh et al., 2010), and immune deficiency characterized by monocytopenia, reduced dendritic cells, natural killer cells, and B lymphocytes (Bigley et al., 2011; Dickinson et al., 2011; Mace et al., 2013).

What unites individuals with GATA2 deficiency is their propensity to manifest hematologic complications early in life, coupled with a substantially elevated risk of developing MDS, which can progress to secondary AML through a precarious malignant transformation (Hahn et al., 2011; Hirabayashi et al., 2017; Pasquet et al., 2013). In addition to predisposing to hematologic malignancies, GATA2 deficiency leads to a disruption in the regulation of the hematopoietic niche and the composition of the immune microenvironment (Calvo et al., 2011; Nováková et al., 2016). However, the precise mechanisms governing malignant transformation and the contribution of hematopoietic niche perturbation to the development of MDS/AML, remain largely elusive.

1.4 Aim of the Study

Given the limited understanding of the mechanisms underlying malignant transformation, navigating informed therapeutic decisions in the management of pediatric GATA2 deficiency presents a significant challenge. The difficulty to distinguish patients with a high risk of rapid progression from those with a more stable disease course underscores a critical knowledge gap, emphasizing the complexity of this condition. Consequently, further research is imperative to elucidate the factors influencing disease trajectory and guide the development of targeted therapeutic interventions.

This doctoral thesis is dedicated to the systematic exploration of potential mechanisms underlying malignant transformation, particularly within the context of pediatric MDS associated with GATA2 deficiency. The study aims to investigate the complex relationships between genetic abnormalities, potentially pivotal signaling pathways, and the trajectory of the disease. The central research focus driving this inquiry is to enhance our understanding of mechanisms or drivers of malignant transformation and to identify predictive markers for assessing individual risk of disease progression. Once identified, these markers hold the potential to guide therapeutic decisions and facilitate personalized patient management.

Conducting a comprehensive morphological and phenotypic characterization of hematopoiesis, the research aims to contribute to a more holistic understanding of the disease. Employing a multifaceted approach, a phenomics analysis will be conducted to unravel the nuances of hematopoiesis in primary patient samples, correlating the results with cytogenetic data. Additionally, exploring the hematopoietic niche to investigate its impact on disease progression is integral.

To facilitate a systematic characterization of bone marrow biopsies from 57 children diagnosed with RCC or MDS-EB, with or without additional GATA2 germline mutation, a range of complementary methods will be employed. These include multiplex immunofluorescence for simultaneous analysis of up to six different immunofluorescence markers on one tissue section with spatial resolution, traditional immunohistochemistry, gene expression profiling for differential gene expression of 770 genes, RNA-*in situ* hybridization for detection of mRNA with spatial resolution, and computational pathology software for artificial intelligence-assisted quantitative and qualitative image analysis.

In conclusion, this investigation aims to enhance our understanding of pediatric GATA2 deficiency, offering valuable insights that may help to refine diagnostic and therapeutic strategies for affected patients, thus contributing to enhanced patient care.

2. Material and Methods

2.1 Material

2.1.1 Reagents and Ancillaries

Table 3: List of reagents and ancillaries.

Reagent or ancillary	Manufacturer
Acetic Acid ROTIPURAN® 100%, p.a.	Carl Roth GmbH + Co. KG
Albumin, from bovine serum (BSA)	Sigma-Aldrich
6-aminocaproic acid	Sigma-Aldrich
Ammonium peroxydisulphate (APS)	Carl Roth GmbH + Co. KG
1x Antibody Diluent/Block	Akoya Biosciences
10x AR6 Buffer	Akoya Biosciences
10x AR9 Buffer	Akoya Biosciences
Bovine serum albumin (BSA), 2 mg/mL	Bio-Rad Laboratories Inc.
Bromophenol blue	Thermo Fisher Scientific
CC1 Antigen Retrieval Buffer, ready to use	Ventana Medical Systems
CCL18, recombinant human protein	Abcam
10x Cell Lysis Buffer	Cell Signaling Technology
Dako REAL™ Antibody Diluent	Agilent Dako
Dako Target Retrieval Solution, pH6, 10x (TRS6)	Agilent Dako
4,6-Diamidino-2-phenylindole (DAPI), dilactate	Biotium
Dithiothreitol (DTT)	Thermo Fisher Scientific
Ethanol, absolute	Chemsolute® a Brand of Th. Geyer
Dimethyl sulfoxide (DMSO), for cell culture, 99.5%	PanReac AppliChem

Fetal bovine serum	Biowest
Gibco™ Dulbecco's Phosphate Buffered Saline, 1x (PBS)	Thermo Fisher Scientific
Gibco™ Iscove's Modified Dulbecco's Medium	Thermo Fisher Scientific
Gibco™ Penicillin Streptomycin	Thermo Fisher Scientific
Gibco™ RPMI Medium 1640	Thermo Fisher Scientific
Glycine PUFFERAN® > 99%, p.a.	Carl Roth GmbH + Co. KG
Glycerol ROTIPURAN® > 99.5%, p.a.	Carl Roth GmbH + Co. KG
HISTOPRIME® Hematoxylin (Mayer)	Linaris Biologische Produkte GmbH
HISTOPRIME® HistoPerm	Linaris Biologische Produkte GmbH
Hydrogen Peroxide, 35%	Carl Roth GmbH + Co. KG
Immobilon®-P polyvinylidene difluoride (PVDF) membrane, 0.45 µm pore size	Merck KGaA
Isopropanol	Carl Roth GmbH + Co. KG
Methanol, p.a.	Chemsolute® a Brand of Th. Geyer
Neutral buffered formalin	Sigma-Aldrich
Non-fat skimmed milk powder	Biomol GmbH
1x Opal™ Anti-Ms + Rb horseradish peroxidase (HRP)	Akoya Biosciences
Phenylmethylsulfonyl fluoride (PMSF)	Carl Roth GmbH + Co. KG
Phorbol 12-myristate 13-acetate (PMA)	Sigma-Aldrich
1x Plus Manual Amplification Diluent	Akoya Biosciences
Precision Plus Protein Dual Color Standards, 500 µL	Bio-Rad Laboratories Inc.
ProTaqs Antigen Enhancer I, pH 6.0, 50x (ProTaqs I)	BIOCYC GmbH & Co. KG
100x Protease Inhibitor Cocktail	Cell Signaling Technology
Protein Assay Dye Reagent Concentrate (Bradford reagent)	Bio-Rad Laboratories Inc.
RNAscope® Probe Hs-CD34-C3	ACD a Bio-Techne Brand

RNAscope® Probe Hs-EZH2	ACD a Bio-Techne Brand
RNAscope® Probe Hs-GATA2	ACD a Bio-Techne Brand
RNAscope® Probe Hs-IKZF1	ACD a Bio-Techne Brand
RNAscope® Probe Hs-LYL1	ACD a Bio-Techne Brand
RNAscope® Probe Hs-RUNX1	ACD a Bio-Techne Brand
Rotiphorese® gel 30 (37.5:1)	Carl Roth GmbH + Co. KG
Sodium chloride, > 99.8%	Carl Roth GmbH + Co. KG
Sodium dodecyl sulfate (SDS) ultra-pure, > 99%	Carl Roth GmbH + Co. KG
N,N,N‘,N‘-tetramethylethylenediamine (TEMED), > 99% p.a.	Carl Roth GmbH + Co. KG
Tris PUFFERAN® > 99.9%, p.a.	Carl Roth GmbH + Co. KG
Triton X-100	Carl Roth GmbH + Co. KG
Trypan Blue Dye 0.40%	Bio-Rad Laboratories Inc.
TUF Target Unmasking Fluid (TUF) (3x concentrated)	PANPATH B.V.
Tween® 20	Carl Roth GmbH + Co. KG
VECTASHIELD® Antifade Mounting Medium	Biozol Diagnostica Vetrieb GmbH
WesternSure® Pen	LI-COR Biosciences
Whatman™ 3 MM Chr	GE HealthCare Technologies
Xylene	Chemsolute® a Brand of Th. Geyer

2.1.2 Kits

The table below presents an overview of commercially available kits utilized in this study, organized according to the method of consumption.

Table 4: List of kits.

Kit	Manufacturer
Multiplex immunofluorescence	
Opal™ 520 Reagent Pack	Akoya Biosciences
Opal™ 540 Reagent Pack	Akoya Biosciences

Opal™ 570 Reagent Pack	Akoya Biosciences
Opal™ 620 Reagent Pack	Akoya Biosciences
Opal™ 650 Reagent Pack	Akoya Biosciences
Opal™ 690 Reagent Pack	Akoya Biosciences
Opal™ 780 Reagent Pack	Akoya Biosciences
Immunohistochemistry	
ImmPRESS® HRP Horse Anti-Mouse IgG Polymer Detection Kit, Peroxidase	Vector Laboratories
ImmPRESS® HRP Horse Anti-Rabbit IgG Polymer Detection Kit, Peroxidase	Vector Laboratories
HISTOPRIME® Peroxidase-Substrate-Kit DAB	Linaris Biologische Produkte GmbH
Gene expression profiling – RNA isolation and purification	
RNeasy® DSP FFPE Kit	Qiagen
Gene expression profiling – NanoString's nCounter® assay for gene expression analysis	
nCounter® Human PanCancer Immune Profiling Panel	NanoString Technologies
nCounter® Standard Cartridges	NanoString Technologies
nCounter® Standard Prep Pack	NanoString Technologies
nCounter® Standard Prep Plates	NanoString Technologies
RNA-*in situ* hybridization	
RNAscope® H_2O_2 & Protease Plus Reagents	ACD a Bio-Techne Brand
RNAscope® Multiplex Fluorescent Detection Kit v2	ACD a Bio-Techne Brand
RNAscope® Target Retrieval Reagents	ACD a Bio-Techne Brand
RNAscope® Wash Buffer Reagents	ACD a Bio-Techne Brand
Western blot analysis - Immunodetection	
SuperSignal™ West Pico PLUS Chemiluminescent Substrate	Thermo Fisher Scientific

2.1.3 Buffers and Solutions

The various buffers and solutions used in this work are listed below. Unless otherwise stated, all buffers and solutions were stored at 4°C protected from light.

Table 5: List of buffers and solutions.

Buffer or solution	Composition
Multiplex immunofluorescence	
1x AR6 buffer	25 mL 10x AR6 buffer *(Akoya Biosciences)* 225 mL ddH_2O
1x AR9 buffer	25 mL 10x AR9 buffer *(Akoya Biosciences)* 225 mL ddH_2O
DAPI solution (1 mg/mL)	21.9 µM DAPI, dilactate *(Biotium)* PBS *(Thermo Fisher Scientific)* ad 1000 mL (10 mg/L DAPI solution); 1 mL 10 mg/L DAPI solution 999 mL PBS *(Thermo Fisher Scientific)* aliquoted in 100 µL
DAPI working solution	2 µL DAPI solution (1 mg/mL) 998 µL 1x TBST buffer, pH 7.5
Opal™ 520 (540/570/620/650/690) solution	Opal™ Polaris 520 (540/570/620/650/690) reagent reconstituted in 75 µL DMSO *(included in the Opal™ Reagent Packs, Akoya Biosciences)*
Opal™ 520 (540/570/620/650/690) working solution	1 µL Opal™ 520 (540/570/620/650/690) solution 99 µL 1x Plus Manual Amplification Diluent *(Akoya Biosciences)*
Opal™ 780 solution	Opal™ Polaris 780 reagent reconstituted in 300 µL ddH_2O *(included in the Opal™ 780 Reagent Pack, Akoya Biosciences)*
Opal™ 780 working solution	1 µL Opal™ 780 solution 24 µL 1x Antibody Diluent/Block solution *(Akoya Biosciences)*

Opal™ TSA-DIG solution	Opal™ TSA-DIG reagent reconstituted in 75 µL DMSO *(included in the Opal™ 780 Reagent Pack, Akoya Biosciences)*
Opal™ TSA-DIG working solution	1 µL Opal™ TSA-DIG solution 99 µL 1x Plus Manual Amplification Diluent *(Akoya Biosciences)*
1x ProTaqs I buffer	20 mL 50x ProTaqs I buffer *(BIOCYC GmbH & Co. KG)* 980 mL ddH_2O
10x TBS buffer, pH 7.5	250 mM Tris PUFFERAN® *(Carl Roth GmbH + Co. KG)* 1.5 M sodium chloride *(Carl Roth GmbH + Co. KG)* pH 7.5 adjusted with acetic acid ROTI-PURAN® *(Carl Roth GmbH + Co. KG)* ddH_2O ad 1000 mL
1x TBST buffer, pH 7.5	100 mL 10x TBS, pH 7.5 0.5 mL Tween® 20 *(Carl Roth GmbH + Co. KG)* 900 mL ddH_20
1x TRS6 buffer	10 mL 10x TRS6 buffer *(Agilent Dako)* 90 mL ddH_2O
1x TUF buffer	30 mL 3x TUF buffer *(PANPATH B.V.)* 60 mL ddH_2O
Immunohistochemistry	
1x AR6 buffer	See multiplex immunofluorescence
1x AR9 buffer	See multiplex immunofluorescence
DAB working solution	4 drops DAB chromogen solution 5 mL DAB substrate buffer *(included in the HISTOPRIME® Peroxidase-Substrate-Kit DAB, Linaris Biologische Produkte GmbH)*

Hydrogen peroxide, 3.5%	10 mL hydrogen peroxide, 35% *(Carl Roth GmbH + Co. KG)* 90 mL ddH_2O stored at RT protected from light
10x TBS buffer, pH 7.6	200 mM Tris PUFFERAN® *(Carl Roth GmbH + Co. KG)* 1.37 M sodium chloride *(Carl Roth GmbH + Co. KG)* pH 7.6 adjusted with acetic acid ROTI-PURAN® *(Carl Roth GmbH + Co. KG)* ddH_2O ad 1000 mL
1x TBS buffer, pH 7.6	100 mL 10x TBS, pH 7.6 900 mL ddH_2O
1x TRS6 buffer	See multiplex immunofluorescence
1x TUF buffer	See multiplex immunofluorescence
RNA-*in situ* hybridization	
1x antigen retrieval buffer	10 mL 10x antigen retrieval buffer 90 mL ddH_2O *(antigen retrieval buffer included in the RNAscope® Target Retrieval Reagents, ACD a Bio-Techne Brand)*
Co-detection probe solution	1 µL RNAscope® Probe Hs-CD34-C3 39 µL RNAscope® Probe Hs-EZH2 (or Hs-RUNX1)
Opal™ 570 single probe working solution	1 µL Opal™ 570 solution 749 µL 1x Plus Manual Amplification Diluent *(Akoya Biosciences)*
Opal™ 570 (or 690) co-detection working solution	1 µL Opal™ 570 (or 690) solution 499 µL 1x Plus Manual Amplification Diluent *(Akoya Biosciences)*
1x wash buffer	20 mL 50x wash buffer 980 mL ddH_2O *(wash buffer included in the RNAscope® Wash Buffer Reagents, ACD a Bio-Techne Brand)* stored at RT

Cell culture - Subculturing			
K-562 medium	500 mL RPMI Medium 1640 *(Thermo Fisher Scientific)* 50 mL fetal bovine serum *(Biowest)* 5 mL Penicillin Streptomycin *(Thermo Fisher Scientific)*		
KG-1 medium	500 mL Iscove's Modified Dulbecco's Medium *(Thermo Fisher Scientific)* 100 mL fetal bovine serum *(Biowest)*		
Cell culture – PMA stimulation			
PMA stock solution	100 µM PMA (*Sigma-Aldrich*) 16.2 mL DMSO (*PanReac AppliChem*) aliquoted in 1 mL and stored at -20°C		
PMA working solutions	10 µM PMA:	500 µL PMA stock	4500 µL cells
	1 µM PMA:	50 µL PMA stock	4950 µL cells
	100 nM PMA:	500 µL PMA 1 µM	4500 µL cells
	10 nM PMA:	50 µL PMA 1 µM	4950 µL cells
	1 nM PMA:	5 µL PMA 1 µM	4995 µL cells
Cell culture - Protein isolation			
PMSF solution	100 mM PMSF *(Carl Roth GmbH + Co. KG)* Isopropanol *(Carl Roth GmbH + Co. KG)* ad 20 mL stored at -20°C protected from light		
1x cell lysis buffer	9 mL ddH_2O 1 mL 10x Cell Lysis Buffer *(Cell Signaling Technology)* 100 µL 100x Protease Inhibitor Cocktail *(Cell Signaling Technology)* 100 µL PMSF solution		

Western blot analysis - Bradford assay			
Triton X-100 solution (0.01%)	0.5 mL Triton X-100 *(Carl Roth GmbH + Co. KG)* 45.5 mL 1x PBS *(Thermo Fisher Scientific)* stored at RT protected from light		
BSA solution (0.2 mg/mL)	100 µL BSA, 2 mg/mL *(Bio-Rad Technologies Inc.)* 900 µL Triton X-100 solution		
BSA standards	0 µg BSA:	0 µL BSA solution	400 µL Triton X-100 solution
	2 µg BSA:	10 µL BSA solution	390 µL Triton X-100 solution
	4 µg BSA:	20 µL BSA solution	380 µL Triton X-100 solution
	6 µg BSA:	30 µL BSA solution	370 µL Triton X-100 solution
	8 µg BSA:	40 µL BSA solution	360 µL Triton X-100 solution
Protein sample dilution	5 µL isolated protein 45 µL 1x PBS *(Thermo Fisher Scientific)*		
Protein sample	20 µL protein sample dilution 180 µL 1x PBS *(Thermo Fisher Scientific)* 200 µL Triton X-100 solution		
Western blot analysis - SDS gel electrophoresis			
10% APS	438 mM APS *(Carl Roth GmbH + Co. KG)* ddH_2O ad 5 mL		
20% SDS	693.9 mM SDS ultra-pure *(Carl Roth GmbH + Co. KG)* ddH_2O ad 250 mL		
Tris pH 6.8	1 M Tris PUFFERAN® *(Carl Roth GmbH + Co. KG)* pH 6.8 adjusted with acetic acid ROTI-PURAN® *(Carl Roth GmbH + Co. KG)* ddH_2O ad 250 mL		

Tris pH 8.8		1 M Tris PUFFERAN® *(Carl Roth GmbH + Co. KG)* pH 8.8 adjusted with acetic acid ROTI-PURAN® *(Carl Roth GmbH + Co. KG)* ddH_2O ad 250 mL
5x SDS sample buffer		3.125 mL Tris pH 6.8 250 mM DTT *(Thermo Fisher Scientific)* 347 mM SDS (*Carl Roth GmbH + Co. KG)* 0.5 mL bromophenol blue *(Thermo Fisher Scientific)* 5 mL Glycerole ROTIPURAN® *(Carl Roth GmbH + Co. KG)* ddH_2O ad 10 mL aliquoted in 500 µL and stored at -20°C
Running gel (for 4 gels)	10%	8.3 mL ddH_2O 6.65 mL Rotiphorese® gel 30 *(Carl Roth GmbH + Co. KG)* 5 mL Tris pH 8.8 125 µL 20% SDS 125 µL 10% APS 50 µL TEMED *(Carl Roth GmbH + Co. KG)*
	12.5%	5 mL ddH_2O 10.5 mL Rotiphorese® gel 30 *(Carl Roth GmbH + Co. KG)* 9.35 mL Tris pH 8.8 125 µL 20% SDS 125 µL 10% APS 50 µL TEMED *(Carl Roth GmbH + Co. KG)*
	20%	8.86 mL ddH_2O 13.2 mL Rotiphorese® gel 30 *(Carl Roth GmbH + Co. KG)* 7.5 mL Tris pH 8.8 150 µL 20% SDS 150 µL 10% APS 15 µL TEMED *(Carl Roth GmbH + Co. KG)*

Stacking gel (for 4 gels)	7 mL ddH_2O 1.672 mL Rotiphorese® gel 30 *(Carl Roth GmbH + Co. KG)* 1.252 mL Tris pH 6.8 50 µL 20% SDS 100 µL 10% APS 25 µL TEMED *(Carl Roth GmbH + Co. KG)*
10x SDS running buffer	250 mM Tris PUFFERAN® *(Carl Roth GmbH + Co. KG)* 1.96 M Glycine PUFFERAN® *(Carl Roth GmbH + Co. KG)* 50 mL 20% SDS ddH_2O ad 1000 mL stored at RT protected from light
1x SDS running buffer	100 mL 10x SDS running buffer 900 mL ddH_2O stored at RT protected from light
Western blot analysis - Semi-dry blotting	
Anode buffer I	300 mM Tris PUFFERAN® *(Carl Roth GmbH + Co. KG)* 100 mL methanol p.a. *(Chemsolute® a Brand of Th. Geyer)* ddH_2O ad 500 mL stored at RT protected from light
Anode buffer II	25 mM Tris PUFFERAN® *(Carl Roth GmbH + Co. KG)* 100 mL methanol p.a. *(Chemsolute® a Brand of Th. Geyer)* ddH_2O ad 500 mL stored at RT protected from light
Cathode buffer	25 mM Tris PUFFERAN® *(Carl Roth GmbH + Co. KG)* 100 mL methanol p.a. *(Chemsolute® a Brand of Th. Geyer)* 40 mM 6-aminocaproic acid *(Sigma-Aldrich)* ddH_2O ad 500 mL stored at RT protected from light

Western blot analysis - Immunodetection	
5% BSA solution	759 µM BSA *(Sigma-Aldrich)* 100 mL 1x TBST buffer aliquoted in 15 mL and stored at -20°C
5% skimmed milk powder solution	12.5 g non-fat skimmed milk powder *(Biomol GmbH)* 250 mL 1x TBST buffer
10x TBS buffer	20 mM Tris PUFFERAN® *(Carl Roth GmbH + Co. KG)* 137 mM sodium chloride *(Carl Roth GmbH + Co. KG)* ddH_2O ad 1000 mL
1x TBST buffer	100 mL 10x TBS buffer 10 mL Tween® 20 *(Carl Roth GmbH + Co. KG)* ddH_2O ad 1000 mL

2.1.4 Human Cell Lines

Table 6: List of human cell lines.

Cell line	Origin	Source
K-562	Lymphoblast cells, bone marrow 53-year old female, chronic myelogenous leukemia	Laboratory of Prof. O. T. Keppler
KG-1	Macrophages, bone marrow 59-year old male, acute myelogenous leukemia	Laboratory of Prof. O. T. Keppler

2.1.5 Antibodies

Table 7: List of antibodies.

Antibody	Clone	Host species	Application (dilution)	Demask-ing/block-ing solution	Manufac-turer
Anti-mouse IgG, HRP-linked	-	horse	Western blot (1:5000)	skimmed milk	Cell Signaling Technology
Anti-rabbit IgG, HRP-linked	-	goat	Western blot (1:5000)	skimmed milk	Cell Signaling Technology

BCL2	124	mouse	mIF (1:25)	CC1	Agilent Dako
Bcl-XL	BX006 +2H12	mouse	mIF (1:75)	AR9	Abcam
Caspase 1 p20 (Cleaved Asp296)	poly-clonal	rabbit	mIF (1:50) IHC (1:200)	ProTaqs I	Thermo Fisher Scientific
CCL18	poly-clonal	rabbit	Western blot (1:1000)	skimmed milk	Abcam
CCL18	poly-clonal	rabbit	mIF (1:75) IHC (1:125)	TRS6	Abnova
CD117	poly-clonal	rabbit	mIF(1:100)	AR6	Agilent Dako
CD123/ IL3RA	IL3RA/ 2947R	rabbit	mIF (1:50)	AR9	Abcam
CD14	EPR 3653	rabbit	mIF (1:100)	AR6	Cell Marque Corpora-tion
CD163	10D6	mouse	mIF (1:150)	AR9	Leica Bio-systems
CD20	L26	mouse	mIF (1:400)	CC1	Dako Agilent
CD3	SP7	rabbit	mIF (1:150)	AR9	Zytomed Systems
CD34	QEBnd -10	mouse	mIF (1:100) IHC (1:50)	AR6 (mIF) CC1 (IHC)	Cell Marque
CD42b	SP219	rabbit	mIF (1:100)	AR9	Abcam
CD71	MRQ-48	mouse	mIF (1:400)	CC1	Cell Marque
CD8	C8/ 144B	mouse	mIF (1:150)	AR9	Cell Marque
Cleaved Caspase-3 (Asp175)	poly-clonal	rabbit	mIF (1:50)	AR9	Cell Signaling Technology

E-Cadherin	EP6	rabbit	IHC (1:50)	TRS6	Bio SB, Inc.
EPX	poly-clonal	rabbit	mIF (1:180) IHC (1:180)	TRS6	Atlas Antibodies
EZH2	D2C9	rabbit	IHC (1:50)	AR9	Cell Signaling Technology
FOXP3	236A/ E7	mouse	mIF (1:50)	AR9	Abcam
Gasdermin D	E7H9G	rabbit	IHC (1:200)	AR9	Cell Signaling Technology
IκBα	L35A5	mouse	Western Blot (1:1000)	BSA	Cell Signaling Technology
Ki-67	MIIB-1	mouse	IHC (1:100)	CC1	Dako Agilent
Mast Cell Tryptase	AA1	mouse	mIF (1:200)	AR6	Diagnostic BioSystems
MCL1	OTI10F 6	mouse	mIF (1:75)	AR6	Thermo Fisher Scientific
Myeloperoxi-dase	poly-clonal	rabbit	mIF (1:100)	None or TRS6	Agilent Dako
NALP3/ NLRP3	poly-clonal	rabbit	mIF (1:200)	TRS6	Lifespan Biosciences
Perilipin-1	D1D8	rabbit	mIF (1:150)	AR6	Cell Signaling Technology
PD-1	NAT10 5	mouse	mIF (1:80)	TRS6	Cell Marque
RUNX1	DW71	mouse	IHC (1:75)	TUF	Santa Cruz Biotechnol-ogy

S100A9	D5O6O	rabbit	mIF (1:300)	AR6	Cell Signaling Technology
SCF	C19H6	rabbit	mIF (1:50)	AR6	Cell Signaling Technology
Terminal Deoxynucleo-tidyl Transfer-ase (TdT)	SEN28	mouse	mIF (1:50)	AR9	Diagnostic Biosystems
TIM-3	D5D5r	rabbit	mIF (1:200)	AR9	Cell Signaling Technology
Tri-Methyl-Histone H3 (Lys27)	C36B11	rabbit	mIF (1:100) IHC (1:4000)	AR9	Cell Signaling Technology

mIF: Multiplex immunofluorescence, IHC: Immunohistochemistry

2.2 Methods

2.2.1 Multiplex Immunofluorescence

Akoya's Opal™ system offers a highly specific solution for multiplex immunofluorescence (mIF) stainings with reagent based signal amplification utilizing tyramide signal amplification (TSA) reagents alias Opal™ dyes. Following the binding of primary and secondary antibodies, the TSA reagent, which contains free tyramide radicals bound to a reporter fluorophore, covalently labels the targeted epitope.

After labeling is complete, the primary and secondary antibodies will be stripped without disrupting the Opal™ fluorescence signal. This allows the user to proceed to the second staining cycle, which will detect the next target with a TSA reagent labeled with a different fluorophore. In this way, a custom multiplexed panel can be created for simultaneous analysis of up to six immunofluorescence markers within one tissue section.

Microscope glass slides with 2-5 µm thick tissue sections of formalin-fixed, paraffin-embedded (FFPE) trephine biopsies of the bone marrow were used for analysis. To

prepare the tissue for the staining procedure, all slides were gently baked overnight at 55°C in the drying cabinet (Binder World Standard Series, *TEquipment*).

Deparaffinization was completed in accordance to the following protocol. The trephine biopsy sections were dewaxed with xylene (2x 15 min), and then rehydrated through a graded series of aqueous ethanol solutions (absolute ethanol 1x 5 min, 96% 1x 5 min and 70% 1x 5 min). Following rehydration, the tissue was briefly rinsed with ddH_2O and fixed in 4% neutral buffered formalin for 20 min at RT.

Beginning the first staining cycle, the slides were washed 3x 2 min in ddH_20 with agitation. To unmask the antigen, the biopsy specimens were transferred to a boiling water bath where they were incubated for 15 min in a Hellendahl staining jar filled with antigen retrieval buffer. The choice of the optimal retrieval buffer is dependent on the characteristics of the tissue and the antibody to be stained, and was subject to prior testing and optimization for each individual target of interest.

The slides were cooled down to RT for 15 min, and washed in 1x TBST buffer, pH 7.5 with agitation (3x 2 min). After excess buffer was removed, the tissue sections were covered with 1x Antibody Diluent/Block solution *(Akoya Biosciences)* for 10 min at RT. All incubation steps were performed in a humidified chamber (Staining Chamber StainTray™ Black lid, *Carl Roth GmbH + Co. KG*) with the biopsy specimens protected from light throughout the workflow.

1x Antibody Diluent/Block solution *(Akoya Biosciences)* was used to prepare the primary antibody solution. Excess blocking solution was drained off, and the slides were incubated in the diluted primary antibody for 1 h at RT. Before the antibodies were combined for use in multiplexed detection, the incubation time and optimal concentration were optimized in a fluorescence monoplex immunohistochemistry staining for each target individually with respect to the chosen antigen retrieval conditions.

The trephine biopsy sections were washed 3x 2 min in 1x TBST buffer, pH 7.5 with agitation. Excess washing buffer was removed, and the slides were incubated in the HRP conjugate solution (1x Opal™ Anti-Ms + Rb HRP, *Akoya Biosciences*) for 10 min at RT.

The washing procedure was repeated (3x 2 min, 1x TBST, pH 7.5). After removing excess buffer, the tissue was covered with Opal™ 520, 540, 570, 620, 650, or 690 working solution for 10 min at RT. All Opal™ working solutions were prepared shortly prior to their use. Due to the light sensitivity of the Opal™ working solutions, the slides were protected from light whenever possible throughout the following workflow.

To complete the first staining cycle, the biopsy sections were washed 3x 2 min in 1x TBST buffer, pH 7.5 with agitation. The slides were placed in a boiling water bath for 15 min to strip away the primary and secondary antibodies, while preserving the covalently bound TSA reagents to ensure that the signal is localized to the target. This time, to retrieve the epitope for the upcoming cycle, the tissue was incubated in the appropriate antigen retrieval buffer for the target to be detected next.

The specimens were cooled down to RT for 15 min, and washed in 1x TBST buffer, pH 7.5 with agitation (3x 2 min). The slides were either stored until the next day at 4°C in a Hellendahl staining jar filled with 1x TBST buffer, pH 7.5 or processed to the next staining cycle, beginning with the 10 min incubation in 1x Antibody Diluent/Block solution *(Akoya Biosciences)*. All subsequent cycles followed the same protocol as the first. The procedure was repeated for up to six targets of interest, each with a different Opal™ fluorophore.

Following the water bath treatment concluding the final cycle, the slides were cooled down to RT for 15 min, and washed 3x 2 min in 1x TBST buffer, pH 7.5 with agitation. In the humidified chamber, the specimens were counterstained for 5 min with DAPI working solution at RT. After the tissue sections were rinsed in ddH_2O, they were covered with mounting medium (VECTASHIELD® Antifade Mounting Medium, *Biozol Diagnostica Vetrieb GmbH*), and sealed with a glass coverslip.

If Opal™ 780 was to be used, it was incorporated in the multiplex staining at the last cycle. Blocking, primary antibody incubation and introduction of secondary HRP were conducted as described above.

Following the incubation in 1x Opal™ Anti-Ms + Rb HRP solution *(Akoya Biosciences)*, the slides were washed in 1x TBST buffer, pH 7.5 with agitation (3x 2 min). Excess

washing buffer was removed, and the tissue was covered with freshly prepared Opal™ TSA-DIG working solution for 10 min at RT.

The washing procedure was repeated (3x 2 min, 1x TBST, pH 7.5), followed by the water bath treatment for 15 min in antigen retrieval buffer. The biopsy specimens were cooled down to RT for 15 min, and washed 3x 2 min in 1x TBST buffer, pH 7.5 with agitation.

Excess buffer was removed. The tissue was incubated in Opal™ 780 working solution for 1 h at RT. Opal™ 780 working solution was prepared shortly before its use.

The trephine biopsy sections were washed in 1x TBST buffer, pH 7.5 with agitation (3x 2 min), and counterstained with DAPI working solution for 5 min at RT. After rinsing in ddH_2O, the tissue was sealed with a coverslip and mounting medium. All stained slides were stored in a slide box at 4°C.

The PhenoImager™ HT Automated Quantitative Pathology Imaging System *(Akoya Biosciences)* was used to obtain an overview scan of the entire tissue. Regions of interest on the stained sections were annotated with the Phenochart™ Whole Slide Viewer *(Akoya Biosciences)*, and a second scan was performed to generate multispectral images (MSI) of the annotated regions of interest.

Unmixing of the MSI and correction for tissue autofluorescence was conducted using the inForm® Automated Image Analysis Software Package *(Akoya Biosciences)*. The images were exported for downstream analysis in the computational pathology software HALO® 3.3, including HALO AI™ 3.3 *(Indica Labs)*.

Akoya's liquid crystal tunable filter (LCTF) technology was utilized for multiplexed panels consisting of DAPI and the Opals 520, 570, 620, 690, and/or 780 (not compatible with Opals 540 and 650). Whole slide multispectral images were generated with the LCTF that already included quantitative unmixing and tissue autofluorescence detection, eliminating the need to re-scan in order to create a MSI.

The multispectral image of the whole tissue was disassembled into multiple tiles for batch export with the inForm® Automated Image Analysis Software Package *(Akoya Biosciences)*, and recomposed for further analysis and quantitative evaluation in HALO® 3.3, including HALO AI™ 3.3 *(Indica Labs)*.

For mIF stainings, the HALO® module HighPlex FL v4.1.2 *(Indica Labs)* was used. A custom algorithm was configured and trained in accordance with the recommendations provided in the user guide.

In brief, the tissue was visually inspected for quality control, and distinct analysis regions were annotated if necessary. A HALO® AI Nuclear Phenotyper for fluorescence images was created and optimized for nuclei detection and nuclear segmentation on the specimen to analyse. The number of dyes was specified and dye positivity thresholds were adjusted for each fluorophore individually in relation to its cellular compartment (nuclear, cytoplasm or membrane dyes). Different phenotypes were created as needed for analysis.

The results were exported in tabular form and the data was processed for graphical presentation and statistical analysis in GraphPad Prism, version 9.5.0 *(GraphPad Software Inc.)*.

2.2.2 Immunohistochemistry

For immunohistochemistry (IHC) staining, microscope glass slides with 2-5 µm thick tissue sections of FFPE trephine biopsies of the bone marrow were used. After overnight incubation at 55°C in the drying cabinet (Binder World Standard Series, *TEquipment*), the slides were deparaffinized and rehydrated as described for mIF (please refer to section 2.2.1).

Following rehydration, the biopsy specimens were washed for 5 min in ddH_2O. To unmask the antigen, the tissue sections were placed in a Hellendahl staining jar filled with antigen retrieval buffer and microwaved 2x 15 min at 80% power. Prior testing and optimization determined which antigen retrieval buffer led to the best results for each target of interest.

The slides were cooled down to RT for 15 min. To quench endogenous peroxidase activity in the tissue sections, they were incubated in the dark for 20 min at RT in hydrogen peroxide, 3.5% solution.

The specimens were washed 2x 2 min in 1x TBS buffer, pH 7.6 with agitation. Excess buffer was removed, and the tissue was incubated for 20 min in normal goat serum

(included in ImmPRESS® HRP Horse Anti-Mouse or Anti-Rabbit IgG Polymer Detection Kit, Peroxidase, *Vector Laboratories*). Throughout the complete staining procedure, all incubation steps were performed at RT in the humidified chamber in the dark (Staining Chamber StainTray™ Black lid, *Carl Roth GmbH + Co. KG*).

The dilution for the primary antibody was prepared using Dako REAL™ Antibody Diluent *(Agilent Dako)*. Following removal of excess blocking solution, the tissue was incubated in the diluted primary antibody for 1 h at RT. Complementary to the choice of the retrieval buffer, the best concentration and incubation time were additionally optimized for each antibody individually.

After washing the slides in 1x TBS buffer, pH 7.6 with agitation (2x 2 min), they were covered for 30 min at RT with ImmPRESS® (Peroxidase) Polymer Anti-Mouse or Anti-Rabbit IgG Reagent (included in ImmPRESS® HRP Horse Anti-Mouse or Anti-Rabbit IgG Polymer Detection Kit, Peroxidase, *Vector Laboratories*). The ImmPRESS® staining system enables a one-step detection as the polymerized reporter enzyme is already attached to the secondary antibody.

The washing procedure was repeated (2x 2 min, 1x TBS, pH 7.6), and the trephine biopsy sections were incubated for 10 min in DAB working solution. The slides were washed in tap water for 2 min to disrupt the DAB colour development. In the humidified chamber, the specimens were counterstained for 2 min at RT with HISTOPRIME® Hematoxylin *(Linaris Biologische Produkte GmbH)*.

The tissue sections were rinsed for 2 min under running tap water, and then dehydrated through a graded series of aqueous ethanol solutions (70% 1x 1 min, 96% 1x 1 min and 1x 1 min absolute ethanol). After rinsing in xylene, the tissue was sealed with a coverslip and mounting medium (HISTOPRIME® HistoPerm, Linaris Biologische Produkte GmbH). The stained slides were stored in a slide box at 4°C.

The PhenoImager™ HT Automated Quantitative Pathology Imaging System *(Akoya Biosciences)* was used to obtain overview scans of the entire tissue as well as exclusive scans of regions of interest that had been selected and annotated using the Phenochart™ Whole Slide Viewer *(Akoya Biosciences)*. Using the inForm® Auto-

mated Image Analysis Software Package *(Akoya Biosciences)*, the images were prepared for further analysis and quantitative evaluation with HALO® 3.3 and HALO AI™ 3.3 *(Indica Labs)*.

A Random Forest tissue classifier was trained on the IHC images to optimize the cellular detection on the tissue, while excluding any background (e.g. glass from the slide). The HALO® module Multiplex IHC v3.1.3 *(Indica Labs)* was used to create a custom algorithm for analysis. Following visual quality control of the MSI, the colour for deconvolution was set for each dye individually. Nuclei detection and nuclear segmentation were adjusted with a HALO® AI Nuclear Phenotyper for brightfield images. Cell membrane and cytoplasm compartments were segmented, and positivity thresholds were set for each stain of interest.

Data from analysed images was transferred to GraphPad Prism, version 9.5.0 *(GraphPad Software Inc.)* for graphical presentation and statistical analysis.

Alternatively, employing a semiquantitative analysis approach (Remmele & Stegner, 1987), the slides were visually inspected to assess both staining intensity and the proportion of positively stained cells. Immunoreactive scores were then obtained by multiplying these two parameters and graded according to the predefined criteria outlined in the following table (Table 8).

Table 8: Grading criteria to obtain immunoreactive scores.

Staining intensity		Positive cells		Immunoreactive score	
0	No staining	**0**	No positive cells	**0 – 2**	Negative
1	Weak staining	**1**	Less than 10%	**3 – 4**	Weakly positive
2	Moderate staining	**2**	10 – 50%	**6 – 8**	Moderately positive
3	Strong staining	**3**	51 – 80%	**9 - 12**	Strongly positive
		4	More than 80%		

2.2.3 Gene Expression Profiling

To prepare the tissue specimens for use in downstream biological assays, nucleic acids were extracted from FFPE trephine biopsies of the bone marrow.

2.2.3.1 RNA Isolation and Purification

Following the instructions outlined in the RNeasy® DSP FFPE Kit manual *(Qiagen)*, total RNA was purified from freshly cut 5-10 µm thick FFPE tissue sections. Depending on the tissue size, up to four sections were combined in one preparation.

In brief, the principle of the procedure can be described as follows.

Deparaffinization Solution (included in the RNeasy® DSP FFPE Kit, *Qiagen*) was used to deparaffinize the specimens. The samples were then incubated in a lysis buffer containing proteinase K (included in the RNeasy® DSP FFPE Kit, *Qiagen*) to release nucleic acids from the trephine biopsy sections. A short heat treatment partially reversed the formalin crosslinking of free RNA, increasing the quality and yield of the extraction.

DNase I treatment (included in the RNeasy® DSP FFPE Kit, *Qiagen*) was used to remove genomic DNA. To facilitate RNA binding to the membrane of the RNeasy MinElute spin columns (included in the RNeasy® DSP FFPE Kit, *Qiagen*), a buffer solution containing ethanol was added to the lysed samples. Via spin column-based purification, remaining contaminants and binding salts were washed away. After a final drying step to evaporate the alcohol, purified nucleic acids were eluted in RNase-free water (included in the RNeasy® DSP FFPE Kit, *Qiagen*).

RNA quality and quantity were assessed with spectrophotometric readings (Thermo Scientific™ NanoDrop™ One Spectrophotometer, *Thermo Fisher Scientific*). The extracted nucleic acids were stored at -80°C.

2.2.3.2 NanoString's nCounter® Assay for Gene Expression Analysis

NanoString's nCounter® platform offers a molecular barcode system based on CodeSet chemistry including a Reporter CodeSet and a Capture ProbeSet. Excess probes are removed as the reporter and capture probes hybridize to the target of interest, forming a target-probe complex that is then immobilized and aligned to a cartridge. A maximum of 770 genes can be detected simultaneously for up to 12 samples in one experiment using one of NanoString's ready-to-use gene expression multiplex panels.

The panel hybridization, immobilization, imaging and counting of the barcodes was performed in the laboratory of Prof. O. Weigert (Experimental leukemia and lymphoma research, Max-Lebsche Platz 30, 81377 Munich, Germany).

According to the manufacturer's user manual, the workflow can be briefly described as follows.

A hybridization master mix consisting of hybridization buffer (included in the nCounter® Standard Prep Pack, *NanoString Technologies*) and the Reporter CodeSet (included in the nCounter® Human PanCancer Immune Profiling Panel, *NanoString Technologies*; list of genes included in the gene expression profiling panel Appendix A) was aliquoted into each tube of a 12-tube strip (included in the nCounter® Standard Prep Pack, *NanoString Technologies*). Purified RNA samples were added to each tube. The sample input of nucleic acid did not exceed 100 ng or a total volume of 7 µL RNA per tube.

After the Capture ProbeSet (included in the nCounter® Human PanCancer Immune Profiling Panel, *NanoString Technologies*) was added to each tube, the samples were hybridized at 65°C for 16-24 h, and loaded onto the nCounter® Prep Station (nCounter® Pro Analysis System, *NanoString Technologies*).

On the Prep Station deck, the hybridized samples were purified via magnetic bead separation and immobilized to the surface of a sample cartridge (all consumables that are mandatory to run the Prep Station are included in the nCounter® Standard Cartridges, nCounter® Standard Prep Pack, and nCounter® Standard Prep Plates, *NanoString Technologies*) .

For imaging of the immobilized fluorescent reporter probes and data collection, the cartridge was transferred to the nCounter® Digital Analyser (nCounter® Pro Analysis System, *NanoString Technologies*). A Reporter Code Count file was created for each of the 12 samples in the cartridge, which served as output for data analysis using the nSolver™ 4.0 Analysis Software *(NanoString Technologies)*.

Basic analysis of the nCounter instrument data was performed in accordance to the nSolver™ Analysis user manual. The workflow includes importing the Reporter Code Count files, selecting quality control parameters, normalizing the data, and creating ratios or fold changes.

Raw data was selected for advanced analysis (nSolver™ Advanced Analysis software plugin version 2.0, *NanoString Technologies*). A quick analysis was run with default parameters, resulting in analyses of overview, normalization, and differential expression (including gene set analysis and PathView). These results were inspected for bias or outliers in the data. Samples that passed the quality control were chosen for custom analysis to explore the additional modules pathway scoring, cell type profiling, and probe descriptive.

2.2.4 RNA-*in situ* Hybridization

ACD's RNAscope® design provides an assay for highly sensitive and specific molecular detection of RNA with simultaneous spatial resolution. The RNAscope® probes are designed as double-Z oligo probe pairs that target and hybridize to a specific RNA of interest. Hybridization of a single Z probe to a non-specific RNA target will result in unstable binding and be removed during the washing steps. Only hybridization of both Z probes in tandem will ensure an intact binding site for the upcoming serial signal amplification.

As each target probe is further tagged with a specific colour detection channel (referred to as C1, C2, and C3), an Opal™ dye fluorophore (*Akoya Biosciences*, see 2.2.1) can be assigned to the channel and the amplified signal visualized under the microscope. In this manner, up to three different RNA targets can be analysed simultaneously with the RNAscope® Multiplex Fluorescent v2 assay.

2 µm thick tissue sections of FFPE bone marrow trephine biopsies were mounted on microscope glass slides and incubated overnight at 55°C in the drying cabinet (Binder World Standard Series, *TEquipment*).

On the next day, the biopsy specimen were dewaxed with xylene (2x 5 min) and rehydrated with absolute ethanol (2x 1 min). Following a 5 min drying step at RT, the tissue was incubated with hydrogen peroxidase (included in the RNAscope® H_2O_2 & Protease Plus Reagents, *ACD a Bio-Techne Brand*) for 10 min at RT in order to block endogenous peroxidase activity.

The slides were washed in ddH_2O for 2 min. Two Hellendahl staining jars, one filled with ddH_2O and the other one with 1x antigen retrieval buffer (included in the

RNAscope® Target Retrieval Reagents, *ACD a Bio-Techne Brand*), were placed into a boiling water bath. The trephine biopsy sections were pre-warmed in ddH_2O for 10 sec and then incubated in 1x antigen retrieval buffer for 30 min to unmask the antigen. To conclude the antigen retrieval procedure, the slides were transferred back to ddH2O for 10 sec to cool before being incubated in absolute ethanol for 3 min.

The bone marrow specimen were dried for 5 min at RT. To create a barrier and use less reagents during the following workflow, a diamond engraving pen *(ROTH SELECTION, Carl Roth GmbH + Co. KG)* was used to draw a permanent mark into the glass around the tissue. The slides were stored at RT until the next day.

On the following day, the sections were incubated with protease reagent (included in the RNAscope® H_2O_2 Protease Plus Reagents, *ACD a Bio-Techne Brand*) for 15 min at 40°C in an hybridization oven (Mini-hybridization oven, *Biometra*). The protease treatment optimizes permeabilization and enables the RNAscope® probes to better access the target RNA. All incubation steps were performed in a humidified chamber (Staining Chamber StainTray™ Black lid, *Carl Roth GmbH + Co. KG*) with the biopsy specimens shielded from light throughout the workflow. The slides were washed 2x 2 min in ddH_2O with agitation.

The tissue was covered in the RNAscope® probe of interest (RNAscope® Probe Hs-EZH2, RNAscope® Probe Hs-GATA2, RNAscope® Hs-IKZF2, RNAscope® Hs-LYL1, or RNAscope® Hs-RUNX1, *ACD a Bio-Techne Brand*) for 2 h at 40°C in the hybridization oven. If two RNAscope® probes were to be detected simultaneously, the slides were incubated in freshly prepared co-detection probe solution for 2 h at 40°C in the hybridization oven.

Unless otherwise specified, the following steps are identical for detecting a single probe or co-detection of two probes.

After the trephine biopsy sections were washed in 1x wash buffer with agitation (2x 2 min), they were incubated in Amp1 reagent (included in the RNAscope® Multiplex Fluorescent Detection Kit v2, *ACD a Bio-Techne Brand*) for 30 min at 40°C in the hybridization oven.

The slides were washed 2x 2 min in 1x wash buffer with agitation, and covered with Amp2 reagent (included in the RNAscope® Multiplex Fluorescent Detection Kit v2, *ACD a Bio-Techne Brand*) for 30 min at 40°C in the hybridization oven.

The washing procedure was repeated, and the biopsy specimen were incubated in Amp3 reagent (included in the RNAscope® Multiplex Fluorescent Detection Kit v2, *ACD a Bio-Techne Brand*) for 15 min at 40°C in the hybridization oven.

After washing the tissue sections in 1x wash buffer with agitation (2x 2 min), they were covered with HRP-C1 reagent (included in the RNAscope® Multiplex Fluorescent Detection Kit v2, *ACD a Bio-Techne Brand*) for 15 min at 40°C in the hybridization oven.

The bone marrow specimen were washed 2x 2 min in 1x wash buffer with agitation, and incubated in Opal™ 570 single probe working solution for 30 min at 40°C in the hybridization oven. For co-detection of two probes, the slides were incubated in Opal™ 570 co-detection working solution instead. All Opal™ solutions were prepared shortly before their use.

The washing steps were repeated. For detection of a single probe, the trephine biopsy sections were counterstained with DAPI working solution for 5 min at RT. After rinsing in ddH_2O, the tissue was sealed with a coverslip and mounting medium. All stained slides were stored in a slide box at 4°C.

The workflow for the co-detection protocol continues as follows.

The biopsy specimen were covered with HRP Block reagent (included in the RNAscope® Multiplex Fluorescent Detection Kit v2, *ACD a Bio-Techne Brand*) for 15 min at 40°C in the drying cabinet.

The slides were washed 2x 2 min in 1x wash buffer with agitation, and incubated in HRP-C3 reagent (included in the RNAscope® Multiplex Fluorescent Detection Kit v2, *ACD a Bio-Techne Brand*) for 15 min at 40°C in the hybridization oven.

After washing the bone marrow specimen in 1x wash buffer with agitation, they were incubated in Opal™ 690 co-detection working solution for 30 min at 40°C in the drying cabinet.

The washing steps were repeated. The tissue was counterstained with DAPI working solution for 5 min at RT, briefly rinsed in ddH_2O, sealed with a coverslip and mounting medium, and stored in a slide box at 4°C.

Multispectral slide scans were captured with the PhenoImager™ HT Automated Quantitative Pathology Imaging System *(Akoya Biosciences)*. Using the Phenochart™ Whole Slide Viewer *(Akoya Biosciences)*, regions of interest were annotated.

Following acquisition of the MSI scans, unmixing and autofluorescence correction of the images was conducted with the inForm® Automated Image Analysis Software Package *(Akoya Biosciences)*. The digital pathology image analysis software HALO® 3.3, including HALO AI™ 3.3 *(Indica Labs)* was used for quantitative analysis.

Following the recommendations in the user guide, the HALO® module FISH-IF v2.1.2 *(Indica Labs)* was used to create a custom algorithm as briefly described below.

The working magnification was increased to 40x to ensure optimal algorithm performance when analysing small structures such as the RNA probes used for RNA-*in situ* hybridization.

Following visual quality control of the MSI, the dyes for quantification were defined, and each corresponding fluorophore was assigned to the nuclear counterstain and the RNAscope® probe(s) of interest.

A HALO® AI Nuclear Phenotyper for fluorescence images was created and optimized for nuclei detection and nuclear segmentation. Cell membrane and cytoplasm compartments were segmented, and positivity thresholds were set for each stain or probe individually. Different phenotypes were created as needed for analysis.

The results were exported in tabular form and the data was processed for graphical presentation and statistical analysis in GraphPad Prism, version 9.5.0 *(GraphPad Software Inc.)*.

2.2.5 Cell Culture

2.2.5.1 Subculturing

All cell lines were incubated in a controlled environment at 37°C, with a 5% CO_2-enriched air atmosphere (HERAcell® 150, *Kendro Laboratory Products GmbH*).

Under sterile conditions (Safe 2020 Microbiological Safety Cabinet, *Thermo Fisher Scientific*), K-562 cells were cultured in RPMI Medium 1640 *(Thermo Fisher Scientific)*, supplemented with 10% fetal bovine serum and 1% penicillin streptomycin solution. KG-1 cells were cultured in Iscove's Modified Dulbecco's Medium *(Thermo Fisher Scientific)*, supplemented with 20% fetal bovine serum.

The suspension cultures were maintained through the periodic introduction of fresh medium or complete replacement, occurring approximately twice per week. Cell density was maintained below 1 x 10^6 viable cells/mL.

2.2.5.2 PMA Stimulation

The incubated cells were collected and resuspended in fresh medium. For cell counting, a mixture of cells and trypan blue dye (Trypan Blue Dye 0.40%, *Bio-Rad Laboratories Inc.*) in a 1:1 ratio was prepared. The TC20 automated cell counter (*Bio-Rad Laboratories Inc.*) was used to determine the total cell count and cell viability.

The PMA stock solution was diluted with cells in medium to create the final PMA working solutions (10 µM, 1 µM, 100 nM, 10 nM, and 1 nM). PMA stimulation was conducted in a 6-well plate format with a cell concentration of 500 000 cells/mL and a total volume of 5 mL/well.

Stimulated cells were incubated for 48 h or 72 h at 37°C in a 5% CO_2-enriched air atmosphere (HERAcell® 150, *Kendro Laboratory Products GmbH*) until harvesting for subsequent protein isolation.

2.2.5.3 Protein Isolation

Shortly before the cellular isolation, 1x cell lysis buffer was prepared, and 1x PBS was cooled on ice to optimize working conditions.

The suspension cells underwent centrifugation at 1800 rounds per minute (rpm) for 3 min (Centrifuge 5417, *Eppendorf*), the supernatant was aspirated, and the remaining cell pellet was washed with ice-cold 1x PBS. The centrifugation and aspiration process was repeated, followed by the addition of 1x cell lysis buffer to the pellet. The cells were then incubated on ice for 15 min and subsequently centrifuged at 4°C for 15 min at 10000 rpm (Centrifuge 5810, *Eppendorf*).

The resulting supernatant was stored at -20°C for short-term preservation, and transferred to -80°C for long-term storage.

2.2.6 Western Blot Analysis

The western blot analysis involves distinct steps aimed at precise and sequential protein handling. The following subsections delineate each step of this procedure, elucidating the execution of the Bradford assay, SDS gel electrophoresis, semi-dry blotting, and immunodetection.

2.2.6.1 Bradford Assay

The Bradford assay was employed to quantify the total protein content following isolation from cell culture material, ensuring accurate loading for subsequent electrophoretic separation. The inclusion of Coomassie Blue dye in the Bradford reagent facilitates specific binding to proteins, resulting in a colour change directly proportional to the protein concentration in the sample.

A series of BSA standards, spanning known concentrations, served as a reference to establish a standard curve correlating absorbance (reflecting colour change) with actual protein concentrations. To adhere to the linear range of the standard curve, protein samples were appropriately diluted (1:10 in 1x PBS). Dilution helps prevent potential saturation that could lead to inaccurate absorbance readings. Furthermore, 0.01% Triton X-100 and 1x PBS were introduced to the diluted samples.

The Bradford reagent, diluted at a ratio of 1:4 in 1x PBS, was subsequently added to both protein samples and BSA standards. Following a 5 min incubation at RT, the samples and standards were transferred to a 96-well plate. Spectrophotometric measurement of absorbance at a wavelength of 595 nm (iMark™ microplate absorbance reader, *Bio-Rad Laboratories Inc.*) was then conducted to quantify the colour change in each well. This information was used to obtain the protein concentrations [µg/µL] for the respective samples.

2.2.6.2 SDS Gel Electrophoresis

SDS gel electrophoresis was employed to enable the separation of proteins based on their molecular weights.

In the initial step, 5x sample buffer was added to 15 µg of protein, quantified using the Bradford assay. The mixture was incubated at 98°C for 5 min, ensuring effective protein solubilization and disruption of endogenous enzymatic activity.

Tailored to the molecular weight of the proteins of interest, a 10 – 20% acrylamide running gel solution was prepared and cast between two clean glass plates (utilizing the Mini-PROTEAN® Tetra Cell Casting Stand with Clamps, *Bio-Rad Laboratories Inc.*). The solution was overlayed with isopropanol and polymerized for 15 min.

The polymerized running gel was then overlayed with a 5% stacking gel. A comb was inserted into the assembled gel and polymerized for 15 min to create wells for the sample loading.

The electrophoresis cell (Mini-PROTEAN® Tetra Vertical Electrophoresis Cell for Mini Precast Gels, *Bio-Rad Laboratories Inc.*) was assembled with the handcast gels and filled with 1x SDS running buffer. The comb was removed, and each well was rinsed with 1x SDS running buffer. The appropriate volumes of protein sample and protein ladder (Precision Plus Protein Dual Color Standards, *Bio-Rad Laboratories Inc.*) were loaded on the gel, with unused wells filled with 5x sample buffer. Electrophoresis was performed at 95 V for 2.30 – 3 h (PowerPac™ HC High-Current Power Supply, *Bio-Rad Laboratories Inc.*), allowing the proteins to migrate through the gel matrix based on their molecular weights.

2.2.6.3 Semi-Dry Blotting

The transfer of separated proteins from the gel to a PVDF membrane was achieved through the utilization of a semi-dry blotting system (Trans-Blot® SD Semi-Dry Transfer Cell, *Bio-Rad Laboratories Inc.*). Post-electrophoresis, the glass plates were opened, and the stacking gel was removed, leaving solely the running gel for the subsequent blotting process.

The preparation of the hydrophobic PVDF transfer membrane (Immobilon®-P PVDF membrane, *Merck KGaA*) involved a sequence of activation steps: an initial 5 min incubation in methanol, followed by additional 5 min in anode buffer II. To assemble the semi-dry blotting system, 6 trimmed pieces of Whatman paper (Whatman™ 3 MM Chr, *GE HealthCare Technologies*) were soaked in anode buffer I, 3 pieces in anode buffer II, and 9 pieces in cathode buffer.

The arrangement within the blotting chamber followed a specific order from bottom to top: Whatman paper saturated in anode buffer I, followed by Whatman paper saturated in anode buffer II, the PVDF membrane, the gel obtained from electrophoresis, and lasty, Whatman paper saturated in cathode buffer. This configuration ensured the optimal transfer of proteins.

The subsequent blotting process was conducted for 80 min, maintaining a constant current of 250 mA (PowerPac™ HC High-Current Power Supply, *Bio-Rad Laboratories Inc.*).

2.2.6.4 Immunodetection

In the final step of the analysis, specific antibodies were employed to target and visualize the protein of interest.

After the completion of the blotting process, the membrane underwent a brief rinse in 1x TBST buffer before being transferred into a primary antibody solution. The primary antibody was diluted in either a 5% skimmed milk powder or a 5% BSA solution not only to facilitate optimal antibody interaction but also to serve as blocking procedure, minimizing non-specific binding.

The membrane was incubated overnight at 4°C with continuous shaking in the primary antibody solution. On the following day, the membrane was washed 3x 7 min in 1x TBST buffer. Subsequently, the membrane was transferred into a solution containing the secondary antibody, coupled to HRP, and diluted in 5% skimmed milk powder solution. The choice of rabbit or mouse secondary antibody (anti-rabbit IgG, HRP-linked or anti-mouse IgG, HRP-linked antibodies, *Cell Signaling Technology*) was made based on the species of the primary antibody, ensuring compatibility. After incubation for 1 h at 4°C with continuous shaking, the membrane was washed again 3x 7 min in 1x TBST buffer.

To visualize the protein bands via the detection of HRP, the membrane was incubated for 2 min in an enhanced chemiluminescence solution (components included in the SuperSignal™ West Pico PLUS Chemiluminescent Substrate kit, *Thermo Fisher Scientific*). The protein ladder was demarcated using the WesternSure® Pen (*LI-COR Biosciences*), and blot images were developed using the C-DiGit® blot scanner (*LI-*

COR Biosciences) equipped with the Image Studio™ software, version 5.2 (*LI-COR Biosciences*).

2.2.7 Statistical Analysis

GraphPad Prism, version 9.5.0 *(GraphPad Software Inc.)* was used for statistical analysis. The Student's *t-test* was conducted to compare the mean differences between specific patient subgroups of interest.

All reported *p*-values were calculated two-tailed. *P*-values less than .05 were considered as statistically significant and will be reported with asterisks ($p < .05$ with *, $p < .01$ with **, $p < .001$ with ***, and $p < .0001$ with ****).

3. Results

3.1 Characteristics of Pediatric Patients in the Cohort

We studied 57 children diagnosed with hematologic malignancies (Table 9). The diagnosis of RCC and MDS-EB was established in accordance to the ICC of hematologic neoplasms with germline predisposition and pediatric MDS (Arber et al., 2022; Rudelius et al., 2023).

In this cohort, 53% (30/57) carried a *GATA2* mutation (GATA2^{mut}), and 47% (27/57) were categorized as wild-type (GATA2^{WT}). Among GATA2^{mut} patients, 80% (24/30) presented with RCC and 20% (6/30) with MDS-EB. In the GATA2^{WT} group, MDS-EB represented a share of 37% (10/27).

There was no difference in age at diagnosis or sex between GATA2^{mut} and GATA2^{WT} subgroups (Table 9).

Table 9: Baseline characteristics of 57 children diagnosed with hematologic malignancies.

		GATA2^{mut} n=30	**GATA2^{WT} n=27**
Age at onset	Years, median (range)	14 (4 – 20)	9 (2 – 19)
Sex	Males, n (%)	16 (53)	16 (59)
	Females, n (%)	14 (47)	11 (41)
Diagnosis	RCC, n (%)	24 (80)	17 (63)
	MDS-EB, n (%)	6 (20)	10 (37)
Karyotype*	Normal, n (%)	9 (33)	15 (56)
	Monosomy 7, n (%)**	11 (41)	8 (30)
	Trisomy 8, n (%)	7 (26)	3 (11)
	Other, n (%)	0 (0)	1 (3)

* no information available for n=3 children in the GATA2^{mut} group

** includes monosomy 7 with additional aberrations

GATA2^{mut}: *GATA2* mutation, GATA2^{WT}: *GATA2* wild-type

Monosomy 7 was the predominant cytogenetic lesion in GATA2^{mut} patients (41%, 11/27), compared to the GATA2^{WT} cohort (30%, 8/27; Table 10). Assessing the prevalence of monosomy 7 in both subgroups, we found an almost equal distribution between RCC and MDS-EB in GATA2^{mut} patients (45%, 5/11 versus 55%, 6/11), whereas this karyotype was more present in RCC in patients with GATA2^{WT} (63%, 5/8). In GATA2^{mut} patients with the diagnosis MDS-EB, monosomy 7 was the prevailing cytogenetic abnormality (100%, 6/6).

A normal karyotype was more frequent in the GATA2^{WT} group, compared to GATA2^{mut} patients (56%, 15/27 in GATA2^{WT} versus 43%, 9/21 in GATA2^{mut}; Table 10). In the GATA2^{mut} cohort, this karyotype was exclusively present in RCC. Among GATA2^{WT} patients in contrast, a normal karyotype appeared in RCC and MDS-EB, and presented as the predominant karyotype in both diagnoses (65%, 11/17 in RCC versus 40%, 4/10 in MDS-EB). Please refer to Appendix B for a detailed overview of mutational data of pediatric patients with GATA2 deficiency in the cohort.

Table 10: Cytogenetic abnormalities in pediatric patients with hematologic malignancies.

	Karyotype	Patients, n (%)	RCC, n	MDS-EB, n
GATA2^{mut*}	Normal	9 (33)	9	0
	Monosomy 7	11 (41)	5	6
	Trisomy 8	7 (26)	7	0
GATA2^{WT}	Normal	15 (56)	11	4
	Monosomy 7	8 (30)	5	3
	Trisomy 8	3 (11)	1	2
	Random aberration	1 (3)	0	1

* no information available for n=3 children

3.2 Disturbed Hematopoiesis in the Microenvironment of Patients with GATA2 Deficiency

The clinical presentation, as well as the histomorphology of the bone marrow in patients with GATA2 deficiency exhibit significant variations in terms of cellularity, dysplasia of the hematopoiesis, and cell differentiation. Therefore, we conducted a

systematic hematopathological assessment of the trilinear hematopoiesis, incorporating cytogenetic characteristics, with a particular emphasis on the quantitative and qualitative composition of individual cell types. To achieve a comprehensive phenotyping of cells with simultaneous spatial resolution, we used mIF in conjunction with multispectral image analysis. This technique enabled us to visualize up to six different antigens plus DAPI on a single slide of FFPE bone marrow sections. Please refer to Appendix C, Table C 1 for a detailed list of all mIF panels and their composition.

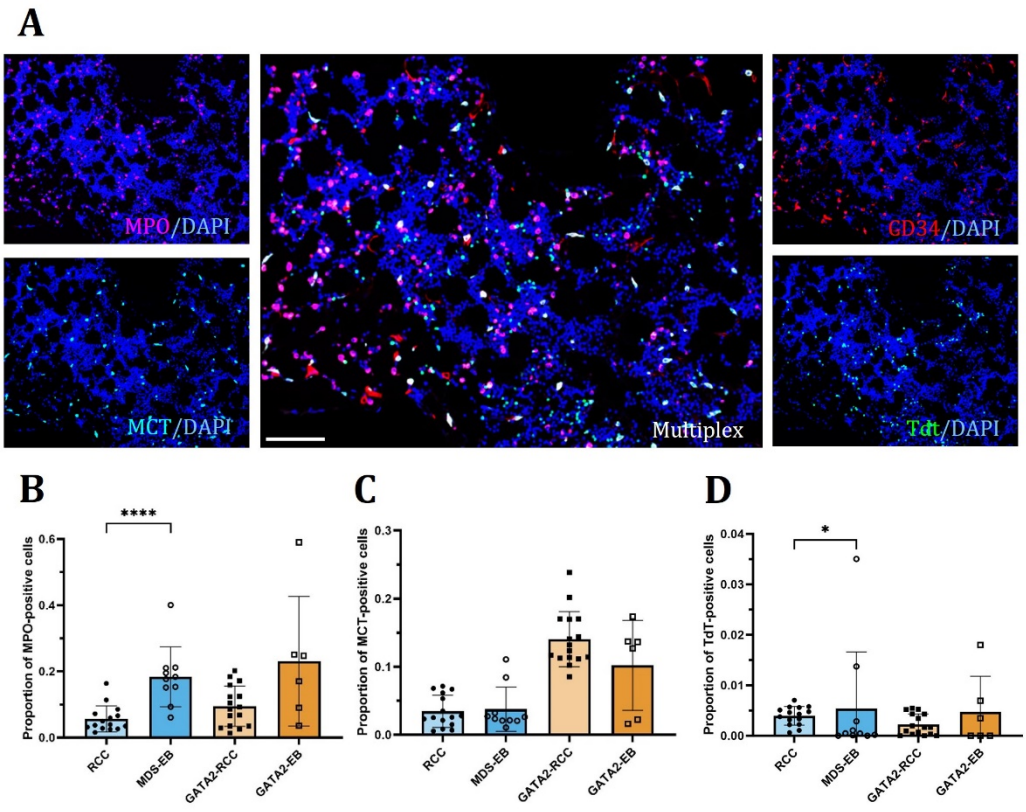

Figure 1: Characterization of myeloid cells, mast cells, and hematogonic cells in the bone marrow. Multiplex immunofluorescence (mIF) image **(A)** for myeloid cells (MPO, magenta), mast cells (MCT, cyan), hematopoietic progenitors (CD34, red), and hematogonic cells (TdT, green). The scale bar corresponds to 100 µm, DAPI staining in blue. Quantification of MPO-positive cells **(B)** showed reduced expression in patients at early disease stages, specifically refractory cytopenia of childhood (RCC) and those with additional *GATA2* mutation (GATA2-RCC). With disease progression to myelodysplastic syndrome with excess blasts (MDS-EB) or advanced GATA2 deficiency (GATA2-EB), MPO expression was increased (MDS-EB **** $p < .0001$). Patients with *GATA2* mutations ($GATA2^{mut}$) exhibited increased levels of MCT-positive cells **(C)** compared to GATA2 wild-type ($GATA2^{WT}$). TdT-positive cells **(D)** were slightly upregulated in MDS-EB (* $p < .05$) but represent an overall negligible cell population in our cohort.

In panel A (Figure 1), we investigated the myeloid cell population (myeloperoxidase, MPO), mast cells (tryptase alpha/beta 1, MCT), hematopoietic progenitors (CD34 molecule, CD34), and hematogonic cells (DNA nucleotidylexotransferase, TdT). The expression levels of each cell type were quantified and compared among the patients in our cohort. Quantification of myeloid cells revealed a significant increase in patients with MDS-EB compared to individuals with RCC (mean ± standard deviation (SD) 0.1837 ± 0.09063 in MDS-EB versus 0.05659 ± 0.03975 in RCC; $p < .0001$). In GATA2^{mut} patients, the expression levels of myeloid cells increased slightly with disease progression, although with considerable variations observed in GATA2-EB patients (mean ± SD in GATA2-EB 0.2308 ± 0.1956 versus 0.09494 ± 0.06104 in GATA2-RCC).

Regarding mast cells, patients without GATA2 deficiency showed lower expression compared to GATA2^{mut} patients (Figure 1). Additionally, the proportion of positive cells was comparable between RCC and MDS-EB (mean ± SD in RCC 0.03435 ± 0.02363; in MDS-EB 0.03775 ± 0.03255). Notably, GATA2-RCC patients exhibited a slightly higher proportion of mast cells compared to GATA2-EB patients, albeit not reaching statistical significance (mean ± SD in GATA2-RCC 0.1403 ± 0.04037 versus 0.1020 ± 0.06608 in GATA2-EB). The mean expression levels of hematogonic cells remained below 0.6% across all four patient groups, regardless of the *GATA2* mutational status, with a slight upregulation in the MDS-EB group (mean ± SD in MDS-EB 0.005396 ± 0.01123 versus 0.003950 ± 0.001850 in RCC; $p < .05$).

The presence of megakaryocytes (glycoprotein Ib platelet subunit alpha, CD42b), dendritic cells (interleukin 3 receptor subunit alpha, CD123), T lymphocytes (CD3 epsilon subunit of T cell receptor complex, CD3), and monocytes (CD14 molecule, CD14) was assessed in panel B (Figure 2). The proportion of megakaryocytes remained relatively low in all four patient groups, with a significant upregulation observed in MDS-EB (mean ± SD in MDS-EB 0.005336 ± 0.003796 versus 0.001502 ± 0.001217 in RCC; $p < .05$). Also in GATA2^{mut} patients, the expression of megakaryocytes showed a slight increase with disease progression, although we observed some variation within the GATA2-EB group (mean ± SD in GATA2-EB 0.01235 ± 0.02288 versus 0.001673 ± 0.0006584 in GATA2-RCC).

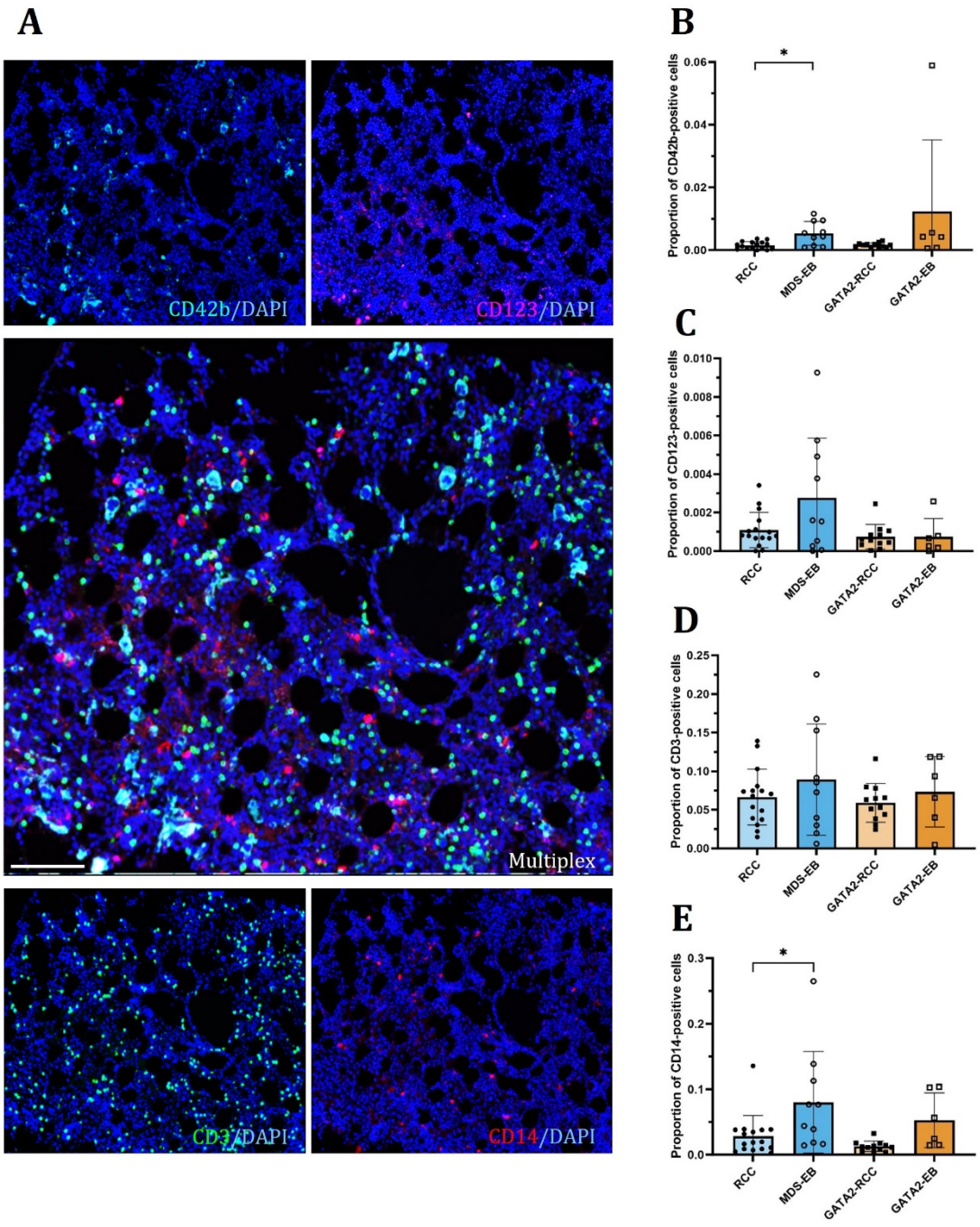

Figure 2: Quantification of megakaryocytes, dendritic cells, T lymphocytes, and monocytes in the bone marrow. mIF image **(A)** for megakaryocytes (CD42b, cyan), dendritic cells (CD123, magenta), T lymphocytes (CD3, green), and monocytes (CD14, red). The scale bar corresponds to 100 µm, DAPI staining in blue. Quantification of CD42b-positive cells **(B)** showed relatively low expression levels, with a slight upregulation in MDS-EB (* $p < .05$). GATA2^{mut} patients exhibited reduced expression of CD123-positive cells **(C)** compared to GATA2^{WT} patients. The expression of CD3 **(D)** remained comparable across all four patient groups. Quantification of CD14-positive cells **(E)** demonstrated an upregulation with disease progression, specifically significant in GATA2^{WT} patients (MDS-EB * $p < .05$).

Quantification of dendritic cells revealed mean expression levels below 0.3% in all patient groups, with the highest expression in MDS-EB (mean ± SD in MDS-EB 0.002766 ± 0.003088) and very low expression in GATA2^{mut} patients (mean ± SD in GATA2-RCC 0.0007338 ± 0.0006391; in GATA2-EB 0.0007406 ± 0.0009465; Figure 2). The proportion of T lymphocytes remained comparable between patients with GATA2 deficiency and those without. The expression of monocytes was significantly increased with disease progression in patients with GATA2^{WT} (mean ± SD in MDS-EB 0.08010 ± 0.07733 versus 0.02829 ± 0.03166 in RCC; $p < .05$), while GATA2^{mut} patients exhibited only a slight increase (mean ± SD in GATA2-EB 0.05265 ± 0.04186 versus 0.01276 ± 0.007720 in GATA2-RCC).

IHC stainings for B lymphocytes (membrane spanning 4-domains A1, CD20), eosinophilic granulocytes (eosinophil peroxidase, EPX), and proliferating cells (marker of proliferation Ki-67, Ki-67), completed the comprehensive phenotyping of cells in the bone marrow (Figure 3). Please refer to Appendix C, Table C 2 for a detailed list of all IHC markers used in this study. In line with previous findings demonstrating a loss of B cells in GATA2 deficiency (Dickinson et al., 2011; Nováková et al., 2016), GATA2^{mut} patients in our cohort exhibited a very low expression of B lymphocytes (mean ± SD in GATA2-RCC 0.03029 ± 0.06640; in GATA2-EB 0.02543 ± 0.02965) compared to patients with GATA2^{WT} (mean ± SD in RCC 0.1030 ± 0.1203; in MDS-EB 0.04272 ± 0.05396).

The expression levels of eosinophilic granulocytes did not show substantial variation between GATA2-RCC and GATA2-EB, while MDS-EB patients displayed slightly higher expression levels compared to children with RCC (mean ± SD in MDS-EB 0.08111 ± 0.09496 versus 0.02507 ± 0.01687 in RCC; Figure 3). Ki-67 staining identified approximately 40 - 55% of evaluated cells as proliferating in all four patient groups (mean ± SD in RCC 0.5456 ± 0.2310; in MDS-EB 0.5093 ± 0.2309; in GATA2-RCC 0.4021 ± 0.2792; in GATA2-EB 0.4474 ± 0.2462). Notably, there was considerable variation in the proportion of proliferating cells of individual patients within each group.

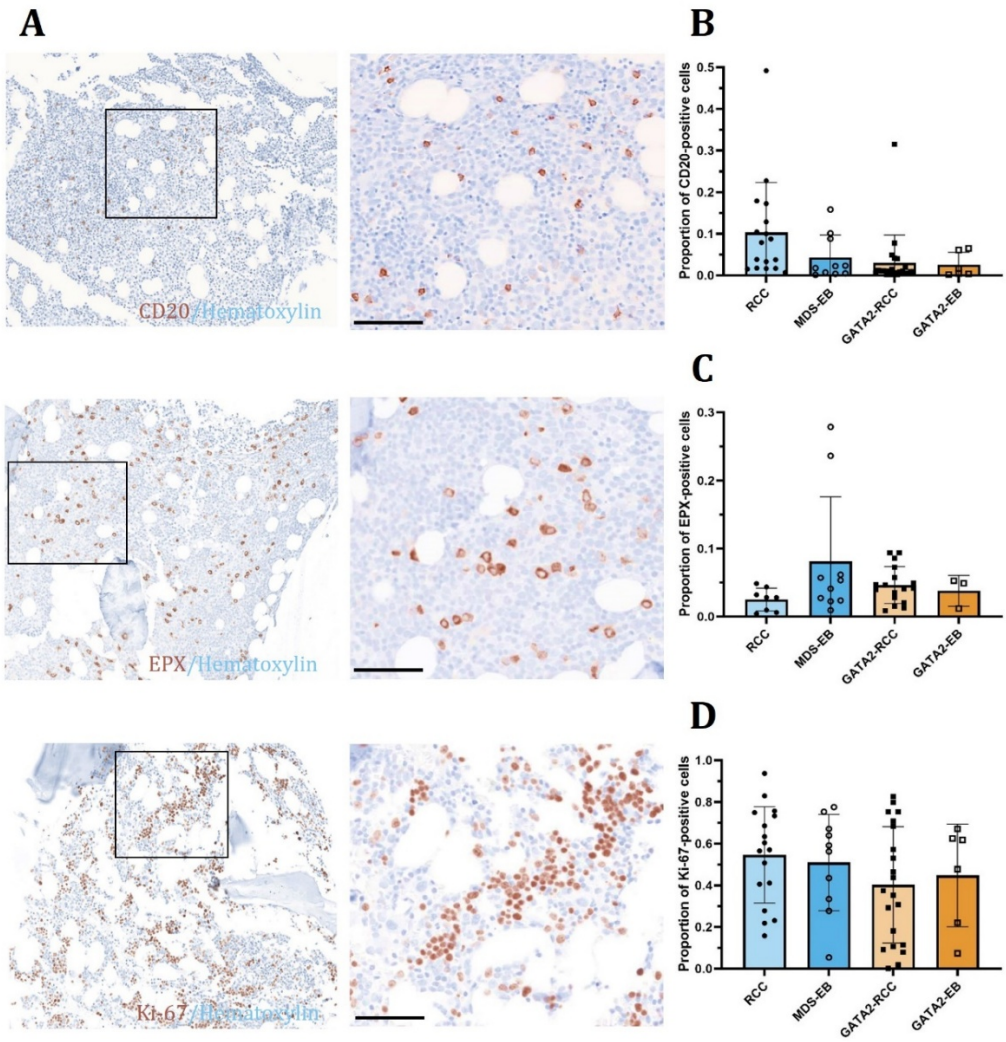

Figure 3: Distribution of B lymphocytes, eosinophilic granulocytes, and proliferating cells. Overview of immunohistochemistry **(A)** for B lymphocytes (CD20, brown, upper panel), eosinophilic granulocytes (EPX, brown, middle panel), and proliferating cells (Ki-67, brown, lower panel), hematoxylin counterstaining in blue. Magnified inlets are shown on the right, scale bar 50 µm. Patients with GATA2 deficiency demonstrated a diminished expression of CD20-positive cells **(B)** compared to GATA2^{WT} patients. The expression levels of eosinophilic granulocytes **(C)** and proliferating cells **(D)** remained relatively uniform in the cohort.

Patients affected by GATA2 deficiency demonstrate a higher incidence of monosomy 7 compared to those with GATA2^{WT} (Wlodarski et al., 2016). Furthermore, the prevalence of monosomy 7 aligns with its recognition as one of the most common chromosomal aberrations in the pediatric population, a pattern that resonates in our study where monosomy 7 is detected in 41% of GATA2^{mut} cases (Table 9).

This occurrence led us to undertake a focused analysis, investigating potential variations in the expression of distinct cell populations based on patient karyotypes.

Specifically, we conducted a comparative examination of expression profiles between individuals presenting with monosomy 7 in one disease group and those characterized by alternative karyotypic alterations, encompassing trisomy 8, normal karyotype, or other random aberrations.

When comparing patients with monosomy 7 to those with other karyotypes, we observed no substantial differences in the expression levels of major cell types in the bone marrow (refer to Appendix D, Figure D 1 - Figure D 3). However, within the subset of MDS-EB patients, those affected by monosomy 7 exhibited considerable variation in the expression levels of cells positive for TdT, CD123, CD3, CD14, and EPX. Remarkably, in patients with RCC, regardless of the *GATA2* mutational status, the impact of the karyotype on expression patterns appeared less pronounced as individuals with monosomy 7 displayed comparable levels to those with diverse karyotypes.

3.3 Transcriptome Analysis Reveals *BCL2* and *CCL18* as Novel Targets of Interest with High Expression in GATA2-EB Patients

GATA2 deficiency not only increases the susceptibility to myeloid neoplasia, but also leads to dysregulation of the bone marrow niche and alters the composition of the immune microenvironment (Calvo et al., 2011; Nováková et al., 2016). The magnitude of disruption within the hematopoietic niche and the specific contribution of external factors to the development of MDS remain elusive. To further address this, we employed gene expression profiling on a small subset of patients in the cohort using NanoString's nCounter® platform. By leveraging this technology, we sought to acquire preliminary insights into the transcriptional network and the multifaceted interplay between hematopoiesis and the hematopoietic niche.

16 patients of the cohort, comprising 8 patients with MDS-EB, 5 patients with GATA2-EB, and 3 patients with GATA2-RCC, were subjected to RNA isolation, followed by gene profiling using the nCounter® Human PanCancer Immune Profiling Panel (*NanoString Technologies*), which encompasses a comprehensive set of 770 genes (please refer to Appendix A for a complete list of the included genes).

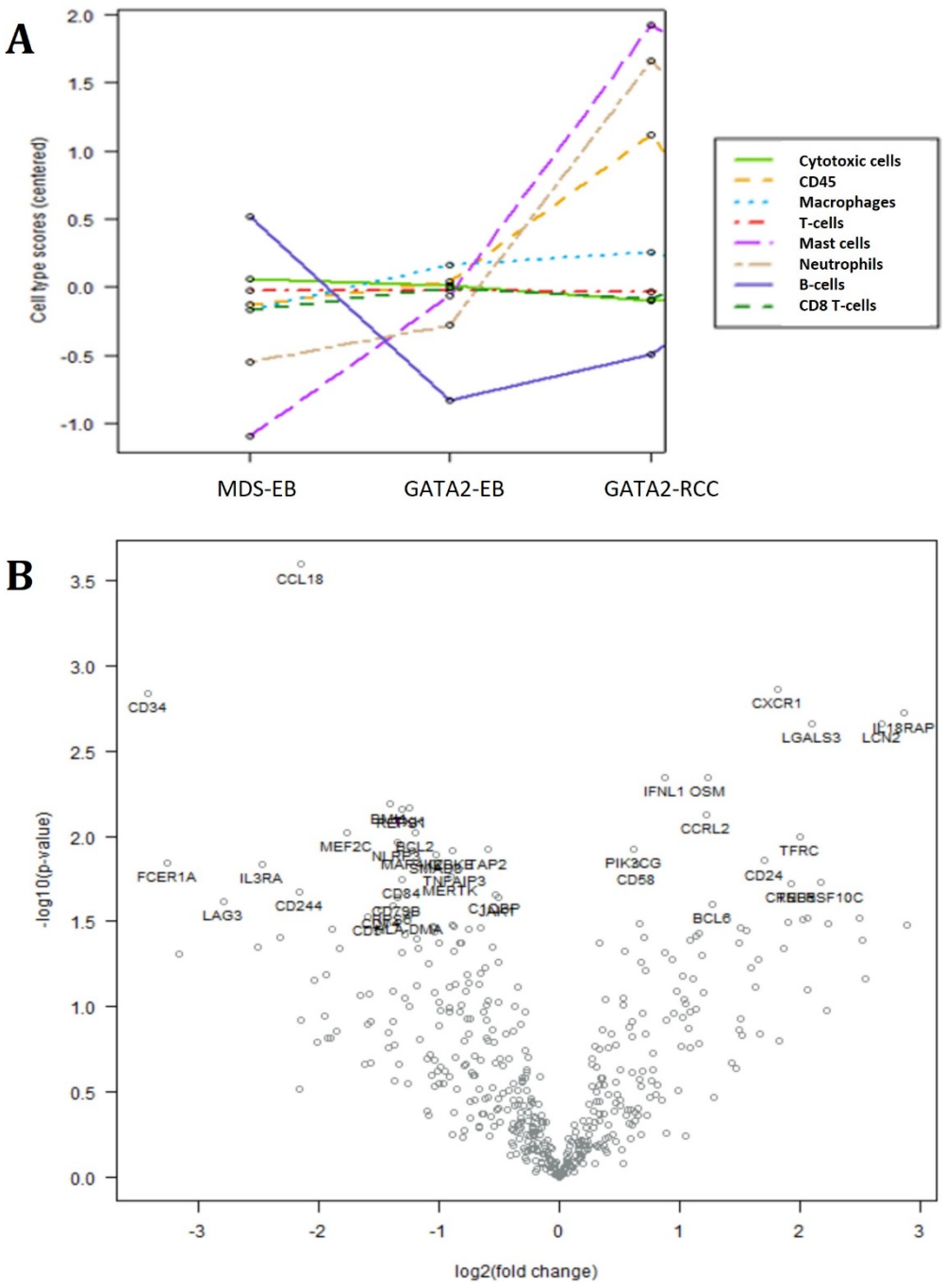

Figure 4: Insights into gene expression profiling on a subset of patients in the cohort. 8 patients with MDS-EB, 5 patients with GATA2-EB, and 3 patients with GATA2-RCC, were subjected to gene expression profiling following RNA isolation. The cell type profiling module provides an overview of cellular populations **(A)** in the bone marrow with cell type scores corresponding to abundance estimates of the raw cell type measurements. A higher abundance of B cells was observed in MDS-EB compared to GATA2-RCC and GATA2-EB. Additionally, the abundance of mast cells showed an increasing trend from MDS-EB to GATA2-EB, reaching its peak in GATA2-RCC. Visualization of the volcano plot **(B)** for identification of differential expression in GATA2-RCC compared to the baseline of GATA2-EB. Genes with differential expression fall to either side of the graph. Genes with statistically significant differential expression would be positioned above horizontal lines.

To assess the abundance of different cell populations among the patient groups, we utilized the cell type profiling module (Figure 4). This advanced analysis module applies the method described by Danaher et al. (Danaher et al., 2017), which quantifies cell populations based on marker genes known to be explicitly and stably expressed in particular cell types. The raw cell type measurement generates abundance estimates, represented as cell type scores, calculated as the mean $\log_2$ normalized counts of the cell type-specific markers.

Consistent with previous findings indicating a decrease of B cells in GATA2 deficiency (Dickinson et al., 2011; Nováková et al., 2016), we observed a higher abundance of B cells in MDS-EB compared to both the GATA2-EB and GATA2-RCC groups (Figure 4). Interestingly, the most prominent change across the patient groups was found in the mast cell population, which exhibited an escalated expression level from MDS-EB to GATA2-EB and reached its peak in GATA2-RCC patients. A relatively smaller increase in expression, from GATA2-EB to GATA2-RCC, was observed for neutrophils and CD45-positive cells. Conversely, other measured cell types displayed a relatively comparable abundance across all three patient groups.

Furthermore, we employed the differential expression module to identify genes exhibiting altered expression patterns between GATA2-RCC and GATA2-EB patients. Visual representation was achieved through the use of a volcano plot, wherein the $-\log_{10}$ (corresponding to the *p*-value) is plotted against the $\log_2$ fold change for each gene in GATA2-RCC compared to the baseline of GATA2-EB (Figure 4). Genes demonstrating substantial differential expression are positioned at either side of the graph, while genes exhibiting high statistical significance are positioned above horizontal lines, representing *p*-value thresholds adjusted using the Benjamini-Yekutieli method to account for multiple comparisons. It is worth noting that the plot lacks explicit thresholds, rendering the data points devoid of significant *p*-values.

Nevertheless, our analysis revealed that *CD34*, positioned prominently to the left of the graph, ranked as the third most differentially expressed gene with decreased expression in GATA2-RCC compared to GATA2-EB (Table 11). This observation aligns with biological reasoning, as patients in advanced disease stages typically exhibit an elevation in CD34-positive blasts. Thus, this information provides valuable

validation of the method, albeit acknowledging that the results should be interpreted with caution.

Therefore, we compiled a list of the top 15 differentially expressed genes in GATA2-RCC versus GATA2-EB, intending to identify novel targets of interest for further validation at the protein level using mIF in the comprehensive cohort of 57 patients (Table 11). Among these differentially expressed genes, C-C motif chemokine ligand 18 (*CCL18*) and BCL2 apoptosis regulator (*BCL2*) sparked our interest.

Table 11: List of the 15 most differentially expressed genes in GATA2-RCC versus GATA2-EB patients.

Top 15 differentially expressed genes in GATA2-RCC versus GATA2-EB					
1	*CCL18**	**6**	*LGALS3***	**11**	*REPS1**
2	*CXCR1***	**7**	*OSM***	**12**	*CCRL2***
3	*CD34**	**8**	*IFNL1***	**13**	*MEF2C**
4	*IL18RAP***	**9**	*BMI1**	**14**	*BCL2**
5	*LCN2***	**10**	*TXK**	**15**	*TRFC***

* decreased expression in GATA2-RCC

** increased expression in GATA2-RCC

Subsequent mIF stainings revealed an upregulation of CCL18 with disease progression in GATA2^{mut} patients (mean ± SD 0.3420 ± 0.07909 in GATA2-EB versus 0.1157 ± 0.04637 in GATA2-RCC; $p < .0001$; Figure 5). Notably, elevated levels of CCL18 were also observed in MDS-EB, albeit to a lesser extent (mean ± SD 0.1514 ± 0.04917 in MDS-EB versus 0.1004 ± 0.02994 in RCC; $p < .05$).

BCL2 expression exhibited a substantial upregulation in GATA2-EB compared to GATA2-RCC (mean ± SD 0.2980 ± 0.09923 in GATA2-EB versus 0.05252 ± 0.03191 in GATA2-RCC; $p < .001$; Figure 5). Moreover, when compared to all other patient groups, BCL2 expression manifested most prominently in GATA2-EB (mean ± SD in MDS-EB 0.08308 ± 0.04836; in RCC 0.03574 ± 0.02431; $p < .05$).

Further examination of karyotypic influences on CCL18 and BCL2 expression is detailed in Appendix D, Figure D 4. Notably, patients with monosomy 7 displayed no significant variance in the expression of these two proteins when contrasted with individuals possessing alternate karyotypes.

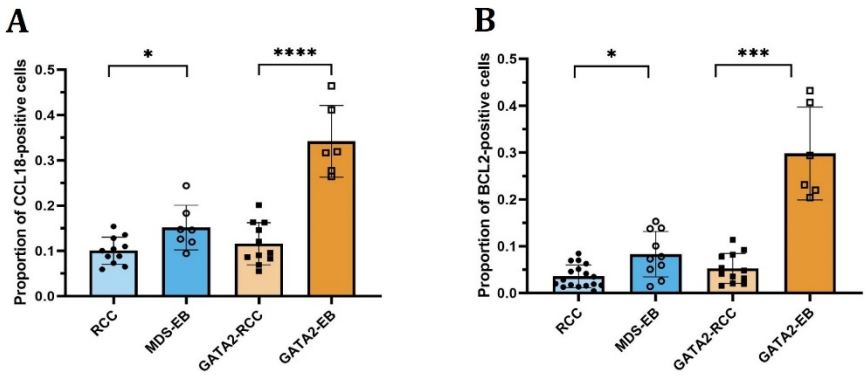

Figure 5: Validation of the differentially expressed genes *CCL18* and *BCL2* as novel targets of interest at protein level. Quantification of CCL18-positive cells **(A)** demonstrated a strong upregulation with disease progression in GATA2 deficiency (**** $p < .0001$) and a slight upregulation in GATA2^{WT} patients (* $p < .05$). Expression of BCL2 **(B)** was significantly increased in GATA2-EB (*** $p < .001$) compared to MDS-EB (* $p < .05$). GATA2-EB patients showed the most prominent BCL2 levels compared to all other disease groups.

3.4 Dysregulation of GATA2 Target Genes and *GATA2* mRNA in the Hematopoietic Niche of GATA2^{mut} Patients

To complement the transcriptome analysis and achieve a more comprehensive understanding of the hematopoietic niche in the context of GATA2 deficiency, we next sought to investigate the influence of GATA2 on the hematopoietic niche and its target genes. To accomplish this, we conducted RNA-*in situ* hybridization on our cohort of pediatric patients. This chapter is a modified version of the study authored by Schreiber and colleagues (Schreiber et al., 2023), published in *Cancers* and has been reproduced here with the permission of the copyright holder.

Exploring the transcriptional network governed by GATA2, we investigated the expression patterns of four target genes known to be regulated by GATA2 (Katsumura et al., 2017). We found no significant variation in the expression of *RUNX1*, Enhancer of zeste 2 polycomb repressive complex 2 subunit (*EZH2*), Ikaros family zinc finger 1 (*IKZF1*), and LYL1 basic helix-loop-helix family member (*LYL1*) between RCC and MDS-EB patients (Figure 6). In contrast, the expression levels of all four GATA2 target genes were significantly elevated with disease progression among GATA2^{mut} patients (GATA2-EB mean ± SD of *RUNX1*-positive cells 0.29991 ± 0.1084; of *EZH2*-positive cells 0.2852 ± 0.09676; of *IKZF1*-positive cells 0.3578 ± 0.1710; and of *LYL1*-positive cells 04935 ± 0.09868; $p < .05$).

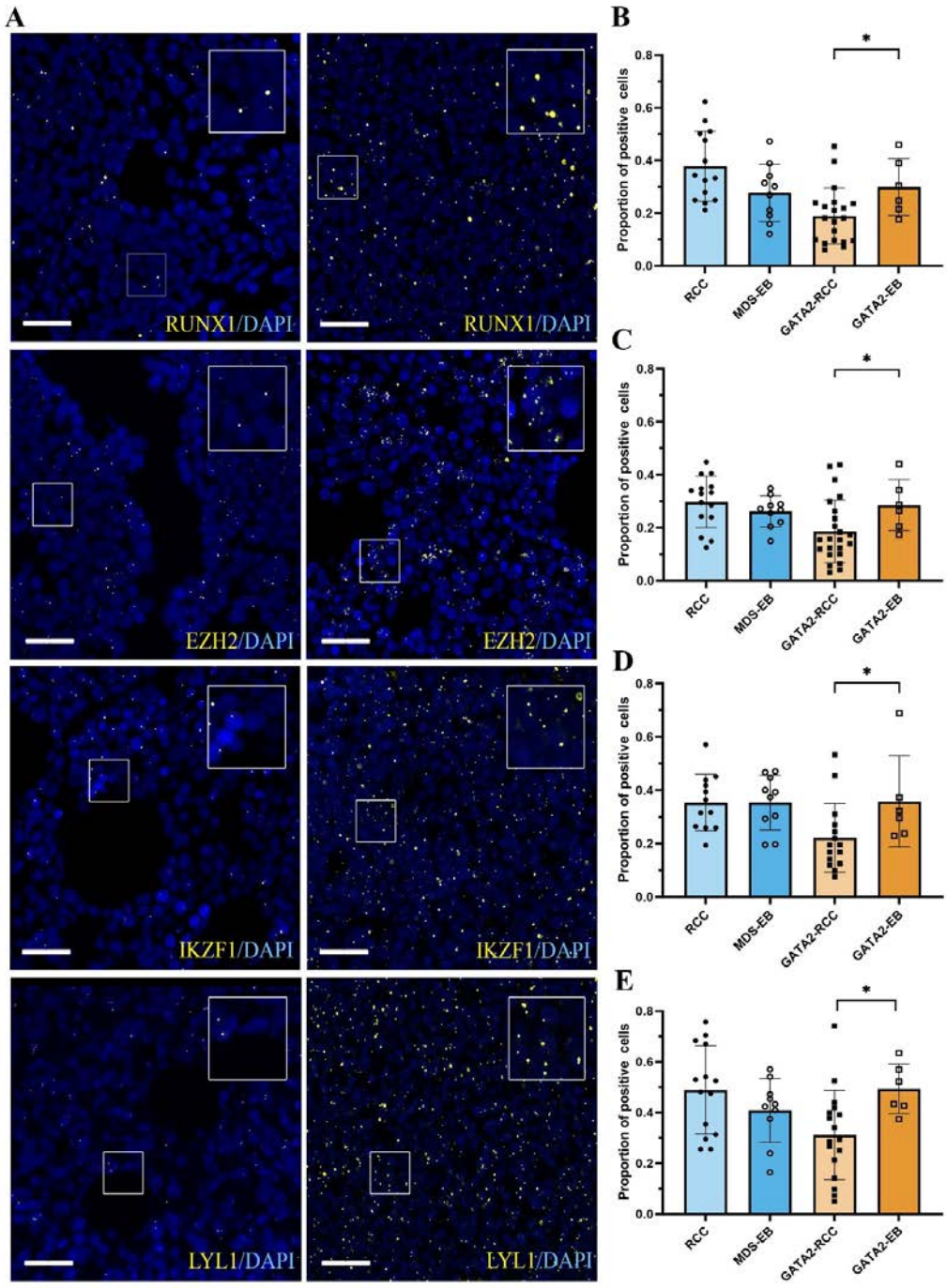

Figure 6: Elevated mRNA expression of *RUNX1*, *EZH2*, *IKZF1*, and *LYL1* with disease progression in GATA2 deficiency. RNA-*in situ* hybridization **(A)** targeting the GATA2-associated genes *RUNX1*, *EZH2*, *IKZF1*, and *LYL1* (yellow), with representative images depicting low (on the left) and high (on the right) mRNA expression, DAPI staining in blue. The scale bars correspond to 25 µm. Quantification of mRNA expression for *RUNX1* **(B)**, *EZH2* **(C)**, *IKZF1* **(D)**, and *LYL1* **(E)** exhibited uniform expression of positive cells in GATA2^{WT} patients. However, in GATA2^{mut} patients, the expression of all four GATA2 targets significantly increased with disease progression (* $p < .05$). This image was originally featured in the study authored by Schreiber and colleagues (Schreiber et al. 2023), published in *Cancers* and has been included here with the permission of the copyright holder.

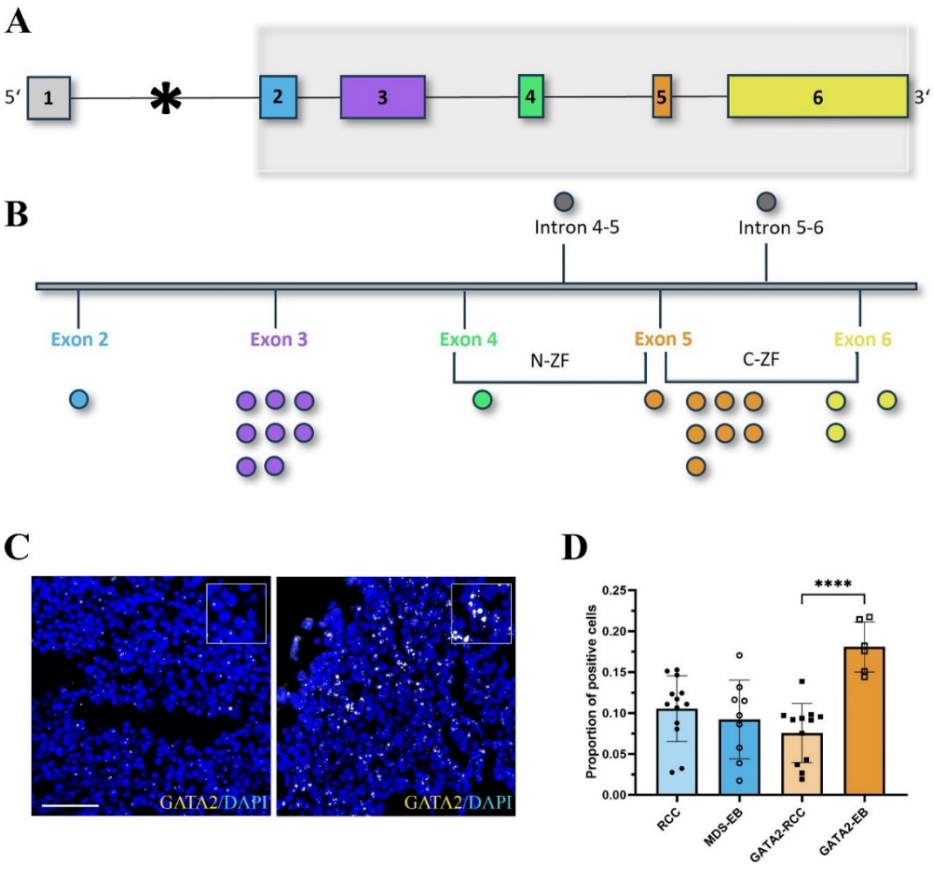

Figure 7: *GATA2* mRNA expression in the cohort and localization of *GATA2* mutations on the *GATA2* gene. Schematic overview **(A)** of transcript variant 2 (NM_032638.5) of the *GATA2* gene, with colored boxes representing exons 1-6. The asterisk denotes the binding site of the *GATA2* probe used for RNA-*in situ* hybridization. A magnified view **(B)** of exons 2-6 highlights the distribution of mutations present in our cohort within the gene. The *GATA2* probe's binding site does not interfere with the localization of the mutations. Mutations were identified in exon 2 (one mutation, blue), exon 3 (8 mutations, purple), exon 4 (one mutation, green), exon 5 (8 mutations, orange), and exon 6 (3 mutations, yellow). The N-zinc finger (N-ZF) and C-zinc finger (C-ZF) represent structural motifs on the gene. Two intronic mutations were also identified. RNA-*in situ* hybridization of *GATA2* (yellow) and DAPI staining in blue **(C)**, with a representative image depicting high (on the right) and low (on the left) mRNA expression, scale bar 25 µm. Quantification of *GATA2* mRNA expression **(D)** revealed comparable expression of *GATA2*-positive cells in patients with RCC and MDS-EB. In patients with GATA2 deficiency, *GATA2* expression significantly increased with disease progression (**** $p < .0001$). This image was originally featured in the study authored by Schreiber and colleagues (Schreiber et al. 2023), published in *Cancers* and has been included here with the permission of the copyright holder.

To establish a correlation between the expression of the four target genes and their regulator, we proceeded to assess the mRNA expression of *GATA2* (Figure 7). For this goal, a specific *GATA2* RNAscope® probe was employed, carefully designed to

circumvent any interference with distinct mutations identified within our cohort of GATA2^{mut} patients, as well as with any previously reported mutations (Sahoo et al., 2020; Wlodarski et al., 2016).

Patients without GATA2 deficiency exhibited consistent and stable levels of *GATA2* mRNA throughout both early and advanced disease stages (mean ± SD in RCC 0.1055 ± 0.04004; in MDS-EB 0.09223 ± 0.04805; Figure 7). Conversely, GATA2-RCC patients displayed a pronounced reduction in *GATA2* mRNA expression (mean ± SD 0.07559 ± 0.03603), which concurs with prior investigations documenting haploinsufficiency and dysregulation of gene expression resulting from germline mutations in the *GATA2* gene (Hahn et al., 2011; Ostergaard et al., 2011; Wlodarski et al., 2016). Intriguingly, a remarkable reinforcement of *GATA2* mRNA levels was observed in association with disease progression in GATA2-EB (mean ± SD 0.1808 ± 0.03071; $p < .0001$).

Investigating potential differences in the expression patterns of *GATA2* and its target genes among patients with monosomy 7 compared to those with different karyotypes, our analysis revealed no significant fluctuations in the proportion of cells positive for *RUNX1*, *EZH2*, *IKZF1*, *LYL1*, and *GATA2* (see Appendix D, Figure D 5).

3.5 Increased Levels of Histone H3 Trimethylation at Lysine 27 in GATA2-EB Patients Correlate with Elevated *EZH2*-Positive Hematopoietic Progenitors

To investigate the potential implications of the dysregulation in the GATA2 transcriptional network for the hematopoietic stem cell pool, we conducted a comprehensive analysis using combinatorial RNA-*in situ* hybridization. Therefore, we examined simultaneous *CD34* expression in conjunction with *RUNX1* or *EZH2*. This chapter is a modified version of the study authored by Schreiber and colleagues (Schreiber et al., 2023), published in *Cancers* and has been reproduced here with the permission of the copyright holder.

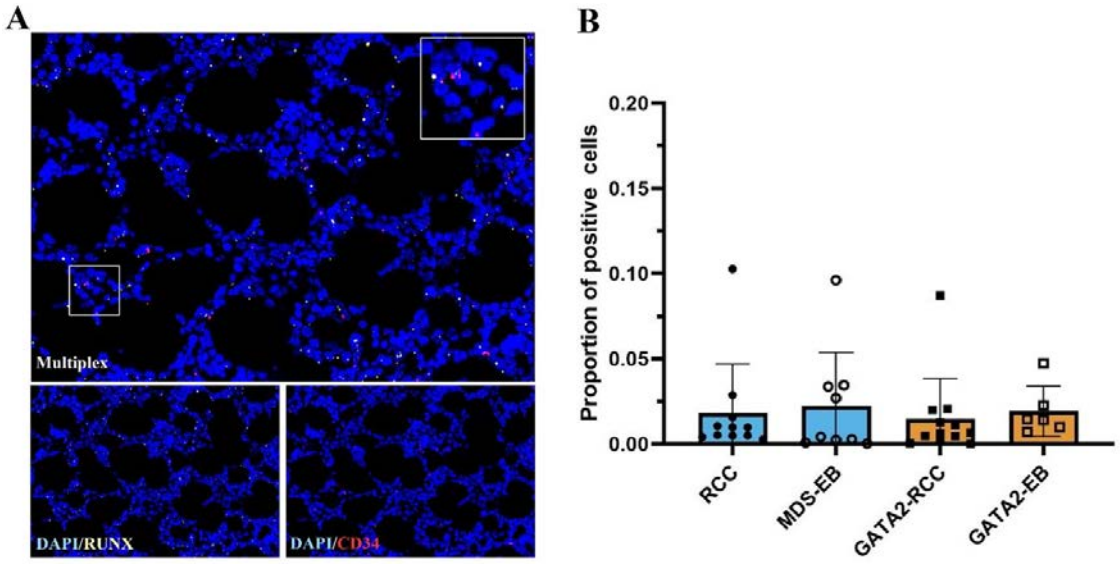

Figure 8: Uniform expression of *RUNX1*-positive hematopoietic progenitors across all patient groups. Combinatorial *in situ* hybridization **(A)** of *RUNX1* (yellow) and *CD34* (red) with DAPI staining in blue. Quantification of *RUNX1*-positive hematopoietic progenitors **(B)** revealed comparable expression levels for GATA2^{WT} and GATA2^{mut} patients. This image was originally featured in the Supplementary Data to the study authored by Schreiber and colleagues (Schreiber et al 2023), published in *Cancers* and has been included here with the permission of the copyright holder.

It is important to note that, despite the increase of blasts at the advanced disease stages MDS-EB and GATA2-EB, the expression levels of *RUNX1*-positive hematopoietic progenitors remained relatively constant across all four patient groups (Figure 8).

Interestingly, a notable elevation of *EZH2* expression in hematopoietic progenitors was found among GATA2-EB patients in contrast to their GATA2-RCC counterparts, while patients without GATA2 deficiency did not manifest this distinctive effect (mean ± SD in GATA2-EB 0.07596 ± 0.05328 versus 0.01293 ± 0.01708 in GATA2-RCC; $p < .01$; Figure 9). As such, the observed upregulation of *EZH2* expression within blasts of GATA2-EB patients cannot be simply attributed to the increased presence of hematopoietic progenitors in advanced disease.

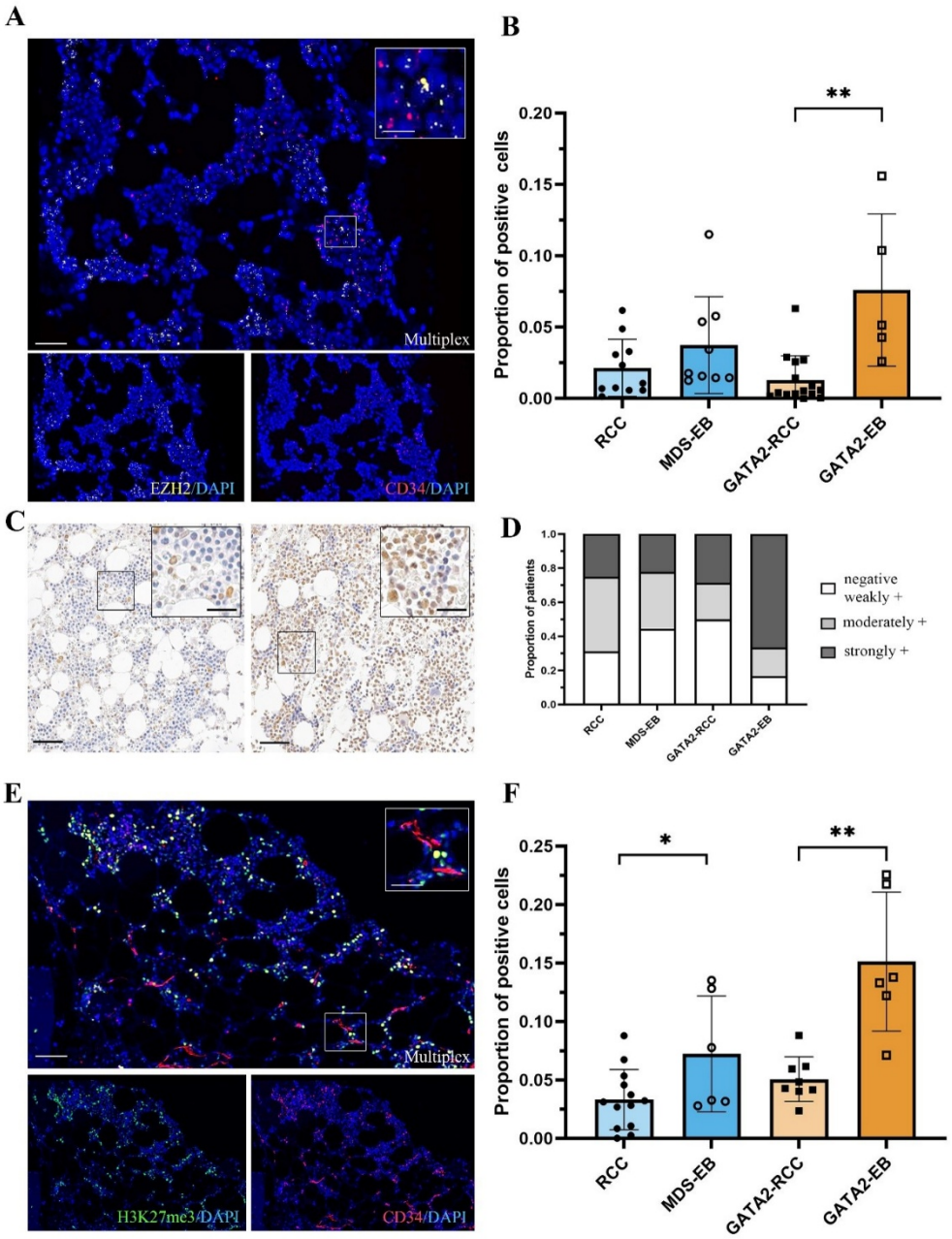

Figure 9: Enhanced *EZH2* expression in hematopoietic progenitors, correlated with elevated histone H3 trimethylation at lysine 27 (H3K27me3) with disease progression in GATA2 deficiency. Combinatorial *in situ* hybridization **(A)** of *EZH2* (yellow) and *CD34* (red) with DAPI staining in blue, scale bars 100 µm (overview) and 50 µm (magnified inlet). Quantification of *EZH2*-positive hematopoietic progenitors **(B)** demonstrated an increased expression level in GATA2-EB patients (** $p < .01$). Overview of immunohistochemistry **(C)** for H3K27me3 (brown) with representative images for strong (on the right) and weak (on the left) histone trimethylation, hematoxylin counterstaining in blue. The scale bars correspond to 100 µm for the overview and 50 µm for the magnified inlet. Visualization of the semi-quantitative immunoreactive scoring system for H3K27me3 **(D)**, with strongly positive immunoreactive scores in GATA2-EB patients and predominantly negative/weakly

H3K27me3 positivity in other patient groups. mIF image **(E)** for CD34 (red) and H3K27me3 (green) with overview (scale bar 100 µm) and magnified inlet (scale bar 50 µm). Quantification of H3K27me3-positive hematopoietic progenitors **(F)** showed a significant increase of H3K27me3 expression in hematopoietic progenitors in patients with advanced GATA2 deficiency (** $p < .01$) compared to $GATA2^{WT}$ patients (* $p < .05$). This image was originally featured in the study authored by Schreiber and colleagues (Schreiber et al 2023), published in *Cancers* and has been included here with the permission of the copyright holder.

The role of *EZH2* in epigenetic gene transcription repression and catalysis of histone H3 trimethylation at lysine 27 (H3K27me3) led us to investigate the presence of this gene silencing mark in our cohort, focusing on differences between $GATA2^{mut}$ and $GATA2^{WT}$ patients (Figure 9). Utilizing a semiquantitative scoring system for IHC stainings of H3K27me3 (see Appendix C, Table C 2), we observed predominantly negative to weakly positive immunoreactive scores in GATA2-RCC and MDS-EB patients (50% of GATA2-RCC negative to weakly positive, 44.45% of MDS-EB), while RCC patients demonstrated moderately positive scores (43.75% of RCC moderately positive). Contrasting to these results, the majority of GATA2-EB patients displayed strong H3K27me3 positivity (66.66% of GATA2-EB strongly positive).

To correlate the increased presence of *EZH2*-positive progenitors in GATA2-EB patients with the epigenetic function of *EZH2*, we conducted mIF, targeting CD34 and H3K27me3 (panel C, for details refer to Appendix C, Table C 1). Aligning with the previous findings, GATA2-EB patients exhibited a higher proportion of hematopoietic progenitors expressing H3K27me3 contrasting to their GATA2-RCC counterparts (mean ± SD in GATA2-EB 0.1512 ± 0.05944 versus 0.05063 ± 0.01921 in GATA2-RCC; $p < .01$; Figure 9). MDS-EB patients also showed an increase in H3K27me3-postive hematopoietic progenitors compared to RCC patients; however, the effect was less significant than in $GATA2^{mut}$ patients (mean ± SD in MDS-EB 0.07221 ± 0.04964 versus 0.03315 ± 0.02572 in RCC; $p < .05$).

For a detailed karyotypic examination of *RUNX1*- and *EZH2*-positive hematopoietic progenitors, along with the expression of H3K27me3 in CD34-positive cells, please refer to Appendix D, Figure D 6. In congruence with earlier findings on the implications of monosomy 7, our observations in this context similarly revealed no noteworthy variations in expression levels associated with karyotypic differences. Nonetheless, among GATA2-RCC patients with monosomy 7, subtle disparities were

found in progenitors expressing *RUNX1* and *EZH2* compared to those with alternate karyotypes. Additionally, in *RUNX1*-positive progenitors, MDS-EB patients exhibited slightly increased expression when affected by karyotypes other than monosomy 7.

3.6 Differential Expression of BCL2 in Distinct Cell Populations within the Bone Marrow

In light of the finding that *BCL2* emerged as a target of interest in the transcriptome analysis, exhibiting upregulation with disease progression in GATA2 deficiency (as depicted in Figure 4 and Figure 5), we undertook a comprehensive characterization of this antiapoptotic protein. For this purpose, we employed mIF to profile critical cell types within the bone marrow and assess the extent to which they express BCL2.

In panel D, we assessed BCL2 expression in cytotoxic T lymphocytes (CD8 subunit alpha, CD8). Panel E encompassed eosinophilic granulocytes (EPX), erythrocytes (transferrin receptor, CD71), and monocytes (CD14), while panel F was utilized for mIF profiling of myeloid cells (MPO), hematopoietic progenitors (CD34), T lymphocytes (CD3), and mast cells (MCT) alongside BCL2. Further details regarding panel D – F can be found in Appendix C, Table C 1.

Table 12: Mean proportion of BCL2-positive cells within cells expressing CD8, CD71, MPO, CD3, EPX, CD34, CD14, or MCT.

		RCC	MDS-EB	GATA2-RCC	GATA2-EB
Mean proportion of BCL2-positive cells within cells expressing	**CD8**	0.8009	0.4569	0.7013	0.5629
	CD71	0.2039	0.2633	0.2536	0.1461
	MPO	0.1096	0.1525	0.1696	0.2105
	CD3	0.0460	0.0617	0.1579	0.0372
	EPX	0.0175	0.0655	0.0285	0.0358
	CD34	0.0212	0.0504	0.0396	0.1186
	CD14	0.0219	0.0360	0.0367	0.0238
	MCT	0.0082	0.0052	0.0130	0.0017

The most prominent expression of BCL2 was observed in cytotoxic T lymphocytes (Table 12). Interestingly, the proportion of BCL2-expressing CD8-positive T cells declined with disease progression in GATA2^{mut} and GATA2^{WT} patients (mean ± SD in RCC 0.8009 ± 0.1925 versus 0.4569 ± 0.3532 in MDS-EB; $p < .05$; 0.7013 ± 0.2391 in GATA2-RCC versus 0.5629 ± 0.08060 in GATA2-EB; Figure 10). Notably, the total levels of CD8-positive cells within the bone marrow remained constant across all four patient groups, suggesting that the changes in BCL2 expression are not solely attributable to varying expression levels of cytotoxic T lymphocytes.

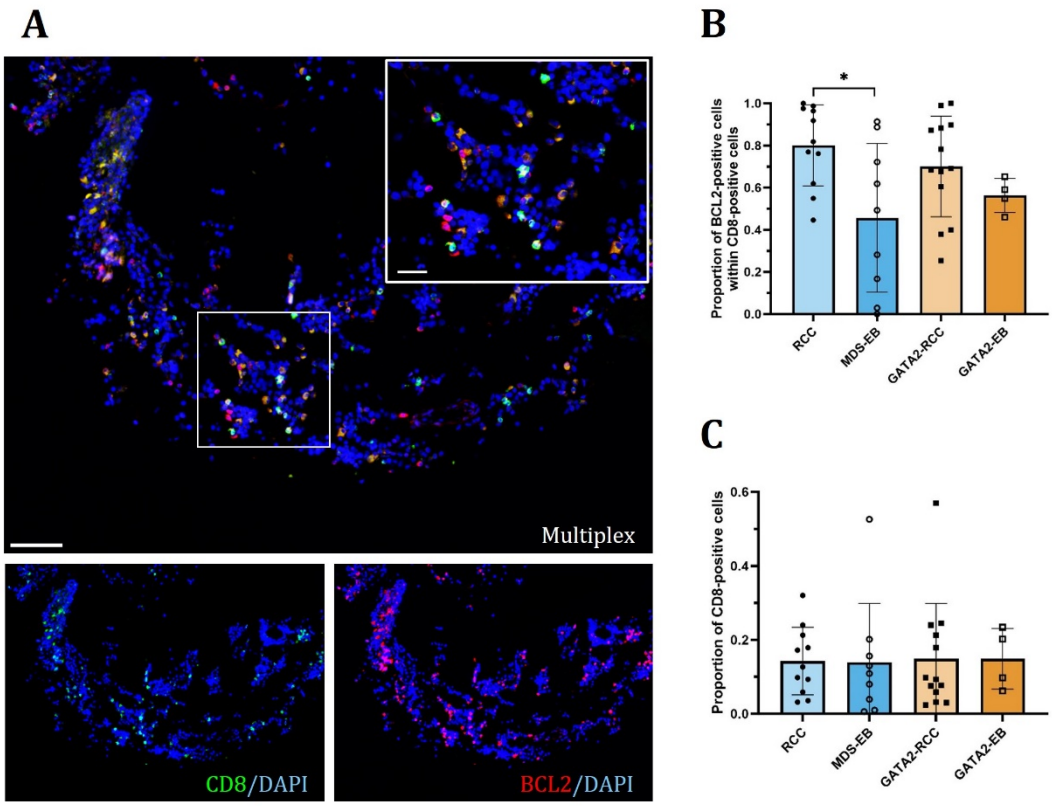

Figure 10: Elevated expression of BCL2 in CD8-positive T cells. mIF image **(A)** for cytotoxic T cells (CD8, green) and antiapoptotic protein BCL2 (red), DAPI staining in blue. The scale bars correspond to 100 µm for the overview and 50 µm for the magnified inlet. Quantification of BCL2 expression in CD8-positive cells **(B)** exhibited increased expression in early disease stages of GATA2^{mut} and GATA2^{WT} patients, and a decline with disease progression to GATA2-EB and MDS-EB (* $p < .05$). The expression levels of CD8-positive cells **(C)** did not vary, regardless of *GATA2* mutational status or disease progression.

Erythrocytes ranked second, with up to a quarter of CD71-positive cells expressing BCL2 (Table 12; Figure 11). The myeloid cell population emerged in third place, displaying upregulated BCL2 expression in patients with MDS-EB and GATA2-EB. This

correlated with an increased proportion of MPO-positive cells co-expressing BCL2 (Schreiber et al., 2023), indicating a survival advantage for the myeloid cell population during disease progression (mean ± SD in RCC 0.002466 ± 0.006717 versus 0.009667 ± 0.01899 in MDS-EB; $p < .05$; in GATA2-RCC 0.004448 ± 0.006316 versus 0.02623 ± 0.03047 in GATA2-EB; $p < .01$).

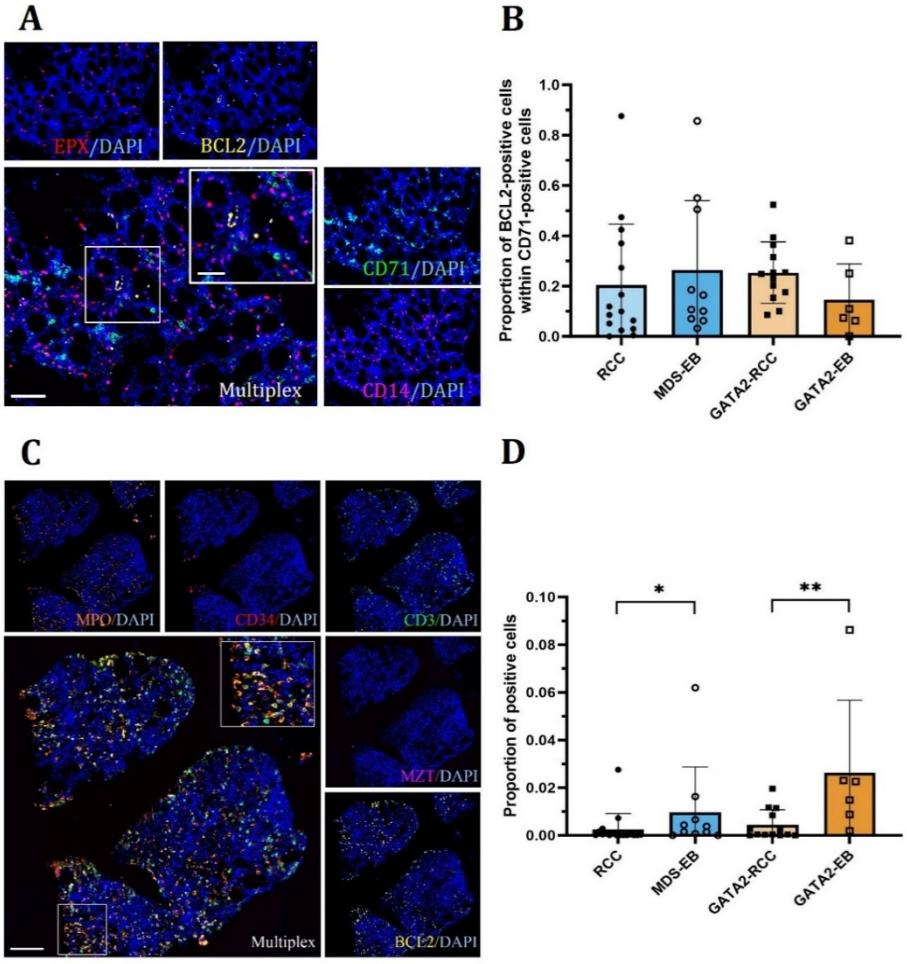

Figure 11: Profiling of BCL2 expression in different cell types in the bone marrow. mIF image **(A)** for eosinophilic granulocytes (EPX, red), erythrocytes (CD71, green), and monocytes (CD14, magenta) together with BCL2 (yellow). DAPI staining in blue, scale bars 100 µm (overview) and 50 µm (magnified inlet). Quantification of BCL2-expressing CD71-positive cells **(B)** demonstrated comparable expression levels in all four patient groups. mIF image **(C)** for myeloid cells (MPO, orange), hematopoietic progenitors (CD34, red), T cells (CD3, green), and mast cells (MZT, magenta), together with BCL2 (yellow). The scale bar corresponds to 100 µm. The expression of MPO-positive cells co-expressing BCL2 **(D)** was upregulated in GATA2-EB patients (** $p < .01$), and to a slighter extent with disease progression in GATA2^{WT} patients (* $p < .05$). Images (C) and (D) were originally featured in the study authored by Schreiber and colleagues (Schreiber et al. 2023), published in *Cancers* and have been included here with the permission of the copyright holder.

The proportion of BCL2-expressing CD3-positive cells showed minimal variation between RCC and MDS-EB, while patients with GATA2 deficiency exhibited a marked decrease in BCL2-positive T lymphocytes with disease progression (Table 12). Notably, the expression of BCL2 in all other cell types was found to be negligible.

3.7 Deciphering Dysregulated BCL2 Family Protein Expression Patterns in GATA2-EB Patients through a Unified Metric

In addition to exploring the role of BCL2 in disease progression in GATA2 deficiency, we proceeded to investigate the expression of additional BCL2 family members, MCL1 apoptosis regulator, BCL2 family member (MCL1) and BCL2 like 1 (Bcl-XL), to gain insights into their potential implications in the survival dynamics of $GATA2^{mut}$ patients (see Appendix C, Table C 1 for panel details). This chapter is a modified version of the study authored by Schreiber and colleagues (Schreiber et al., 2023), published in *Cancers* and has been reproduced here with the permission of the copyright holder.

In congruence with existing literature highlighting the importance of MCL1 and Bcl-XL in addition to BCL2 in orchestrating cellular survival (Adams & Cory, 2018; Huang et al., 2019; Letai et al., 2002), our analysis revealed contrasting trends in their expression levels in GATA2-EB patients (Figure 12). Specifically, both MCL1 and Bcl-XL exhibited reduced levels in GATA2-EB patients, while the RCC and MDS-EB groups displayed relatively comparable expression levels of these BCL2 family members.

To integrate a unifying metric for protein expression of BCL2, MCL1, and Bcl-XL, we introduced the "Mediators of Apoptosis Combinatorial Score" (Waclawiczek et al., 2023), alias MAC score, using two distinct calculation approaches and adapted the flow cytometry-based methodology to suit our mIF data.

In the first calculation approach, we considered the overall count of positively stained cells for each of the three proteins to present a simple and practical analysis plan (Figure 12). The resulting MAC score, reflecting the ratio of BCL2-positive cells to the sum of MCL1-positive and Bcl-XL-positive cells, was significantly higher in GATA2-EB patients compared to the GATA2-RCC group (mean ± SD GATA2-EB 1.487

± 1.184 versus 0.4425 ± 0.3659 in GATA2-RCC; $p < .01$). For patients without GATA2 deficiency, the MAC score did not exhibit substantial variation between RCC and MDS-EB (mean ± SD RCC 0.7621 ± 0.4522; MDS-EB 0.8686 ± 0.6336).

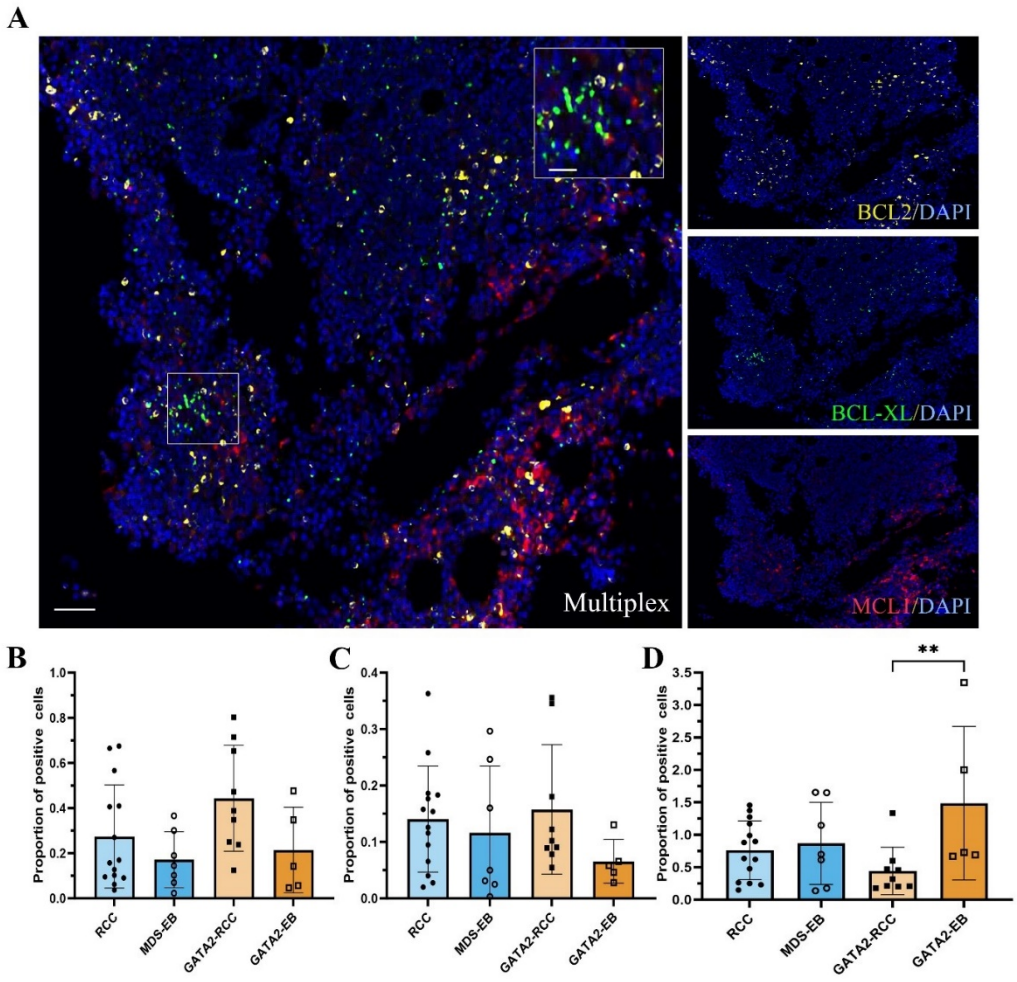

Figure 12: Elevated Mediators of Apoptosis Combinatorial score (MAC score) in GATA2-EB patients. mIF image **(A)** for the BCL2 family members BCL2 (yellow), Bcl-XL (green), and MCL1 (red) with scale bars corresponding to 100 µm for the overview and 50 µm for the magnified inlet. Quantification of MCL1 **(B)** and Bcl-XL **(C)** demonstrated reduced expression in GATA2-EB patients and relatively uniform expression in RCC and MDS-EB patients. Significantly upregulated MAC scores **(D)** were found in GATA2-EB patients (** $p < .01$) compared to GATA2-RCC and GATA2^{WT} patients.

The MAC score obtained from the second calculation approach exclusively focused on single positive cell phenotypes to resemble distinct subpopulations. Specifically, it represented the ratio of BCL2-positive, MCL1-negative, and Bcl-XL-negative cells to the sum of MCL1-positive, BCL2-negative, and Bcl-XL-negative cells and Bcl-XL-

positive, BCL2-negative, and MCL1-negative cells. Once more, GATA2-EB patients showed a significantly elevated MAC score compared to the other three patient groups (mean ± SD GATA2-EB 14.42 ± 29.42; GATA2-RCC 0.3568 ± 0.68586; $p < .01$; MDS-EB 3.071 ± 4.601; RCC 1.114 ± 1.106; data not shown).

3.8 Investigation of the Pyroptosis Pathway Exhibits Upregulated NLRP3 and Cleaved CASP1, but Inactive GSDMD in Advanced GATA2 Deficiency

In view of our observations delineating an elevated expression of BCL2, indicative of an heightened antiapoptotic response in advanced GATA2 deficiency, our attention was extended towards the investigation of pyroptosis, the inflammatory form of cell death, and its potential involvement in disease progression among pediatric MDS patients.

To explore this hypothesis, we employed mIF to quantify the expression of key players in the pyroptosis pathway, including cleaved caspase 1 (CASP1), NLR family pyrin domain containing 3 (NLRP3), and S100 calcium binding protein A9 (S100A9). However, due to technical limitations in detecting cleaved CASP1 with mIF, we opted to utilize IHC for this particular analysis (refer to Appendix C, Table C 1 for details about panel H and to Table C 2 for details about IHC marker).

The additional attempt to measure the area of fat vacuoles in bone marrow tissue using perilipin 1 (PLIN1) in panel H did not yield substantial variations between $GATA2^{mut}$ and $GATA2^{WT}$, as the fat vacuole area remained relatively consistent among all patients in the cohort (Figure 13).

Regarding inflammatory cell death, our investigation revealed slightly upregulated expression of S100A9, a critical alarmin initiating the pyroptosis signaling cascade, in GATA2-EB patients compared to GATA2-RCC (mean ± SD 0.3415 ± 0.2537 in GATA2-EB versus 0.1884 ± 0.1175 in GATA2-RCC; Figure 14). Patients with $GATA2^{WT}$ exhibited comparable S100A9 levels.

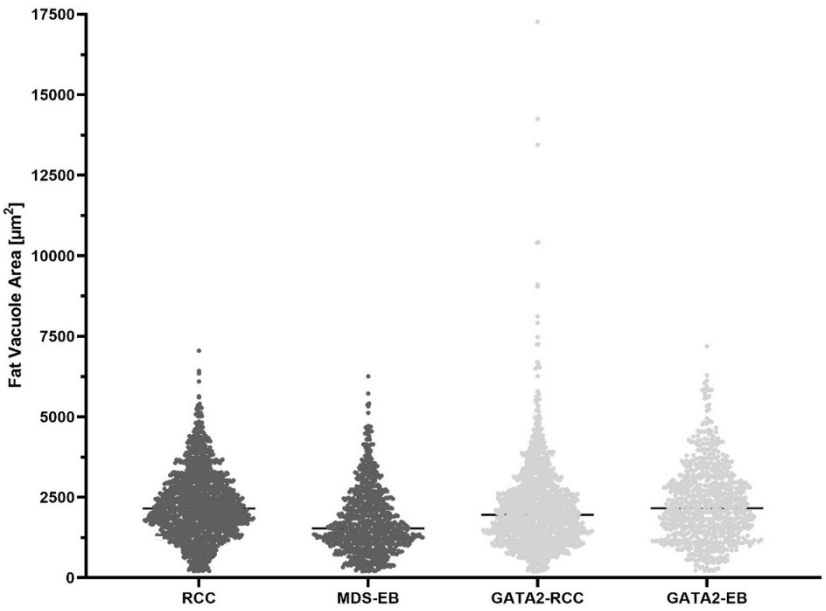

Figure 13: Visualization of the fat vacuole area in bone marrow samples. PLIN1 staining was used to measure the fat vacuole area [µm²] in the cohort. However, no substantial variations in the fat vacuole area were observed between patients, regardless of *GATA2* mutational status or disease progression.

In our investigation of downstream targets in pyroptosis, our focus turned to the formation of the inflammasome within the cell, which is represented by the NLRP3 protein (Figure 14). Notably, we observed a significant upregulation of NLRP3 with disease progression in GATA2^{mut} patients, while those with RCC and MDS-EB displayed a more stable and weaker NLRP3 expression (mean ± SD GATA2-EB 0.6710 ± 0.2442 versus 0.1373 ± 0.09815 in GATA2-RCC; $p < .0001$; RCC 0.2386 ± 0.1187; MDS-EB 0.2771 ± 0.1794).

Following inflammasome formation, CASP1 cleavage is initiated. Consistent with the upregulated NLRP3, we also found increased levels of cleaved CASP1 in GATA2-EB patients, whereas the expression of cleaved CASP1 remained below 25% in all other patient groups (mean ± SD GATA2-EB 0.5909 ± 0.09780 versus 0.2088 ± 0.1529 in GATA2-RCC; $p < .0001$; RCC 0.2440 ± 0.1463; MDS-EB 0.1769 ± 0.06360; Figure 14).

Upon analysis of S100A9, NLRP3, and CASP1 expression patterns in relation to patient karyotypes, no significant distinctions became evident concerning these pivotal components of pyroptosis (see Appendix D, Figure D 7).

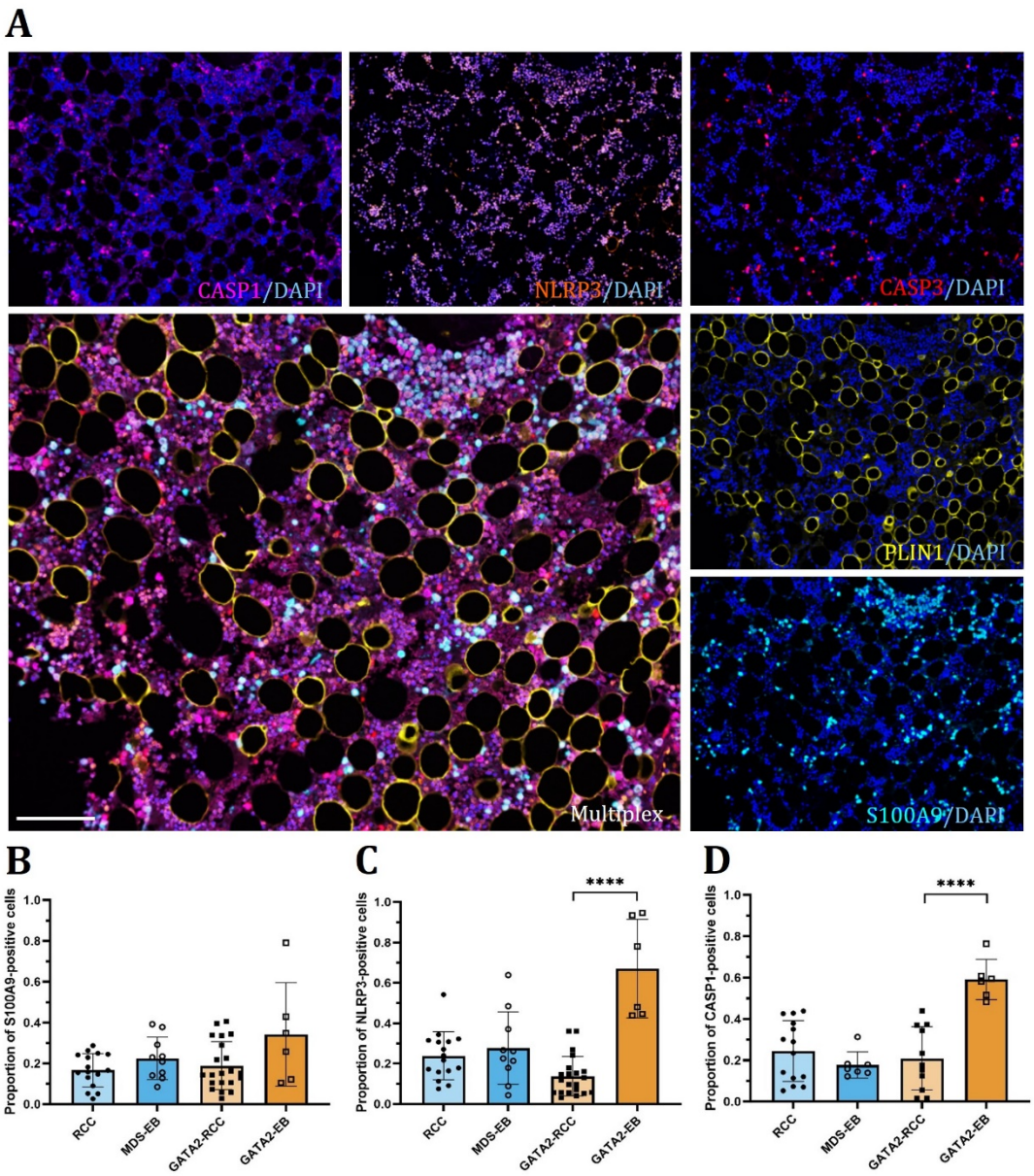

Figure 14: Enhanced expression of NLRP3 and CASP1 with disease progression in GATA2 deficiency. mIF image **(A)** for CASP1 (magenta), NLRP3 (orange), CASP3 (red), PLIN1 (yellow), and S100A9 (cyan), DAPI staining in blue. The scale bar corresponds to 100 µm. S100A9 expression **(B)** was slightly increased in GATA2-EB patients, whereas GATA2^{WT} patients demonstrated uniform expression levels. Quantification of NLRP3 **(C)** and CASP1 **(D)** revealed substantial upregulation with disease progression in GATA2^{mut} patients (**** $p <$ .0001). GATA2-EB patients showed the most prominent NLRP3 and CASP1 expression levels compared to all other disease groups.

It is worth mentioning that although CASP1 may be the executioner caspase in pyroptosis, not every cleavage of CASP1 necessarily leads to cell death (Sallman et al., 2016). Hence, we extended our investigation to examine the expression of gasder-

min D (GSDMD). This protein undergoes cleavage and translocation to the cell membrane following CASP1 cleavage, culminating in pore formation in the cell membrane and, consequently, inducing cell lysis concurrent with cell death (Sborgi et al., 2016; Shi et al., 2015). Intriguingly, utilizing the semiquantitative immunoreactive scoring system for IHC stainings of cleaved GSDMD, our cohort almost exclusively exhibited negative immunoreactive scores for cleaved GSDMD, irrespective of the *GATA2* mutational status and disease progression (Figure 15). Moreover, visual histomorphological evaluation revealed that cells appeared viable, and no cell lysis was apparent.

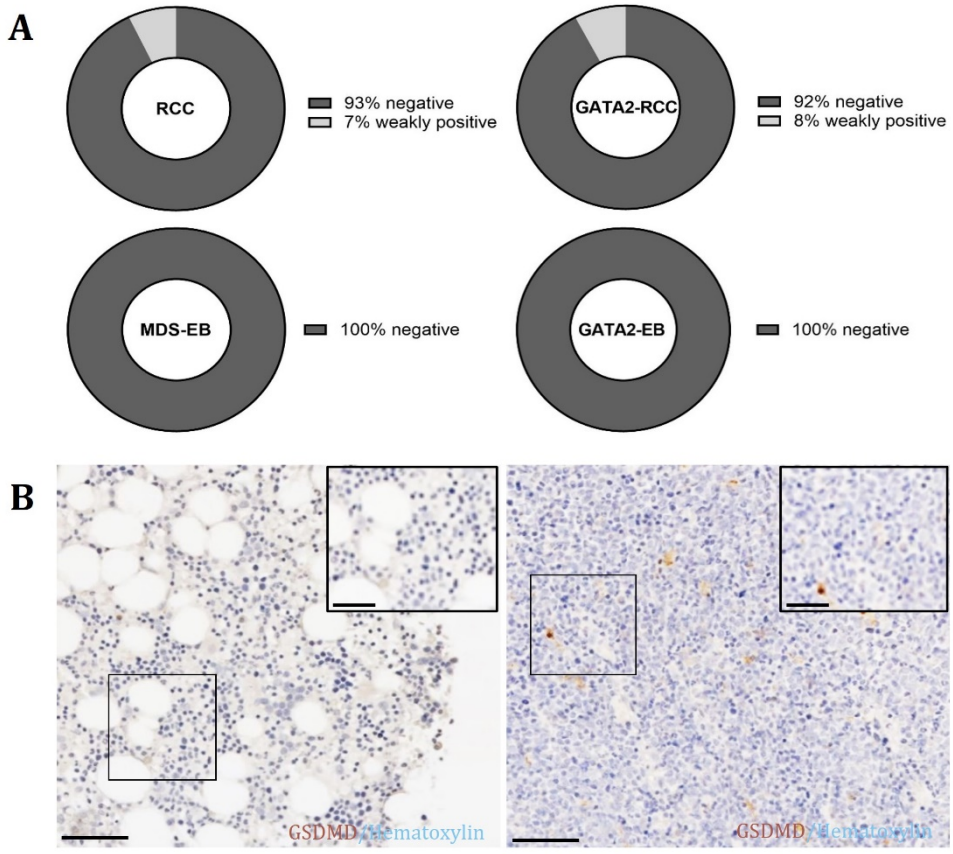

Figure 15: No discernible GSDMD positivity in GATA2^{mut} and GATA2^{WT} patients in the cohort. Visualization of the semiquantitative immunoreactive scoring system **(A)** for immunohistochemical stainings of GSDMD. GATA2-RCC and RCC patients demonstrated a small portion of weakly positive immunoreactive scores, whereas GATA2-EB and MDS-EB patients presented exclusively negative for GSDMD. Overview of immunohistochemistry **(B)** for GSDMD (brown) with representative images of a negative immunoreactive score (on the left) and weak positivity (on the right), hematoxylin counterstaining in blue. The scale bars correspond to 100 µm for the overview and 50 µm for the magnified inlet.

In addition to the execution of pyroptosis, CASP1 cleavage can lead to the activation of interleukin 1 beta (IL1B) and interleukin 18 (IL18), both known as pro-inflammatory cytokines that play pivotal roles in promoting inflammation and immune responses in humans (Dinarello, 2009; Sallman et al., 2016). Analysing the list of 770 genes included in the gene expression profiling analysis, we observed differential expression of both IL1B and IL18 in our cohort. Comparing GATA2-RCC to GATA2-EB, we found a decrease in $\log_2$ fold change of 1.59 for IL1B and 0.308 for IL18 in GATA2-RCC. On the other hand, comparing GATA2-EB to MDS-EB, both cytokines exhibited increased expression in GATA2-EB, with $\log_2$ fold changes of 2.09 for IL1B and 0.274 for IL18, respectively (data not shown). These observations suggest a potential upregulation of both cytokines with disease progression in GATA2 deficiency.

3.9 Examination of T Cell Phenotypes Reveals Altered Antiapoptotic Properties in TIM-3-Expressing Cells in GATA2 Deficiency

As we observed the most prominent expression of BCL2 in cytotoxic T lymphocytes and noted a marked decline accompanying disease progression in both $GATA2^{mut}$ and $GATA2^{WT}$ patients (see Figure 10), we proceeded to delve deeper into characterizing distinct T cell phenotypes. To achieve this, we compiled a mIF panel, encompassing discerning markers for exhausted T cells (programmed cell death 1, PD-1), regulatory T cells (forkhead box P3, FOXP3), and an additional robust indicator for T cell exhaustion (hepatitis A virus cellular receptor-2, TIM-3), together with BCL2, to gain insights into T cell dysregulation (refer to Appendix C, Table C 1 for a detailed description of panel I).

Quantifying the total amounts of the three markers, the expression levels of TIM-3, PD-1, and FOXP3 were found to persist below 10% for all four patient groups (Figure 16). However, the expression of TIM-3 showed a significant increase with disease progression in GATA2 deficiency, while PD-1 and FOXP3 levels remained relatively unchanged (mean ± SD of TIM-3-positive cells 0.08219 ± 0.04109 in GATA2-EB; 0.008797 ± 0.006674 in GATA2-RCC; $p < .05$).

The proportion of BCL2-expressing TIM-3-positive cells was found to be roughly 20% in GATA2-RCC, but significantly upregulated to 93% with disease progression

in GATA2-EB patients (mean ± SD in GATA2-EB 0.9265 ± 0.03262 versus 0.2013 ± 0.1766 in GATA2-RCC; $p < .001$; Figure 17). Similarly, patients without GATA2 deficiency showed increased levels of TIM-3-positive cells with antiapoptotic properties with disease progression, albeit to a lesser extent compared to GATA2-EB patients (mean ± SD in MDS-EB 0.2747 ± 0.3155 versus 0.1080 ± 0.1580 in RCC).

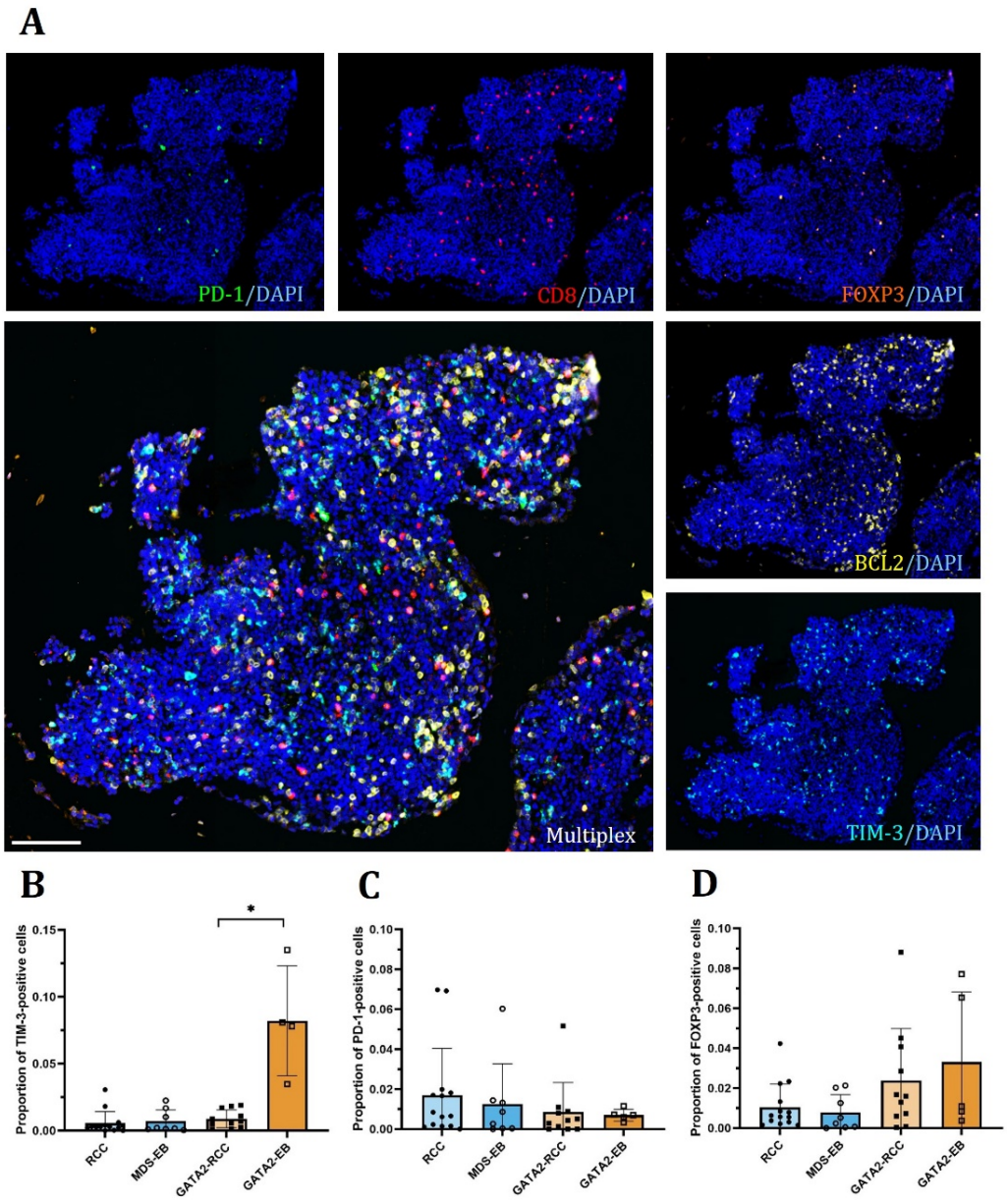

Figure 16: Elevated TIM-3 expression in GATA2-EB patients. mIF image **(A)** for PD-1 (green), CD8 (red), FOXP3 (orange), and TIM-3 (cyan) together with BCL2 (yellow). DAPI staining in blue, scale 100 µm. TIM-3 expression **(B)** was enhanced with disease progression in GATA2 deficiency (* $p < .05$), whereas PD-1 **(C)** and FOXP3 **(D)** expression levels did not change significantly across disease groups.

Analysing BCL2 expression in PD-1- and FOXP3-positive cells, we also observed statistically significant upregulation correlating with disease progression in GATA2 deficiency (mean ± SD of BCL2-positive cells within cells expressing PD-1 0.5932 ± 0.1539 in GATA2-EB versus 0.3060 ± 0.2376 in GATA2-RCC; $p < .05$; of BCL2-positive cells within cells expressing FOXP3 0.8618 ± 0.06191 in GATA2-EB versus 0.5934 ± 0.2315 in GATA2-RCC; $p < .01$; Figure 17). Notably, the increase in BCL2-expressing TIM-3-positive cells was found to be most pronounced. Antiapoptotic properties in PD-1-positive cells did not exhibit substantial changes in RCC and MDS-EB patients, while for FOXP3-positive cells, BCL2 expression decreased slightly with disease progression in GATA2^{WT} patients.

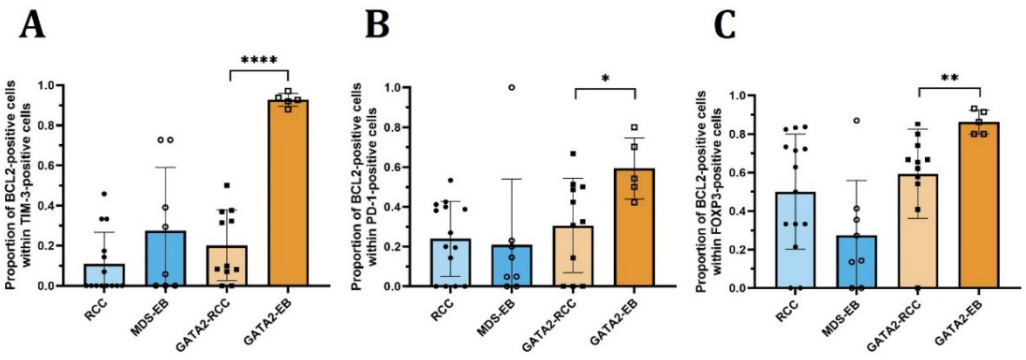

Figure 17: Enhanced BCL2 expression in TIM-3-, PD-1-, and FOXP3-positive cells with disease progression in GATA2 deficiency. The proportion of BCL2 expression in TIM-3-positive cells **(A)** was substantially elevated in GATA2-EB patients (**** $p < .0001$). Additionally, the levels of BCL2-expressing PD-1-positive **(B)** and FOXP3-positive **(C)** cells increased significantly with disease progression in GATA2^{mut} patients, albeit to a lesser extent compared to TIM-3 (* $p < .05$; ** $p < .01$). The BCL2 expression of the distinct cells did not change substantially in patients with GATA2^{WT}.

3.10 Cell Type Profiling Reveals High MPO Levels in TIM-3-Expressing Cells

As we observed notable alterations in the expression of TIM-3-positive and BCL2-expressing TIM-3-positive cells correlating with disease progression in GATA2 deficiency, our attention shifted towards a deeper exploration of this protein. Consequently, our subsequent investigations were aimed at identifying the specific cell types within the bone marrow exhibiting heightened TIM-3 expression.

Table 13: Mean proportion of TIM-3-positive cells within cells expressing MPO, CD14, CD3, CD163 or MCT.

		RCC	MDS-EB	GATA2-RCC	GATA2-EB
Mean proportion of TIM-3-positive cells within cells expressing	**MPO**	0.3924	0.3539	0.5692	0.3255
	CD14	0.3226	0.3625	0.4825	0.2669
	CD3	0.0143	0.0279	0.0359	0.0191
	CD163	0.0069	0.0188	0.0157	0.0162
	MCT	0.0060	0.0241	0.0165	0.0066

To achieve this, we assembled two mIF panels (refer to Appendix C, Table C 1 for details about panel J and K). The first panel elucidated the presence of TIM-3 in T lymphocytes (CD3), macrophages (CD163 molecule, CD163), and mast cells (MCT). The second panel, on the other hand, focused on myeloid cells (MPO) and monocytes (CD14).

We found a prevalence of TIM-3 expression within myeloid cells, reaching a zenith of nearly 57% among patients with GATA2-RCC (Table 13). Notably, CD14-positive cells also exhibited a noteworthy expression of TIM-3, whereas all other profiled cell types displayed markedly diminished levels of TIM-3 expression.

In view of the relatively limited population of TIM-3-positive cells within the bone marrow (refer to Figure 16), we turned our attention to the co-expression patterns of TIM-3 positive cells (Figure 18). Here, MPO emerged as the most prominent player, with 90-98% of TIM-3 positive cells co-expressing MPO across all four patients groups (mean ± SD of MPO-positive cells within TIM-3-positive cells 0.9422 ± 0.05183 in RCC; 0.9539 ± 0.03297 in MDS-EB; 0.8986 ± 0.08891 in GATA2-RCC; 0.9791 ± 0.02054 in GATA2-EB; $p < 0.5$).

In contrast, the expression of CD14 in TIM-3 positive cells was notably less pronounced, with the highest levels observed in MDS-EB patients (mean ± SD of CD14-positive cells within TIM-3-positive cells 0.2238 ± 0.2530 in MDS-EB; 0.1799 ± 0.1540 in RCC; 0.1310 ± 0.1133 in GATA2-EB; 0.1997 ± 0.1671 in GATA2-RCC; Figure 18).

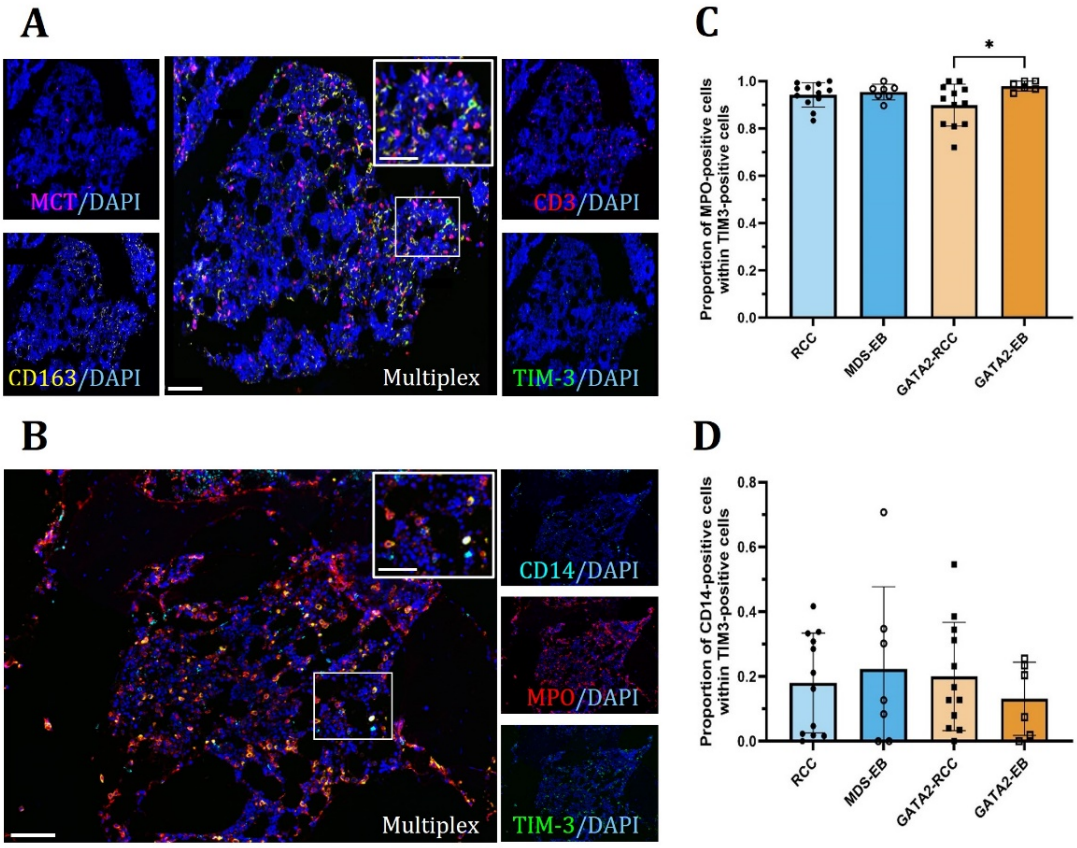

Figure 18: Profiling of co-expression patterns of TIM-3-positive cells in the bone marrow. mIF image **(A)** for mast cells (MCT, magenta), macrophages (CD163, yellow), and T lymphocytes (CD3, red), as well as **(B)** for monocytes (CD14, cyan), and myeloid cells (MPO, red), together with TIM-3 (green). DAPI staining in blue, scale bars corresponding to 100 µm (overview) and 50 µm (magnified inlet). Quantification of MPO-positive cells within TIM-3-positive cells **(C)** demonstrated that TIM-3-positive cells showed a strong co-expression of MPO with slight upregulation in GATA2-EB patients (* $p < .05$). CD14 expression in TIM-3-positive cells **(D)** did not change significantly across all patient groups.

3.11 CCL18 is Strongly Expressed in MPO-positive Cells in Pediatric MDS Bone Marrow Samples

In the transcriptome analysis, the identification of *CCL18*, alongside *BCL2*, emerged as a notable point of interest. CCL18, a chemokine recognized for its role in immune system regulation and inflammatory processes within the human body, has been associated with aberrant levels in various inflammatory conditions, including rheumatoid arthritis and pulmonary fibrosis (Cardoso et al., 2021; Schutyser et al., 2005).

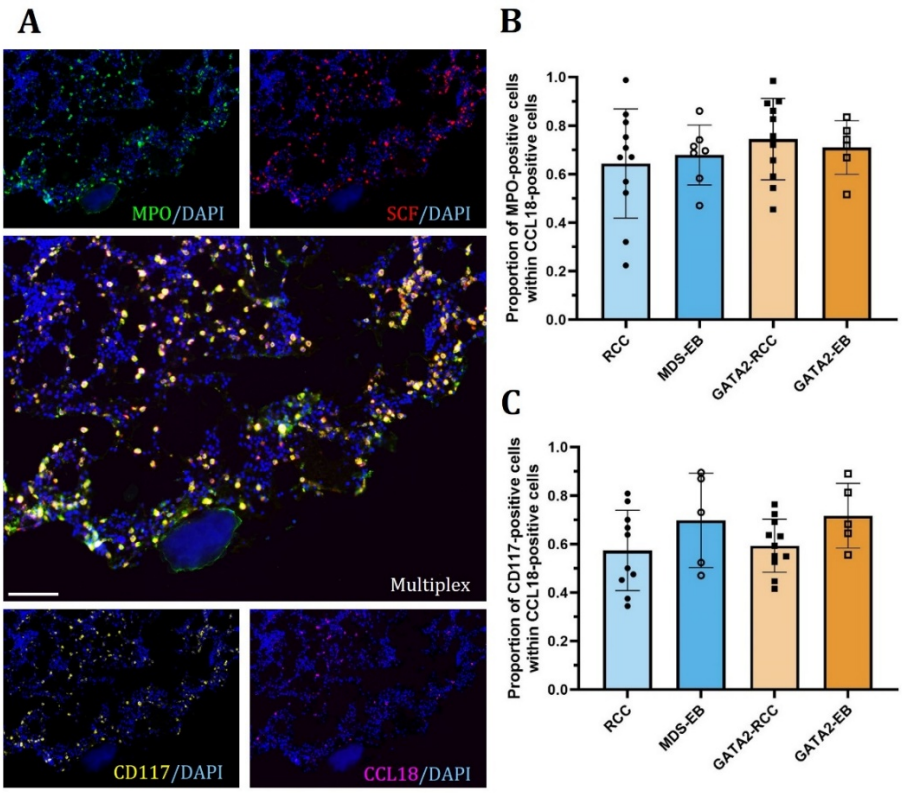

Figure 19: Profiling of co-expression patterns of CCL18-positive cells in the bone marrow. mIF image **(A)** for MPO (green), SCF (red), and CD117 (yellow) together with CCL18 (magenta). DAPI staining in blue, scale bar 100 µm. Quantification of CCL18-positive cells revealed strong MPO expression in CCL18-positive cells **(B)** and slightly less expression of CD117 in CCL18-positive cells **(C)**. The expression levels did not change significantly across patient groups, regardless of *GATA2* mutational status or disease progression.

With an interest in a detailed exploration of CCL18 expression patterns in the bone marrow, we employed a mIF panel to assess its co-expression with MPO, stem cell factor (SCF), and KIT proto-oncogene, receptor tyrosine kinase (CD117), and a second panel to additionally evaluate co-expression with CD34 (refer to Appendix C, Table C 1 for a detailed description of panel L and panel M).

Notably, CCL18-positive cells demonstrated robust co-expression of MPO, showing a slight increase in GATA2^{mut} patients (mean ± SD of MPO-positive cells within CCL18-positive cells 0.7443 ± 0.1674 in GATA2-RCC; 0.7097 ± 0.1102 in GATA2-EB), compared to GATA2^{WT} (mean ± SD of MPO-positive cells within CCL18-positive cells 0.6439 ± 0.2252 in RCC; 0.6788 ± 0.1234 in MDS-EB; Figure 19). Furthermore, CD117 exhibited pronounced expression in CCL18-positive cells, with increasing numbers correlating with disease progression in both GATA2^{mut} and GATA2^{WT} cohorts (mean ± SD of CD117-positive cells within CCL18-positive cells 0.5736 ±

01658 in RCC; 0.6977 ± 0.1944 in MDS-EB; 0.5934 ± 0.1096 in GATA2-RCC; 0.7170 ± 0.1336 in GATA2-EB).

A lower degree of co-expression was observed between CCL18 and CD34, with values approximating 50% of CD34-positive cells within CCL18-positive cells or lower (mean ± SD of CD34-positive cells within CCL18-positive cells 0.4971 ± 0.1298 in RCC; 0.3368 ± 0.1753 in MDS-EB; 0.5020 ± 0.1791 in GATA2-RCC; 0.5283 ± 0.1586 in GATA2-EB; data not shown).

3.12 Implications of CCL18 Expression in Hematologic Cell Lines upon PMA Stimulation

In order to find an appropriate model for investigating the inflammatory roles of CCL18 within the context of GATA2 deficiency, we directed our focus to two hematologic cell lines, namely KG-1 and K-562, both known to express GATA2. KG-1 was further identified in the literature as constitutively expressing CCL18 (St Louis et al., 1999), while K-562 is reported to exhibit CCL18 expression upon PMA stimulation (Hieshima et al., 1997).

Subsequent to subjecting both cell lines to PMA stimulation for durations of 48 h and 72 h, encompassing concentrations ranging from 1 nM to 10 µM, we proceeded with protein isolation and subsequent Western blot analysis, conducted on 20% acrylamide gels. Notably, it was observed that a PMA concentration of 10 µM manifested as cytotoxic, with an absence of protein yield in both KG-1 and K-562 cell lines (data not shown).

For validation purposes, recombinant human CCL18 protein at a concentration of 1 µg was incorporated as positive control, and NFKB inhibitor alpha (IκBα) was employed to visually confirm the efficacy of PMA stimulation (Brown et al., 1995; Guerrini et al., 1996). Nevertheless, we could not observe a discernible CCL18 band of the expected size of 8 kDa under any PMA concentration or duration of stimulation tested (refer to Appendix E, Figure E). Additionally, the intensity of the IκBα control band did not exhibit a decrease in K-562 cells, implying the ineffectiveness of the PMA stimulation in our experimental conditions.

4. Discussion

The intricate mechanisms and underlying drivers responsible for malignant transformation in pediatric GATA2 deficiency remain inadequately understood. This underscores the imperative to deepen our comprehension of this heterogeneous, multisystem disorder (Schreiber et al., 2023).

Addressing these gaps in knowledge, our study delves into the complexities of pediatric GATA2 deficiency. Through systematic investigation, this research aims to identify predictive markers for assessing individual risk of disease progression. The findings presented herein can play a pivotal role in refining diagnostic and therapeutic strategies for pediatric patients affected by GATA2 deficiency, ultimately contributing to the advancement of patient care.

4.1 A Contextual Overview of the Rarity of MDS in the Pediatric Population

In contrast to the adult population, pediatric MDS is a rare condition, with an estimated incidence of approximately 1.8 to 4 cases per million children (Hofmann, 2015). Our study primarily focused on children residing in Germany, where the population under the age of 18 is 14.25 million (as of December 31, 2022; https://de.statista.com), encompassing only 7.1 million individuals aged between 6 and 14 years. The instances of *GATA2* mutations in this population are significantly lower, pointing to an exceptionally small number of affected children.

While our sample includes 57 children, which might seem modest initially, it gains significance when compared to the estimated 25 to at most 57 pediatric MDS cases exclusive to Germany. This sample presents a substantial portion, offering valuable insights into the characteristics of pediatric MDS within the context of GATA2 deficiency.

Nevertheless, the sample size, particularly the six patients included in the GATA2-EB group, may impact statistical power. To mitigate this, we included 10 MDS-EB patients without GATA2 deficiency as a valuable comparison group for analysis. The

observed differences between the GATA2-EB group and MDS-EB patients across experiments emphasize the clear contrast between individuals with and without GATA2 deficiency. However, it is essential to acknowledge that the limited sample size could slightly influence the accurate estimation of the effect size, underscoring the necessity for further investigations with larger sample sizes (Schreiber et al., 2023).

4.2 The Mast Cell Population as Focal Point of Interest in Pediatric MDS

The clinical and histomorphological characteristics of GATA2 deficiency manifest considerable variations, encompassing cellularity, hematopoietic dysplasia, and cell differentiation. To conduct a comprehensive hematopathological assessment of the trilinear hematopoiesis, we employed mIF coupled with multispectral image analysis.

In line with prior research indicating reduced B cell counts in GATA2 deficiency (Dickinson et al., 2011; Nováková et al., 2016), GATA2^{mut} patients in our cohort exhibited markedly low expression of B lymphocytes. This not only replicates earlier findings but also affirms the precision of our mIF stainings, serving as internal validation.

Examining major cell types in the bone marrow, including myeloid cells, megakaryocytes, T lymphocytes, monocytes, dendritic cells, hematogonic cells, and eosinophilic granulocytes, we observed no discernible changes that could distinguish patients with GATA2 deficiency from GATA2^{WT}. Neither did differences in proliferating cell rates emerge between these groups.

Diving deeper into patients sharing the same diagnosis, we focused on potential variations based on karyotypes, specifically comparing monosomy 7, the most prevalent aberration observed in both our GATA2^{mut} cohort and previous studies (Wlodarski et al., 2016), against other karyotypes within the group. Interestingly, patients with monosomy 7 did not exhibit substantial differences in the expression levels of investigated cell types when juxtaposed against those with different chromosomal aberrations. Consequently, in our cohort, the karyotype, and specifically

the influence of monosomy 7, did not emerge as a decisive factor in assessing malignant transformation or disease progression. However, it is important to note that in GATA2-EB, monosomy 7 was the sole karyotype present, rendering comparisons challenging.

Shifting our focus from mIF and expression at protein level to gene expression profiling for investigating differential gene expression through mRNA detection, we uncovered an intriguing and novel aspect – higher abundance of mast cells in patients with GATA2 deficiency. This finding was reinforced at the protein level, with increased expression of MCT in patients with GATA2 deficiency compared to $GATA2^{WT}$.

Identifying mast cells as a cellular population with differential expression in patients with and without GATA2 mutations, we delved into further examination. A 2021 study provided initial evidence linking GATA2 to mast cells, describing GATA2 as lineage-determining factor and demonstrating its role in promoting chromatin accessibility to enhance robust gene transcription, thereby maintaining mast cell identity (Y. Li et al., 2021).

Beyond the commonly assessed marker MCT, mast cells have the potential to express chymase, a neutral protease implicated in inducing apoptosis in human coronary smooth muscle cells in culture (Leskinen et al., 2001). However, the debate surrounding the existence of mast cells expressing only chymase in neoplastic or physiological states remains controversial (Horny et al., 2003; L. Li & Krilis, 1997). Consequently, we proceeded to assess the expression of chymase and/or MCT together to gain a better understanding of the characteristics of bone marrow mast cells in pediatric MDS, aiming to determine whether these cells exhibit differences in expression patterns. Our attempt, utilizing IHC and mIF stainings, proved challenging (data not shown), prompting further investigations to enhance our understanding of this intriguing cell population in the context of pediatric MDS and GATA2 deficiency.

4.3 Dysregulated *GATA2* Transcriptional Network in GATA2 Deficiency and Restoration of *GATA2* mRNA with Disease Progression

To pursue a comprehensive exploration of the hematopoietic niche within the context of GATA2 deficiency, we employed RNA-*in situ* hybridization to examine the influence of GATA2 on its microenvironment and a subset of its target genes.

Previous research has demonstrated that germline mutations in the *GATA2* gene can lead to disrupted gene expression and haploinsufficiency (Hahn et al., 2011; Ostergaard et al., 2011; Wlodarski et al., 2016). Consistent with this understanding, we observed significantly reduced expression levels of *GATA2* mRNA in individuals diagnosed with GATA2-RCC. GATA2 plays a critical role in regulating the expression of its target genes *RUNX1*, *EZH2*, *IKZF1*, and *LYL1* (Katsumura et al., 2017). As anticipated, the decreased expression of *GATA2* in GATA2-RCC patients correlated with a parallel reduction in the levels of these four GATA2 target genes. This concordance underscores the perturbation of the *GATA2* transcriptional network in GATA2 deficiency (Schreiber et al., 2023).

Moreover, our investigation into disease progression revealed a novel and intriguing aspect. Contrary to the expected continued downregulation following germline mutations in *GATA2*, we observed a restoration in the expression levels of *GATA2*, accompanied by a simultaneous upregulation of the associated target genes. This resurgence was exclusively observed in patients with GATA2-EB, highlighting the differences between patients with and without *GATA2* mutations. This previously undocumented observation was initially reported in our 2023 publication in *Cancers* (Schreiber et al., 2023).

The restoration of *GATA2*-associated expression dynamics introduces a nuanced layer to our understanding of the disease trajectory. Our observations prompt a deeper exploration into the molecular mechanisms governing this unexpected reversal, potentially offering insights into compensatory mechanisms or alternative regulatory pathways activated during advanced disease stages in GATA2 deficiency.

4.4 Upregulation of *EZH2* Expression Associated with Increased Histone Trimethylation H3K27me3 in Advanced GATA2 Deficiency

To explore the potential consequences of the dysregulated *GATA2* transcriptional network for the hematopoietic stem cell pool, we employed combinatorial *in situ* hybridization to simultaneously assess the expression of *CD34* and *EZH2* in each cell.

In the context of adult MDS, the role of *EZH2* in promoting disease progression is well acknowledged (Zheng et al., 2021), yet this understanding is lacking in the pediatric population. Within our cohort of pediatric patients, we observed a significant upregulation of *EZH2* expression in hematopoietic progenitors with disease progression in GATA2 deficiency. In contrast, in GATA2^{WT} patients, the levels of *EZH2*-expressing hematopoietic progenitors remained unchanged, once again highlighting GATA2 deficiency as distinct disease entity.

Functioning as a histone methyltransferase, *EZH2* targets histone H3 at lysine 27 and catalyses its trimethylation H3K27me3, executing a fundamental role in orchestrating epigenetic silencing (Cao et al., 2002; Viré et al., 2006). The analysis of this gene silencing mark in our cohort revealed that patients with advanced GATA2 deficiency exhibited strong positivity for H3K27me3, distinguishing this group from GATA2-RCC or GATA2^{WT} patients, predominantly negative for this marker. Furthermore, an increase of H3K27me3 expression in hematopoietic progenitors was observed in GATA2-EB, linking elevated levels of *EZH2* to increased histone trimethylation H3K27me3 in advanced GATA2 deficiency (Schreiber et al., 2023).

Our findings regarding the crucial role of *EZH2* in histone trimethylation align with prior studies in adult AML/MDS and underscore the potential of *EZH2* as promising candidate for a prognostically relevant marker (Göllner et al., 2017; McGraw et al., 2019; Stomper et al., 2021). While extensive research has explored the influence of *EZH2* and epigenetics in general in adult MDS (Figueroa et al., 2009; Issa, 2013; Karoopongse et al., 2014; Stomper et al., 2021; Xu et al., 2011), evidence in children is limited (de Souza Fernandez et al., 2019). Consequently, our study contributes to the sparse literature, offering insights that can enhance our comprehension of the impact of epigenetic factors in the context of pediatric MDS (Schreiber et al., 2023).

4.5 Acquired Resistance to Apoptosis in Pediatric GATA2 Deficiency

BCL2 has emerged as a notable target in the transcriptome analysis, demonstrating a substantial upregulation with disease progression in GATA2 deficiency and significantly lower expression in GATA2^{WT} patients. To delve deeper into this intriguing finding, we extended our analysis to different cell types in the bone marrow, aiming to evaluate the extent of their expression of this antiapoptotic protein.

In the context of transformation from MDS to AML, one focus of our examination has been the myeloid cell population. Within this critical subset, we noted a significant increase in the expression of the antiapoptotic BCL2. Remarkably, this enhancement specifically occurred in the myeloid cells of pediatric patients with advanced GATA2 deficiency. This observation underscores the heightened significance of myeloid cells in the context of disease progression and highlights the emergence of acquired resistance to apoptotic cell death, offering insights into potential mechanisms on the path towards disease progression in pediatric GATA2 deficiency (Schreiber et al., 2023).

While the concept of acquired resistance to apoptosis following dysregulated apoptotic signaling is well established in adult high-risk MDS (Boudard et al., 2002; Jilg et al., 2016; Parker et al., 2000; Raza et al., 1995), there is limited understanding in pediatric MDS. Our findings contribute to this sparse literature by providing cues that the upregulation of antiapoptotic signaling via an increase in BCL2 might play a crucial role in disease progression in pediatric GATA2 deficiency. In addition to enhancing our comprehension of the pathogenic mechanisms in disease progression, this finding provides an essential connection between adult and pediatric patients (Schreiber et al., 2023). It urges further investigations into the context of apoptotic resistance in the pediatric population, unraveling more facets of the complex etiology of the disorder.

4.6 The MAC Score as Prognostic Tool in Pediatric GATA2 Deficiency: Implications for Venetoclax and Azacitidine Therapy

In addition to examining the involvement of BCL2 in the progression of GATA2 deficiency, we extended our investigation to include the expression of other

BCL2 family members, namely the antiapoptotic proteins MCL1 and Bcl-XL, recognized for their roles in promoting cell survival (Adams & Cory, 2018; Huang et al., 2019; Letai et al., 2002).

To consolidate the expression patterns of the three BCL2 family members, we employed the MAC score, initially introduced by Waclawiczek et al. (Waclawiczek et al., 2023). This flow cytometry-based metric combines the expression of BCL2, MCL1, and Bcl-XL and was originally designed to predict the response to venetoclax (VEN) and azacitidine (AZA) combination therapy in adult AML patients. The MAC score proved to be a valuable predictive marker in their cohort, prompting our interest in its utilization for pediatric MDS patients.

Application of the MAC score through mIF in our pediatric cohort revealed significantly increased scores with disease progression in GATA2 deficiency. Conversely, GATA2^{WT} patients exhibited unchanged MAC scores with disease progression, emphasizing the distinctions between patients with and without GATA2 mutations. Following the rationale established by Waclawiczek et al. (Waclawiczek et al., 2023), the elevated MAC scores in GATA2-EB patients suggest a potential favorable response to combined treatment with VEN/AZA, a prospect less likely for patients without GATA2 deficiency (Schreiber et al., 2023).

Our study employed a comprehensive approach, integrating data from the examination of the hematopoietic niche, its microenvironment, and transcriptome analysis. Through this, we observed an elevation of both BCL2 and *EZH2* with disease progression in GATA2 deficiency. This is noteworthy, because, firstly, VEN directly inhibits BCL2, and secondly, the upregulation of *EZH2*, along with H3K27me3, underscores the significance of epigenetic regulation – a domain where AZA operates, targeting epigenetic alterations. Consequently, we provide a foundation for understanding the potential therapeutic benefits of VEN and AZA individually, as well as in combination. These findings strongly suggest that patients with advanced GATA2 deficiency might benefit from treatment with VEN and AZA alone or in combination (Schreiber et al., 2023).

While the efficacy of VEN and AZA in adult AML/MDS is broadly supported by literature (DiNardo et al., 2020; Fenaux et al., 2009; Jabbour et al., 2017; Zeidan, Garcia, et al., 2021), limited knowledge exists about their use in the pediatric population.

Only recently, two retrospective studies were published, offering initial insights into the safety and beneficial outcomes of regimens involving VEN and VEN/AZA in pediatric MDS (Masetti et al., 2023; Winters et al., 2020). Our findings significantly contribute to this growing evidence by providing additional support for the use of VEN/AZA for pediatric patients with advanced GATA2 deficiency (Schreiber et al., 2023). Additionally, we lay the groundwork for an easily implementable prognostic tool for pediatric MDS, warranting further validation in larger cohorts of children to assess its potential integration into routine diagnostics.

4.7 Chronic Inflammation Beyond Pyroptosis: The Significance of NLRP3 and CASP1 in Pediatric GATA2 Deficiency

In light of our observations delineating an acquired resistance to apoptotic cell death with disease progression in GATA2 deficiency, our attention shifted towards investigating pyroptosis, an alternative form of regulated cell death known for its lytic and pro-inflammatory nature, in contrast to apoptosis (Boise & Collins, 2001; Fink & Cookson, 2005).

Within the pyroptosis signaling cascade, the activation of NLRP3 by extracellular alarmins S100 calcium binding protein A8 (S100A8) and S100A9 serves as pivotal event (Simard et al., 2013). Subsequently, the formation of the NLRP3 inflammasome complex is facilitated by NLRP3 recruiting apoptosis-associated speck-like protein (ASC), which contains a caspase-recruitment domain and binds pro-CASP1 (Bergsbaken et al., 2009).

Upon activation, the inflammasome orchestrates the cleavage and activation of pro-CASP1 into its mature, catalytically active form via ASC. CASP1 cleavage initiates diverse cellular processes, including the cleavage of GSDMD, which then translocates to the plasma membrane, initiating pore formation (Sborgi et al., 2016; Shi et al., 2015). These pores allow the influx of small molecules and ions into the cell, inducing local osmotic changes, cell swelling, and ultimately lysis (Zhang et al., 2018). This process releases intracellular inflammatory mediators into the extracellular milieu, propagating local inflammation (Bergsbaken et al., 2009; Hersh et al., 1999). Additionally, cleaved CASP1 converts precursor forms of the inflammatory cytokines

IL1B and IL18 into their active forms, further contributing to the inflammatory milieu (Sallman et al., 2016).

In our effort to delineate key players in the pyroptosis pathway, we investigated the expression of S100A9, NLRP3, cleaved CASP1, and cleaved GSDMD. While S100A9 showed a tendency towards increased levels in advanced GATA2 deficiency, NLRP3, and cleaved CASP1 exhibited substantial and significant upregulation with disease progression, reaching levels approximately three times higher in GATA2-EB compared to $GATA2^{WT}$ patients.

Remarkably, our observations represent pioneering work in the pediatric disease landscape, as there is currently no study published investigating the role of pyroptosis in the context of pediatric MDS or GATA2 deficiency. However, in adult MDS, a 2016 study by Basiorka et al. proposes NLRP3 inflammasome activation, in both low- and high-risk patients, as a key feature of the MDS phenotype, leading to elevated CASP1 levels and inducing pyroptotic cell death (Basiorka et al., 2016).

To ensure the specificity of our analysis, we focused on events characteristic to pyroptosis downstream of CASP1 activation, namely GSDMD cleavage and the observation of GSDMD-immunopositive cellular debris that can be found upon cell membrane rupture and lysis (X. Chen et al., 2016). Our visual inspection of IHC stainings for cleaved GSDMD yielded no indication of larger mean cell areas attributed to cell swelling or GSDMD-positive cellular debris, suggesting cellular viability. Additionally, the immunoreactive scores for cleaved GSDMD in our cohort were predominantly negative. This signifies that GSDMD is not activated, and, consequently, not primed to initiate pore formation.

In conclusion, our findings indicate activation of initial steps in the pyroptosis pathway, specifically through increased NLRP3 and cleaved CASP1 expression in advanced GATA2 deficiency. However, downstream events leading to pore formation and full pyroptosis execution may not occur or may be incomplete. This nuanced understanding is crucial for enhancing our comprehension of the cellular response and provides valuable insights into specific stages of the pyroptotic pathway that may be impacted in pediatric GATA2 deficiency. To reinforce the conclusion that full pyroptosis is not executed, measurement of a suitable molecular marker for end-stage lytic cell death could be beneficial. Notably, large molecules are impermeable

through the pores created by cleaved GSDMD and can only be released upon membrane rupture and cell lysis (McKenzie et al., 2020).

Consequently, we propose a refined focus for GATA2 deficiency, emphasizing the contribution of pyroptosis to a chronic feed-forward inflammatory process over cell death. In this scenario, NLRP3 and CASP1 play crucial roles in initiating and regulating the inflammatory response in the human body. NLRP3 is essential for inflammasome formation, activating CASP1, which, in turn, leads to the activation of pro-inflammatory cytokines like IL1B and IL18. Initial indications of the importance of these cytokines in GATA2 deficiency were found through their upregulation in GATA2-EB at mRNA level in our transcriptome analysis. These cytokines can exit the cell via various non-lytic pathways, such as direct transporters or exocytosis in secretory lysosomes, and do not rely on pyroptosis (Andrei et al., 2004; Qu et al., 2007). They contribute to the inflammatory response by recruiting immune cells and promoting inflammation at the site of infection or tissue damage (Dinarello, 2009).

4.8 Induction of TIM-3 in Advanced GATA2 Deficiency and its Implications for Targeted Therapy

Inflammation plays a crucial role in the immune response, orchestrating rapid and localized reactions to infections or injuries. However, when inflammation becomes persistent or chronic, it leads to prolonged activation of the immune system. Therefore, in addition to our examination of pyroptosis and its involvement in inflammation, it is essential to investigate the immune response within the context of GATA2 deficiency. The complex nature of MDS has prompted extensive research on the contribution of genetic and epigenetic factors to its pathophysiology (Gañán-Gómez et al., 2015). Recent evidence, however, indicates a link between immune dysregulation and the progression to secondary AML (Ivy & Brent Ferrell, 2018; Takeuchi & Akira, 2010). While the impairment of Toll-like receptor signaling pathways has been a central focus in understanding the influence of the innate immune response (Takeuchi & Akira, 2010; Wang et al., 2018), information regarding the impact of the adaptive immune system, especially T cell surveillance, in MDS remains limited.

In the bone marrow microenvironment of healthy donors, Bauer et al. observed a distinct absence of CD3-CD8-positive T cells, highlighting the unique immune landscape in a healthy hematopoietic niche (Bauer et al., 2021). In contrast, their exploration of MDS and secondary AML patients revealed the presence of this CD8-positive T cell subset, shedding light on altered immune composition within the microenvironment in MDS and potential implications for its pathogenesis. This aligns with existing evidence emphasizing the crucial role of the bone marrow microenvironment in regulating the neoplastic stem cell pool (Bauer et al., 2021; Ding et al., 2012).

Exploring the dynamics of CD8-positive T cells in the context of our study, we observed intriguing patterns. During acute viral infections, naïve CD8-positive T cells undergo expansion, differentiating into effector T cells (Kurtulus et al., 2011). Subsequent to the elimination of the threat, the majority of these effector T cells experience programmed cell death, whereas a small portion transitions into the memory T cell state. The BCL2 family has been identified as a key player in this process, with BCL2 protecting CD8-positive T cells from cell death (Joshi et al., 2007; Kurtulus et al., 2010).

Intriguingly, our investigation revealed an increased expression of BCL2 in CD8-positive cells during early stages of disease, particularly in RCC and GATA2-RCC. This suggests a potential role of BCL2 in safeguarding this specific T cell subset within the evolving immune microenvironment of pediatric MDS. However, as the disease progressed, the expression of BCL2 in CD8-positive cells decreased. This nuanced shift indicates that the initially established survival advantage via BCL2 may not be sustained over an extended period, potentially creating a dynamic environment where other immune perturbations may arise.

In the context of MDS, characterized by persistent or chronic antigen stimulation rather than acute viral infection, T cells may undergo a gradual reduction in cellular functions due to immune-inhibitory molecules such as TIM-3 or PD-1, leading to a state termed “exhaustion” (Yi et al., 2010). During acute infections, these inhibitory checkpoint receptors limit the severity of the immune response and are downregulated as the pathogen is cleared. However, with chronic antigen stimulation, the exhausted state is established due to a sustained elevated expression of the inhibitory

checkpoint receptors, which negatively regulate the functional and proliferative potential of affected T cells (Blackburn et al., 2009; Wherry et al., 2007). Notably, TIM-3 has been shown to influence the exhausted state of T cells significantly, and in the context of Human Immunodeficiency Virus Type 1 or Hepatitis C Virus infections, the level of TIM-3 expression has been reported to parallel the exhausted state of the cells (Golden-Mason et al., 2009; Jones et al., 2008).

Our results substantiate this concept by revealing increased BCL2 expression in TIM-3-positive cells, a phenomenon exclusive to disease progression in GATA2 deficiency. This suggests that, within this context, the initially increased survival of CD8-positive cells may have shifted to a sustained survival of TIM-3-positive cells. Previous studies in adult MDS have highlighted an association of TIM-3 with T cell defects, with a higher percentage of TIM-3 linked to an increased risk of transformation from MDS to AML (J. Tao et al., 2016; J. L. Tao et al., 2014). Extending these insights to the pediatric disease landscape, the overall elevated levels of TIM-3-positive cells we observed in GATA2-EB serve as a focal point for further investigation. Given the inconclusive nature of our results regarding PD-1, it would be beneficial to evaluate the expression of additional markers crucial for T cell exhaustion, such as lymphocyte activation gene 3 protein (LAG-3), cytotoxic T lymphocyte antigen 4 (CTLA-4), and indoleamine 2,3 dioxygenase (IDO) (Munn & Mellor, 2013; Rowshanravan et al., 2018; Yi et al., 2010).

In the context of adult MDS, there is a growing body of evidence advocating for the use of immune checkpoint inhibition to restore immune surveillance (Fu et al., 2019; Ozkazanc et al., 2016; Rezaei et al., 2021; J. Tao et al., 2016). TIM-3 inhibitors, such as sabatolimab, are currently under investigation in ongoing clinical trials for immunotherapy in MDS and AML, with preliminary data showing promising response rates and safety (Borate et al., 2019; Brunner et al., 2024; Zeidan, Al-Kali, et al., 2021). Our results, indicating increased TIM-3 expression with disease progression in pediatric GATA2 deficiency, can lend support to considering TIM-3 as a candidate for targeted therapy within this context. However, as some clinical trials have only explored TIM-3 blockade in combination with other checkpoint inhibitors or hypomethylating agents, further research is needed to better understand the mechanisms of TIM-3 inhibition and optimize its use for immunotherapy.

4.9 Potential Implications of CCL18 for Inflammation and Dysregulated Immune Response in GATA2 Deficiency

In our transcriptome analysis, coupled with subsequent mIF stainings, increased expression of CCL18 was observed primarily in patients with advanced GATA2 deficiency. Additionally, our findings reveal TIM-3 induction and heightened inflammation via NLRP3 activation. This suggests that CCL18 may act as a pivotal link between inflammation and dysregulated immune response, potentially contributing to both processes.

Regarding inflammation, the chemotactic activity of CCL18 towards immune cells, including monocytes (Schraufstatter et al., 2004), dendritic cells (Vulcano et al., 2003), and T cells (Adema et al., 1997; Chenivesse et al., 2012), is noteworthy. By recruiting immune cells to sites of inflammation, CCL18 may contribute to inflammatory processes mediated by activated NLRP3. Furthermore, CCL18 has been shown to modulate macrophage activity. In the context of chronic inflammation, these macrophages may produce pro-inflammatory cytokines such as IL1B and IL18 (Arango Duque & Descoteaux, 2014; Y. Chen et al., 2019), whose significance has been indicated in our transcriptome analysis. This could further amplify the inflammatory response in this setting.

Concerning the immune response, accumulating evidence suggests that CCL18 may counteract an effective anti-tumor response by inducing an immunosuppressive state in macrophages and dendritic cells, thereby compromising immune surveillance (Azzaoui et al., 2011; Cardoso et al., 2021; Schraufstatter et al., 2004). Moreover, CCL18 has been reported to suppress effector T cell proliferation (Azzaoui et al., 2011; Chang et al., 2010), which may further contribute to T cell exhaustion.

Given that the upregulated expression of CCL18 was exclusively found in patients with advanced GATA2 deficiency, and not in GATA2^{WT}, we hypothesized a potential regulatory role of GATA2 on CCL18. However, our attempts to investigate this hypothesis using two hematologic cell lines expressing GATA2 and CCL18, either constitutively or upon PMA stimulation, were inconclusive. This may be attributed to discrepancies between the reported expression profiles of KG-1 and K-562 cells, published in the late 1990s (Hieshima et al., 1997; St Louis et al., 1999), and our

experimental conditions. Notably, these expression profiles have not been confirmed in more recent publications, which could explain why we did not observe a discernible CCL18 band in our Western blot analyses as expected in both cell lines. Consequently, alternative cell lines expressing both GATA2 and CCL18, such as A549 cells (Luo et al., 2023), warrant further investigation. Establishing a cell line model would enable robust testing of whether GATA2 regulates CCL18, potentially through chromatin immunoprecipitation assays.

To further elucidate the connection between CCL18, T cell exhaustion, and inflammation, migration assays could be conducted to assess CCL18's chemotactic activity. Ideally, patient and healthy donor samples could be utilized to isolate different T cell subsets such as CD8-positive T cells, monocytes, and/or macrophages. Following migration assays, flow cytometry-based analysis could be employed to assess changes in immune phenotypes of the migrated cells, particularly signs of T cell exhaustion or alterations in phenotype after exposure to CCL18.

Overall, these proposed experiments aim to deepen our understanding of the role of CCL18 in the context of GATA2 deficiency, inflammation, and immune response, potentially uncovering therapeutic targets for this condition.

4.10 Conclusion

Through systematic investigation, integrating comprehensive data from the examination of hematopoiesis, the hematopoietic niche, its microenvironment, and transcriptome analysis, this study significantly advances our understanding of mechanisms of transformation and potential predictive markers in pediatric GATA2 deficiency.

The identification of increased histone trimethylation and deregulated apoptosis as potential drivers of malignant transformation provides crucial insights into disease progression in GATA2 deficiency. These findings not only shed light on the pathophysiology of the disease but also hold the potential to customize therapeutic approaches for affected patients. Notably, there is significant promise in treatment regimens involving VEN and AZA, either separately or in combination, for GATA2-EB patients (Schreiber et al., 2023).

Furthermore, our research establishes a foundation for further investigation into the intricate interplay between immune response and inflammation in pediatric GATA2 deficiency. The observed activation of NLRP3 could initiate a chronic inflammatory process, involving pro-inflammatory cytokines IL1B and IL18. This prolonged exposure to inflammatory signals may ultimately result in a dysregulated immune response, as indicated by the induced expression of the immune-inhibitory molecule TIM-3 in advanced GATA2 deficiency.

In conclusion, this doctoral research not only provides predictive markers for disease progression in GATA2 deficiency but also contributes to a deeper comprehension of the disease landscape. These insights hold the potential to refine diagnostic and therapeutic strategies, ultimately advancing patient care and improving outcomes for pediatric patients affected by GATA2 deficiency.

References

Adams, J. M., & Cory, S. (2018). The BCL-2 arbiters of apoptosis and their growing role as cancer targets. *Cell Death Differ, 25*(1), 27-36. doi:10.1038/cdd.2017.161

Adema, G. J., Hartgers, F., Verstraten, R., de Vries, E., Marland, G., Menon, S., . . . Figdor, C. G. (1997). A dendritic-cell-derived C-C chemokine that preferentially attracts naive T cells. *Nature, 387*(6634), 713-717. doi:10.1038/42716

Alter, B. P., Giri, N., Savage, S. A., Peters, J. A., Loud, J. T., Leathwood, L., . . . Rosenberg, P. S. (2010). Malignancies and survival patterns in the National Cancer Institute inherited bone marrow failure syndromes cohort study. *Br J Haematol, 150*(2), 179-188. doi:10.1111/j.1365-2141.2010.08212.x

Andrei, C., Margiocco, P., Poggi, A., Lotti, L. V., Torrisi, M. R., & Rubartelli, A. (2004). Phospholipases C and A2 control lysosome-mediated IL-1 beta secretion: Implications for inflammatory processes. *Proc Natl Acad Sci U S A, 101*(26), 9745-9750. doi:10.1073/pnas.0308558101

Arango Duque, G., & Descoteaux, A. (2014). Macrophage cytokines: involvement in immunity and infectious diseases. *Front Immunol, 5*, 491. doi:10.3389/fimmu.2014.00491

Arber, D. A., Orazi, A., Hasserjian, R. P., Borowitz, M. J., Calvo, K. R., Kvasnicka, H. M., . . . Tefferi, A. (2022). International Consensus Classification of Myeloid Neoplasms and Acute Leukemias: integrating morphologic, clinical, and genomic data. *Blood, 140*(11), 1200-1228. doi:10.1182/blood.2022015850

Asou, H., Matsui, H., Ozaki, Y., Nagamachi, A., Nakamura, M., Aki, D., & Inaba, T. (2009). Identification of a common microdeletion cluster in 7q21.3 subband among patients with myeloid leukemia and myelodysplastic syndrome. *Biochem Biophys Res Commun, 383*(2), 245-251. doi:10.1016/j.bbrc.2009.04.004

Azzaoui, I., Yahia, S. A., Chang, Y., Vorng, H., Morales, O., Fan, Y., . . . Tsicopoulos, A. (2011). CCL18 differentiates dendritic cells in tolerogenic cells able to prime regulatory T cells in healthy subjects. *Blood, 118*(13), 3549-3558. doi:10.1182/blood-2011-02-338780

Basiorka, A. A., McGraw, K. L., Eksioglu, E. A., Chen, X., Johnson, J., Zhang, L., . . . List, A. F. (2016). The NLRP3 inflammasome functions as a driver of the myelodysplastic syndrome phenotype. *Blood, 128*(25), 2960-2975. doi:10.1182/blood-2016-07-730556

Bauer, M., Vaxevanis, C., Al-Ali, H. K., Jaekel, N., Naumann, C. L. H., Schaffrath, J., . . . Wickenhauser, C. (2021). Altered Spatial Composition of the Immune Cell Repertoire in Association to CD34(+) Blasts in Myelodysplastic Syndromes and Secondary Acute Myeloid Leukemia. *Cancers (Basel), 13*(2). doi:10.3390/cancers13020186

Baumann, I., Führer, M., Behrendt, S., Campr, V., Csomor, J., Furlan, I., . . . Schwarz, S. (2012). Morphological differentiation of severe aplastic anaemia from hypocellular refractory cytopenia of childhood: reproducibility of histopathological diagnostic criteria. *Histopathology, 61*(1), 10-17. doi:10.1111/j.1365-2559.2011.04156.x

Bejar, R., Stevenson, K., Abdel-Wahab, O., Galili, N., Nilsson, B., Garcia-Manero, G., . . . Ebert, B. L. (2011). Clinical effect of point mutations in myelodysplastic syndromes. *N Engl J Med, 364*(26), 2496-2506. doi:10.1056/NEJMoa1013343

Bergsbaken, T., Fink, S. L., & Cookson, B. T. (2009). Pyroptosis: host cell death and inflammation. *Nat Rev Microbiol, 7*(2), 99-109. doi:10.1038/nrmicro2070

Bigley, V., Haniffa, M., Doulatov, S., Wang, X. N., Dickinson, R., McGovern, N., . . . Collin, M. (2011). The human syndrome of dendritic cell, monocyte, B and NK lymphoid deficiency. *J Exp Med, 208*(2), 227-234. doi:10.1084/jem.20101459

Blackburn, S. D., Shin, H., Haining, W. N., Zou, T., Workman, C. J., Polley, A., . . . Wherry, E. J. (2009). Coregulation of CD8+ T cell exhaustion by multiple inhibitory receptors during chronic viral infection. *Nat Immunol, 10*(1), 29-37. doi:10.1038/ni.1679

Boise, L. H., & Collins, C. M. (2001). Salmonella-induced cell death: apoptosis, necrosis or programmed cell death? *Trends Microbiol, 9*(2), 64-67. doi:10.1016/s0966-842x(00)01937-5

Borate, U., Esteve, J., Porkka, K., Knapper, S., Vey, N., Scholl, S., . . . Wei, A. H. (2019). Phase Ib Study of the Anti-TIM-3 Antibody MBG453 in Combination with Decitabine in Patients with High-Risk Myelodysplastic Syndrome (MDS) and Acute Myeloid Leukemia (AML). *Blood, 134*, 570. doi:10.1182/blood-2019-128178

Boudard, D., Vasselon, C., Berthéas, M. F., Jaubert, J., Mounier, C., Reynaud, J., . . . Campos, L. (2002). Expression and prognostic significance of Bcl-2 family proteins in myelodysplastic syndromes. *Am J Hematol, 70*(2), 115-125. doi:10.1002/ajh.10108

Bresnick, E. H., Jung, M. M., & Katsumura, K. R. (2020). Human GATA2 mutations and hematologic disease: how many paths to pathogenesis? *Blood Adv, 4*(18), 4584-4592. doi:10.1182/bloodadvances.2020002953

Bresnick, E. H., Katsumura, K. R., Lee, H. Y., Johnson, K. D., & Perkins, A. S. (2012). Master regulatory GATA transcription factors: mechanistic principles and emerging links to hematologic malignancies. *Nucleic Acids Res, 40*(13), 5819-5831. doi:10.1093/nar/gks281

Brown, K., Gerstberger, S., Carlson, L., Franzoso, G., & Siebenlist, U. (1995). Control of I kappa B-alpha proteolysis by site-specific, signal-induced phosphorylation. *Science, 267*(5203), 1485-1488. doi:10.1126/science.7878466

Brunner, A. M., Esteve, J., Porkka, K., Knapper, S., Traer, E., Scholl, S., . . . Wei, A. H. (2024). Phase Ib study of sabatolimab (MBG453), a novel immunotherapy targeting TIM-3 antibody, in combination with decitabine or azacitidine in high- or very high-risk myelodysplastic syndromes. *Am J Hematol, 99*(2), E32-e36. doi:10.1002/ajh.27161

Calvo, K. R., Vinh, D. C., Maric, I., Wang, W., Noel, P., Stetler-Stevenson, M., . . . Holland, S. M. (2011). Myelodysplasia in autosomal dominant and sporadic monocytopenia immunodeficiency syndrome: diagnostic features and clinical implications. *Haematologica, 96*(8), 1221-1225. doi:10.3324/haematol.2011.041152

Cao, R., Wang, L., Wang, H., Xia, L., Erdjument-Bromage, H., Tempst, P., . . . Zhang, Y. (2002). Role of histone H3 lysine 27 methylation in Polycomb-group silencing. *Science, 298*(5595), 1039-1043. doi:10.1126/science.1076997

Cardoso, A. P., Pinto, M. L., Castro, F., Costa Â, M., Marques-Magalhães, Â., Canha-Borges, A., . . . Oliveira, M. J. (2021). The immunosuppressive and pro-tumor functions of CCL18 at the tumor microenvironment. *Cytokine Growth Factor Rev, 60*, 107-119. doi:10.1016/j.cytogfr.2021.03.005

Chang, Y., de Nadai, P., Azzaoui, I., Morales, O., Delhem, N., Vorng, H., . . . Tsicopoulos, A. (2010). The chemokine CCL18 generates adaptive regulatory T cells from memory CD4+ T cells of healthy but not allergic subjects. *Faseb j, 24*(12), 5063-5072. doi:10.1096/fj.10-162560

Chen, M. J., Yokomizo, T., Zeigler, B. M., Dzierzak, E., & Speck, N. A. (2009). Runx1 is required for the endothelial to haematopoietic cell transition but not thereafter. *Nature, 457*(7231), 887-891. doi:10.1038/nature07619

Chen, X., He, W. T., Hu, L., Li, J., Fang, Y., Wang, X., . . . Han, J. (2016). Pyroptosis is driven by non-selective gasdermin-D pore and its morphology is different from MLKL channel-mediated necroptosis. *Cell Res, 26*(9), 1007-1020. doi:10.1038/cr.2016.100

Chen, Y., Song, Y., Du, W., Gong, L., Chang, H., & Zou, Z. (2019). Tumor-associated macrophages: an accomplice in solid tumor progression. *J Biomed Sci, 26*(1), 78. doi:10.1186/s12929-019-0568-z

Chenivesse, C., Chang, Y., Azzaoui, I., Ait Yahia, S., Morales, O., Plé, C., . . . Tsicopoulos, A. (2012). Pulmonary CCL18 recruits human regulatory T cells. *J Immunol, 189*(1), 128-137. doi:10.4049/jimmunol.1003616

Danaher, P., Warren, S., Dennis, L., D'Amico, L., White, A., Disis, M. L., . . . Fling, S. P. (2017). Gene expression markers of Tumor Infiltrating Leukocytes. *J Immunother Cancer, 5*, 18. doi:10.1186/s40425-017-0215-8

de Pater, E., Kaimakis, P., Vink, C. S., Yokomizo, T., Yamada-Inagawa, T., van der Linden, R., . . . Dzierzak, E. (2013). Gata2 is required for HSC generation and survival. *J Exp Med, 210*(13), 2843-2850. doi:10.1084/jem.20130751

de Souza Fernandez, T., Fonseca Alvarenga, T., Almeida Antônio de Kós, E., Lamim Lovatel, V., Tavares, R. C., da Costa, E. S., . . . Abdelhay, E. (2019). Aberrant Expression of EZH2 in Pediatric Patients with Myelodysplastic Syndrome: A Potential Biomarker of Leukemic Evolution. *Biomed Res Int, 2019*, 3176565. doi:10.1155/2019/3176565

Dickinson, R. E., Griffin, H., Bigley, V., Reynard, L. N., Hussain, R., Haniffa, M., . . . Collin, M. (2011). Exome sequencing identifies GATA-2 mutation as the cause of dendritic cell, monocyte, B and NK lymphoid deficiency. *Blood, 118*(10), 2656-2658. doi:10.1182/blood-2011-06-360313

DiNardo, C. D., Jonas, B. A., Pullarkat, V., Thirman, M. J., Garcia, J. S., Wei, A. H., . . . Pratz, K. W. (2020). Azacitidine and Venetoclax in Previously Untreated Acute Myeloid Leukemia. *N Engl J Med, 383*(7), 617-629. doi:10.1056/NEJMoa2012971

Dinarello, C. A. (2009). Immunological and inflammatory functions of the interleukin-1 family. *Annu Rev Immunol, 27*, 519-550. doi:10.1146/annurev.immunol.021908.132612

Ding, L., Saunders, T. L., Enikolopov, G., & Morrison, S. J. (2012). Endothelial and perivascular cells maintain haematopoietic stem cells. *Nature, 481*(7382), 457-462. doi:10.1038/nature10783

Donadieu, J., Lamant, M., Fieschi, C., de Fontbrune, F. S., Caye, A., Ouachee, M., . . . Pasquet, M. (2018). Natural history of GATA2 deficiency in a survey of 79 French and Belgian patients. *Haematologica, 103*(8), 1278-1287. doi:10.3324/haematol.2017.181909

Doré, L. C., Chlon, T. M., Brown, C. D., White, K. P., & Crispino, J. D. (2012). Chromatin occupancy analysis reveals genome-wide GATA factor switching during hematopoiesis. *Blood, 119*(16), 3724-3733. doi:10.1182/blood-2011-09-380634

Fenaux, P., Mufti, G. J., Hellstrom-Lindberg, E., Santini, V., Finelli, C., Giagounidis, A., . . . Silverman, L. R. (2009). Efficacy of azacitidine compared with that of conventional care regimens in the treatment of higher-risk myelodysplastic syndromes: a randomised, open-label, phase III study. *Lancet Oncol, 10*(3), 223-232. doi:10.1016/s1470-2045(09)70003-8

Figueroa, M. E., Skrabanek, L., Li, Y., Jiemjit, A., Fandy, T. E., Paietta, E., . . . Melnick, A. (2009). MDS and secondary AML display unique patterns and abundance of aberrant DNA methylation. *Blood, 114*(16), 3448-3458. doi:10.1182/blood-2009-01-200519

Fink, S. L., & Cookson, B. T. (2005). Apoptosis, pyroptosis, and necrosis: mechanistic description of dead and dying eukaryotic cells. *Infect Immun, 73*(4), 1907-1916. doi:10.1128/iai.73.4.1907-1916.2005

Fu, R., Li, L., Hu, J., Wang, Y., Tao, J., Liu, H., . . . Zhang, W. (2019). Elevated TIM3 expression of T helper cells affects immune system in patients with myelodysplastic syndrome. *J Investig Med, 67*(8), 1125-1130. doi:10.1136/jim-2019-001059

Gañán-Gómez, I., Wei, Y., Starczynowski, D. T., Colla, S., Yang, H., Cabrero-Calvo, M., . . . Garcia-Manero, G. (2015). Deregulation of innate immune and inflammatory signaling in myelodysplastic syndromes. *Leukemia, 29*(7), 1458-1469. doi:10.1038/leu.2015.69

Göhring, G., Michalova, K., Beverloo, H. B., Betts, D., Harbott, J., Haas, O. A., . . . Schlegelberger, B. (2010). Complex karyotype newly defined: the strongest prognostic factor in advanced childhood myelodysplastic syndrome. *Blood, 116*(19), 3766-3769. doi:10.1182/blood-2010-04-280313

Golden-Mason, L., Palmer, B. E., Kassam, N., Townshend-Bulson, L., Livingston, S., McMahon, B. J., . . . Rosen, H. R. (2009). Negative immune regulator Tim-3 is overexpressed on T cells in hepatitis C virus infection and its blockade rescues dysfunctional CD4+ and CD8+ T cells. *J Virol, 83*(18), 9122-9130. doi:10.1128/jvi.00639-09

Göllner, S., Oellerich, T., Agrawal-Singh, S., Schenk, T., Klein, H. U., Rohde, C., . . . Müller-Tidow, C. (2017). Loss of the histone methyltransferase EZH2 induces resistance to multiple drugs in acute myeloid leukemia. *Nat Med, 23*(1), 69-78. doi:10.1038/nm.4247

Guerrini, L., Casalino, L., Corti, A., & Blasi, F. (1996). NF-kappa B-mediated regulation of urokinase gene expression by PMA and TNF-alpha in human A549 cells. *FEBS Lett, 393*(1), 69-73. doi:10.1016/0014-5793(96)00854-x

Hahn, C. N., Chong, C. E., Carmichael, C. L., Wilkins, E. J., Brautigan, P. J., Li, X. C., . . . Scott, H. S. (2011). Heritable GATA2 mutations associated with familial myelodysplastic syndrome and acute myeloid leukemia. *Nat Genet, 43*(10), 1012-1017. doi:10.1038/ng.913

Hasle, H., Aricò, M., Basso, G., Biondi, A., Cantù Rajnoldi, A., Creutzig, U., . . . Zimmermann, M. (1999). Myelodysplastic syndrome, juvenile myelomonocytic leukemia, and acute myeloid leukemia associated with complete or partial monosomy 7. European Working Group on MDS in Childhood (EWOG-MDS). *Leukemia, 13*(3), 376-385. doi:10.1038/sj.leu.2401342

Hasle, H., Kerndrup, G., & Jacobsen, B. B. (1995). Childhood myelodysplastic syndrome in Denmark: incidence and predisposing conditions. *Leukemia, 9*(9), 1569-1572.

Hasle, H., Niemeyer, C. M., Chessells, J. M., Baumann, I., Bennett, J. M., Kerndrup, G., & Head, D. R. (2003). A pediatric approach to the WHO classification of myelodysplastic and myeloproliferative diseases. *Leukemia, 17*(2), 277-282. doi:10.1038/sj.leu.2402765

Hersh, D., Monack, D. M., Smith, M. R., Ghori, N., Falkow, S., & Zychlinsky, A. (1999). The Salmonella invasin SipB induces macrophage apoptosis by binding to caspase-1. *Proc Natl Acad Sci U S A, 96*(5), 2396-2401. doi:10.1073/pnas.96.5.2396

Hieshima, K., Imai, T., Baba, M., Shoudai, K., Ishizuka, K., Nakagawa, T., . . . Nomiyama, H. (1997). A novel human CC chemokine PARC that is most homologous to macrophage-inflammatory protein-1 alpha/LD78 alpha and chemotactic for T lymphocytes, but not for monocytes. *J Immunol, 159*(3), 1140-1149.

Hirabayashi, S., Flotho, C., Moetter, J., Heuser, M., Hasle, H., Gruhn, B., . . . Wlodarski, M. W. (2012). Spliceosomal gene aberrations are rare, coexist with oncogenic mutations, and are unlikely to exert a driver effect in childhood MDS and JMML. *Blood, 119*(11), e96-99. doi:10.1182/blood-2011-12-395087

Hirabayashi, S., Wlodarski, M. W., Kozyra, E., & Niemeyer, C. M. (2017). Heterogeneity of GATA2-related myeloid neoplasms. *Int J Hematol, 106*(2), 175-182. doi:10.1007/s12185-017-2285-2

Hofmann, I. (2015). Pediatric myelodysplastic syndromes. *Journal of Hematopathology, 8*, 127-141.

Horny, H. P., Greschniok, A., Jordan, J. H., Menke, D. M., & Valent, P. (2003). Chymase expressing bone marrow mast cells in mastocytosis and myelodysplastic syndromes: an immunohistochemical and morphometric study. *J Clin Pathol, 56*(2), 103-106. doi:10.1136/jcp.56.2.103

Hsu, A. P., Sampaio, E. P., Khan, J., Calvo, K. R., Lemieux, J. E., Patel, S. Y., . . . Holland, S. M. (2011). Mutations in GATA2 are associated with the autosomal dominant and sporadic monocytopenia and mycobacterial infection (MonoMAC) syndrome. *Blood, 118*(10), 2653-2655. doi:10.1182/blood-2011-05-356352

Huang, K., O'Neill, K. L., Li, J., Zhou, W., Han, N., Pang, X., . . . Luo, X. (2019). BH3-only proteins target BCL-xL/MCL-1, not BAX/BAK, to initiate apoptosis. *Cell Res, 29*(11), 942-952. doi:10.1038/s41422-019-0231-y

Issa, J. P. (2013). The myelodysplastic syndrome as a prototypical epigenetic disease. *Blood, 121*(19), 3811-3817. doi:10.1182/blood-2013-02-451757

Ivy, K. S., & Brent Ferrell, P., Jr. (2018). Disordered Immune Regulation and its Therapeutic Targeting in Myelodysplastic Syndromes. *Curr Hematol Malig Rep, 13*(4), 244-255. doi:10.1007/s11899-018-0463-9

Jabbour, E., Short, N. J., Montalban-Bravo, G., Huang, X., Bueso-Ramos, C., Qiao, W., . . . Garcia-Manero, G. (2017). Randomized phase 2 study of low-dose decitabine vs low-dose azacitidine in lower-risk MDS and MDS/MPN. *Blood, 130*(13), 1514-1522. doi:10.1182/blood-2017-06-788497

Jilg, S., Reidel, V., Müller-Thomas, C., König, J., Schauwecker, J., Höckendorf, U., . . . Jost, P. J. (2016). Blockade of BCL-2 proteins efficiently induces apoptosis in progenitor cells of high-risk myelodysplastic syndromes patients. *Leukemia, 30*(1), 112-123. doi:10.1038/leu.2015.179

Jones, R. B., Ndhlovu, L. C., Barbour, J. D., Sheth, P. M., Jha, A. R., Long, B. R., . . . Ostrowski, M. A. (2008). Tim-3 expression defines a novel population of dysfunctional T cells with highly elevated frequencies in progressive HIV-1 infection. *J Exp Med, 205*(12), 2763-2779. doi:10.1084/jem.20081398

Joshi, N. S., Cui, W., Chandele, A., Lee, H. K., Urso, D. R., Hagman, J., . . . Kaech, S. M. (2007). Inflammation directs memory precursor and short-lived effector CD8(+) T cell fates via the graded expression of T-bet transcription factor. *Immunity, 27*(2), 281-295. doi:10.1016/j.immuni.2007.07.010

Kardos, G., Baumann, I., Passmore, S. J., Locatelli, F., Hasle, H., Schultz, K. R., . . . Niemeyer, C. M. (2003). Refractory anemia in childhood: a retrospective analysis of 67 patients with particular reference to monosomy 7. *Blood, 102*(6), 1997-2003. doi:10.1182/blood-2002-11-3444

Karoopongse, E., Yeung, C., Byon, J., Ramakrishnan, A., Holman, Z. J., Jiang, P. Y., . . . Marcondes, A. M. (2014). The KDM2B- let-7b -EZH2 axis in myelodysplastic syndromes as a target for combined epigenetic therapy. *PLoS One, 9*(9), e107817. doi:10.1371/journal.pone.0107817

Katsumura, K. R., Bresnick, E. H., & the, G. F. M. G. (2017). The GATA factor revolution in hematology. *Blood, 129*(15), 2092-2102. doi:10.1182/blood-2016-09-687871

Kazenwadel, J., Secker, G. A., Liu, Y. J., Rosenfeld, J. A., Wildin, R. S., Cuellar-Rodriguez, J., . . . Harvey, N. L. (2012). Loss-of-function germline GATA2 mutations in patients with MDS/AML or MonoMAC syndrome and primary lymphedema reveal a key role for GATA2 in the lymphatic vasculature. *Blood, 119*(5), 1283-1291. doi:10.1182/blood-2011-08-374363

Kurtulus, S., Tripathi, P., Moreno-Fernandez, M. E., Sholl, A., Katz, J. D., Grimes, H. L., & Hildeman, D. A. (2011). Bcl-2 allows effector and memory CD8+ T cells to tolerate higher expression of Bim. *J Immunol, 186*(10), 5729-5737. doi:10.4049/jimmunol.1100102

Kurtulus, S., Tripathi, P., Opferman, J. T., & Hildeman, D. A. (2010). Contracting the 'mus cells'--does down-sizing suit us for diving into the memory pool? *Immunol Rev, 236*, 54-67. doi:10.1111/j.1600-065X.2010.00920.x

Leskinen, M., Wang, Y., Leszczynski, D., Lindstedt, K. A., & Kovanen, P. T. (2001). Mast cell chymase induces apoptosis of vascular smooth muscle cells. *Arterioscler Thromb Vasc Biol, 21*(4), 516-522. doi:10.1161/01.atv.21.4.516

Letai, A., Bassik, M. C., Walensky, L. D., Sorcinelli, M. D., Weiler, S., & Korsmeyer, S. J. (2002). Distinct BH3 domains either sensitize or activate mitochondrial apoptosis, serving as prototype cancer therapeutics. *Cancer Cell, 2*(3), 183-192. doi:10.1016/s1535-6108(02)00127-7

Li, L., & Krilis, S. A. (1997). Conditioned media obtained from a human mastocytosis cell strain induce mast cells expressing chymase but not tryptase from human progenitors. *Int Arch Allergy Immunol, 113*(1-3), 289-290. doi:10.1159/000237576

Li, Y., Gao, J., Kamran, M., Harmacek, L., Danhorn, T., Leach, S. M., . . . Huang, H. (2021). GATA2 regulates mast cell identity and responsiveness to antigenic stimulation by promoting chromatin remodeling at super-enhancers. *Nat Commun, 12*(1), 494. doi:10.1038/s41467-020-20766-0

Ling, K. W., Ottersbach, K., van Hamburg, J. P., Oziemlak, A., Tsai, F. Y., Orkin, S. H., . . . Dzierzak, E. (2004). GATA-2 plays two functionally distinct roles during the ontogeny of hematopoietic stem cells. *J Exp Med, 200*(7), 871-882. doi:10.1084/jem.20031556

Linnemann, A. K., O'Geen, H., Keles, S., Farnham, P. J., & Bresnick, E. H. (2011). Genetic framework for GATA factor function in vascular biology. *Proc Natl Acad Sci U S A, 108*(33), 13641-13646. doi:10.1073/pnas.1108440108

Luo, H. Q., Huang, Y. M., Li, J., Tang, X. D., Chen, R., Wang, Y., . . . Li, X. Y. (2023). DHA inhibits invasion and metastasis in NSCLC cells by interfering with CCL18/STAT3 signaling pathway. *Clin Exp Med, 23*(6), 2311-2320. doi:10.1007/s10238-022-00906-0

Mace, E. M., Hsu, A. P., Monaco-Shawver, L., Makedonas, G., Rosen, J. B., Dropulic, L., . . . Orange, J. S. (2013). Mutations in GATA2 cause human NK cell deficiency with specific loss of the CD56(bright) subset. *Blood, 121*(14), 2669-2677. doi:10.1182/blood-2012-09-453969

Malcovati, L., Papaemmanuil, E., Ambaglio, I., Elena, C., Gallì, A., Della Porta, M. G., . . . Cazzola, M. (2014). Driver somatic mutations identify distinct disease entities within myeloid neoplasms with myelodysplasia. *Blood, 124*(9), 1513-1521. doi:10.1182/blood-2014-03-560227

Mansour, S., Connell, F., Steward, C., Ostergaard, P., Brice, G., Smithson, S., . . . Murday, V. (2010). Emberger syndrome-primary lymphedema with myelodysplasia: report of seven new cases. *Am J Med Genet A, 152a*(9), 2287-2296. doi:10.1002/ajmg.a.33445

Masetti, R., Baccelli, F., Leardini, D., Gottardi, F., Vendemini, F., Di Gangi, A., . . . Locatelli, F. (2023). Venetoclax-based therapies in pediatric advanced MDS and relapsed/refractory AML: a multicenter retrospective analysis. *Blood Adv, 7*(16), 4366-4370. doi:10.1182/bloodadvances.2023010113

McGraw, K. L., Nguyen, J., Al Ali, N. H., Komrokji, R. S., Sallman, D., Zhang, X., . . . Zhang, L. (2019). Association of EZH2 protein expression by immunohistochemistry in myelodysplasia related neoplasms with mutation status, cytogenetics and clinical outcomes. *Br J Haematol, 184*(3), 450-455. doi:10.1111/bjh.15099

McKenzie, B. A., Fernandes, J. P., Doan, M. A. L., Schmitt, L. M., Branton, W. G., & Power, C. (2020). Activation of the executioner caspases-3 and -7 promotes microglial pyroptosis in models of multiple sclerosis. *J Neuroinflammation, 17*(1), 253. doi:10.1186/s12974-020-01902-5

Munn, D. H., & Mellor, A. L. (2013). Indoleamine 2,3 dioxygenase and metabolic control of immune responses. *Trends Immunol, 34*(3), 137-143. doi:10.1016/j.it.2012.10.001

Niemeyer, C. M., & Baumann, I. (2008). Myelodysplastic syndrome in children and adolescents. *Semin Hematol, 45*(1), 60-70. doi:10.1053/j.seminhematol.2007.10.006

Nováková, M., Žaliová, M., Suková, M., Wlodarski, M., Janda, A., Froňková, E., . . . Mejstříková, E. (2016). Loss of B cells and their precursors is the most constant feature of GATA-2 deficiency in childhood myelodysplastic syndrome. *Haematologica, 101*(6), 707-716. doi:10.3324/haematol.2015.137711

Ostergaard, P., Simpson, M. A., Connell, F. C., Steward, C. G., Brice, G., Woollard, W. J., . . . Mansour, S. (2011). Mutations in GATA2 cause primary lymphedema associated with a predisposition to acute myeloid leukemia (Emberger syndrome). *Nat Genet, 43*(10), 929-931. doi:10.1038/ng.923

Ozkazanc, D., Yoyen-Ermis, D., Tavukcuoglu, E., Buyukasik, Y., & Esendagli, G. (2016). Functional exhaustion of CD4(+) T cells induced by co-stimulatory signals from myeloid leukaemia cells. *Immunology, 149*(4), 460-471. doi:10.1111/imm.12665

Parker, J. E., Mufti, G. J., Rasool, F., Mijovic, A., Devereux, S., & Pagliuca, A. (2000). The role of apoptosis, proliferation, and the Bcl-2-related proteins in the myelodysplastic syndromes and acute myeloid leukemia secondary to MDS. *Blood, 96*(12), 3932-3938.

Pasquet, M., Bellanné-Chantelot, C., Tavitian, S., Prade, N., Beaupain, B., LaRochelle, O., . . . Delabesse, E. (2013). High frequency of GATA2 mutations in patients with mild chronic neutropenia evolving to MonoMac syndrome, myelodysplasia, and acute myeloid leukemia. *Blood, 121*(5), 822-829. doi:10.1182/blood-2012-08-447367

Passmore, S. J., Chessells, J. M., Kempski, H., Hann, I. M., Brownbill, P. A., & Stiller, C. A. (2003). Paediatric myelodysplastic syndromes and juvenile myelomonocytic leukaemia in the UK: a population-based study of incidence and survival. *Br J Haematol, 121*(5), 758-767. doi:10.1046/j.1365-2141.2003.04361.x

Pastor, V. B., Sahoo, S. S., Boklan, J., Schwabe, G. C., Saribeyoglu, E., Strahm, B., . . . Wlodarski, M. W. (2018). Constitutional SAMD9L mutations cause familial myelodysplastic syndrome and transient monosomy 7. *Haematologica, 103*(3), 427-437. doi:10.3324/haematol.2017.180778

Peffault de Latour, R., & Soulier, J. (2016). How I treat MDS and AML in Fanconi anemia. *Blood, 127*(24), 2971-2979. doi:10.1182/blood-2016-01-583625

Qu, Y., Franchi, L., Nunez, G., & Dubyak, G. R. (2007). Nonclassical IL-1 beta secretion stimulated by P2X7 receptors is dependent on inflammasome activation and correlated with exosome release in murine macrophages. *J Immunol, 179*(3), 1913-1925. doi:10.4049/jimmunol.179.3.1913

Raza, A., Gezer, S., Mundle, S., Gao, X. Z., Alvi, S., Borok, R., . . . et al. (1995). Apoptosis in bone marrow biopsy samples involving stromal and hematopoietic cells in 50 patients with myelodysplastic syndromes. *Blood, 86*(1), 268-276.

Remmele, W., & Stegner, H. E. (1987). [Recommendation for uniform definition of an immunoreactive score (IRS) for immunohistochemical estrogen receptor detection (ER-ICA) in breast cancer tissue]. *Pathologe, 8*(3), 138-140.

Rezaei, M., Tan, J., Zeng, C., Li, Y., & Ganjalikhani-Hakemi, M. (2021). TIM-3 in Leukemia; Immune Response and Beyond. *Front Oncol, 11*, 753677. doi:10.3389/fonc.2021.753677

Rodrigues, N. P., Janzen, V., Forkert, R., Dombkowski, D. M., Boyd, A. S., Orkin, S. H., . . . Scadden, D. T. (2005). Haploinsufficiency of GATA-2 perturbs adult hematopoietic stem-cell homeostasis. *Blood, 106*(2), 477-484. doi:10.1182/blood-2004-08-2989

Rowshanravan, B., Halliday, N., & Sansom, D. M. (2018). CTLA-4: a moving target in immunotherapy. *Blood, 131*(1), 58-67. doi:10.1182/blood-2017-06-741033

Rudelius, M., Weinberg, O. K., Niemeyer, C. M., Shimamura, A., & Calvo, K. R. (2023). The International Consensus Classification (ICC) of hematologic neoplasms with germline predisposition, pediatric myelodysplastic syndrome, and juvenile myelomonocytic leukemia. *Virchows Arch, 482*(1), 113-130. doi:10.1007/s00428-022-03447-9

Sahoo, S. S., Kozyra, E. J., & Wlodarski, M. W. (2020). Germline predisposition in myeloid neoplasms: Unique genetic and clinical features of GATA2 deficiency and SAMD9/SAMD9L syndromes. *Best Pract Res Clin Haematol, 33*(3), 101197. doi:10.1016/j.beha.2020.101197

Sahoo, S. S., Pastor Loyola, V., Panda, P. K., Szvetnik, E. A., Kozyra, E. J., Voss, R. K., . . . Wlodarski, M. W. (2018). SAMD9 and SAMD9L Germline Disorders in Patients Enrolled in Studies of the European Working Group of MDS in Childhood (EWOG-MDS): Prevalence, Outcome, Phenotype and Functional Characterisation. *Blood, 132*(Supplement 1), 643-643. doi:10.1182/blood-2018-99-118389

Sallman, D. A., Cluzeau, T., Basiorka, A. A., & List, A. (2016). Unraveling the Pathogenesis of MDS: The NLRP3 Inflammasome and Pyroptosis Drive the MDS Phenotype. *Front Oncol, 6*, 151. doi:10.3389/fonc.2016.00151

Sborgi, L., Rühl, S., Mulvihill, E., Pipercevic, J., Heilig, R., Stahlberg, H., . . . Hiller, S. (2016). GSDMD membrane pore formation constitutes the mechanism of pyroptotic cell death. *Embo j, 35*(16), 1766-1778. doi:10.15252/embj.201694696

Schraufstatter, I., Takamori, H., Sikora, L., Sriramarao, P., & DiScipio, R. G. (2004). Eosinophils and monocytes produce pulmonary and activation-regulated chemokine, which activates cultured monocytes/macrophages. *Am J Physiol Lung Cell Mol Physiol, 286*(3), L494-501. doi:10.1152/ajplung.00323.2002

Schreiber, F., Piontek, G., Schneider-Kimoto, Y., Schwarz-Furlan, S., De Vito, R., Locatelli, F., . . . Rudelius, M. (2023). Development of MDS in Pediatric Patients with GATA2 Deficiency: Increased Histone Trimethylation and Deregulated Apoptosis as Potential Drivers of Transformation. *Cancers (Basel), 15*(23). doi:10.3390/cancers15235594

Schutyser, E., Richmond, A., & Van Damme, J. (2005). Involvement of CC chemokine ligand 18 (CCL18) in normal and pathological processes. *J Leukoc Biol, 78*(1), 14-26. doi:10.1189/jlb.1204712

Schwartz, J. R., Ma, J., Lamprecht, T., Walsh, M., Wang, S., Bryant, V., . . . Klco, J. M. (2017). The genomic landscape of pediatric myelodysplastic syndromes. *Nat Commun, 8*(1), 1557. doi:10.1038/s41467-017-01590-5

Shi, J., Zhao, Y., Wang, K., Shi, X., Wang, Y., Huang, H., . . . Shao, F. (2015). Cleavage of GSDMD by inflammatory caspases determines pyroptotic cell death. *Nature, 526*(7575), 660-665. doi:10.1038/nature15514

Shimamura, A., & Alter, B. P. (2010). Pathophysiology and management of inherited bone marrow failure syndromes. *Blood Rev, 24*(3), 101-122. doi:10.1016/j.blre.2010.03.002

Simard, J. C., Cesaro, A., Chapeton-Montes, J., Tardif, M., Antoine, F., Girard, D., & Tessier, P. A. (2013). S100A8 and S100A9 induce cytokine expression and regulate the NLRP3 inflammasome via ROS-dependent activation of NF-κB(1.). *PLoS One, 8*(8), e72138. doi:10.1371/journal.pone.0072138

Spinner, M. A., Sanchez, L. A., Hsu, A. P., Shaw, P. A., Zerbe, C. S., Calvo, K. R., . . . Holland, S. M. (2014). GATA2 deficiency: a protean disorder of hematopoiesis, lymphatics, and immunity. *Blood, 123*(6), 809-821. doi:10.1182/blood-2013-07-515528

St Louis, D. C., Woodcock, J. B., Franzoso, G., Blair, P. J., Carlson, L. M., Murillo, M., . . . Lee, K. P. (1999). Evidence for distinct intracellular signaling pathways in CD34+ progenitor to dendritic cell differentiation from a human cell line model. *J Immunol, 162*(6), 3237-3248.

Stomper, J., Meier, R., Ma, T., Pfeifer, D., Ihorst, G., Blagitko-Dorfs, N., . . . Lübbert, M. (2021). Integrative study of EZH2 mutational status, copy number, protein expression and H3K27 trimethylation in AML/MDS patients. *Clin Epigenetics, 13*(1), 77. doi:10.1186/s13148-021-01052-2

Takeuchi, O., & Akira, S. (2010). Pattern recognition receptors and inflammation. *Cell, 140*(6), 805-820. doi:10.1016/j.cell.2010.01.022

Tao, J., Li, L., Wang, Y., Fu, R., Wang, H., & Shao, Z. (2016). Increased TIM3+CD8+T cells in Myelodysplastic Syndrome patients displayed less perforin and granzyme B secretion and higher CD95 expression. *Leuk Res, 51*, 49-55. doi:10.1016/j.leukres.2016.11.003

Tao, J. L., Li, L. J., Fu, R., Wang, H. Q., Jiang, H. J., Yue, L. Z., . . . Shao, Z. H. (2014). Elevated TIM3+ hematopoietic stem cells in untreated myelodysplastic syndrome displayed aberrant differentiation, overproliferation and decreased apoptosis. *Leuk Res, 38*(6), 714-721. doi:10.1016/j.leukres.2014.03.018

Vinh, D. C., Patel, S. Y., Uzel, G., Anderson, V. L., Freeman, A. F., Olivier, K. N., . . . Holland, S. M. (2010). Autosomal dominant and sporadic monocytopenia with susceptibility to mycobacteria, fungi, papillomaviruses, and myelodysplasia. *Blood, 115*(8), 1519-1529. doi:10.1182/blood-2009-03-208629

Viré, E., Brenner, C., Deplus, R., Blanchon, L., Fraga, M., Didelot, C., . . . Fuks, F. (2006). The Polycomb group protein EZH2 directly controls DNA methylation. *Nature, 439*(7078), 871-874. doi:10.1038/nature04431

Vulcano, M., Struyf, S., Scapini, P., Cassatella, M., Bernasconi, S., Bonecchi, R., . . . Sozzani, S. (2003). Unique regulation of CCL18 production by maturing dendritic cells. *J Immunol, 170*(7), 3843-3849. doi:10.4049/jimmunol.170.7.3843

Waclawiczek, A., Leppä, A. M., Renders, S., Stumpf, K., Reyneri, C., Betz, B., . . . Trumpp, A. (2023). Combinatorial BCL-2 family expression in Acute Myeloid Leukemia Stem Cells predicts clinical response to Azacitidine/Venetoclax. *Cancer Discov*. doi:10.1158/2159-8290.Cd-22-0939

Wang, C., Yang, Y., Gao, S., Chen, J., Yu, J., Zhang, H., . . . Li, W. (2018). Immune dysregulation in myelodysplastic syndrome: Clinical features, pathogenesis and therapeutic strategies. *Crit Rev Oncol Hematol, 122*, 123-132. doi:10.1016/j.critrevonc.2017.12.013

Wherry, E. J., Ha, S. J., Kaech, S. M., Haining, W. N., Sarkar, S., Kalia, V., . . . Ahmed, R. (2007). Molecular signature of CD8+ T cell exhaustion during chronic viral infection. *Immunity, 27*(4), 670-684. doi:10.1016/j.immuni.2007.09.006

Wilson, N. K., Foster, S. D., Wang, X., Knezevic, K., Schütte, J., Kaimakis, P., . . . Göttgens, B. (2010). Combinatorial transcriptional control in blood stem/progenitor cells: genome-wide analysis of ten major transcriptional regulators. *Cell Stem Cell, 7*(4), 532-544. doi:10.1016/j.stem.2010.07.016

Winters, A. C., Maloney, K. W., Treece, A. L., Gore, L., & Franklin, A. K. (2020). Single-center pediatric experience with venetoclax and azacitidine as treatment for myelodysplastic syndrome and acute myeloid leukemia. *Pediatr Blood Cancer, 67*(10), e28398. doi:10.1002/pbc.28398

Wlodarski, M. W., Hirabayashi, S., Pastor, V., Starý, J., Hasle, H., Masetti, R., . . . EWOG-MDS, f. t. (2016). Prevalence, clinical characteristics, and prognosis of GATA2-related myelodysplastic syndromes in children and adolescents. *Blood, 127*(11), 1387-1397. doi:10.1182/blood-2015-09-669937

Xu, F., Li, X., Wu, L., Zhang, Q., Yang, R., Yang, Y., . . . Chang, C. (2011). Overexpression of the EZH2, RING1 and BMI1 genes is common in myelodysplastic syndromes: relation to adverse epigenetic alteration and poor prognostic scoring. *Ann Hematol, 90*(6), 643-653. doi:10.1007/s00277-010-1128-5

Yi, J. S., Cox, M. A., & Zajac, A. J. (2010). T-cell exhaustion: characteristics, causes and conversion. *Immunology, 129*(4), 474-481. doi:10.1111/j.1365-2567.2010.03255.x

Zeidan, A. M., Al-Kali, A., Borate, U., Cluzeau, T., DeZern, A. E., Esteve, J., . . . Garcia-Manero, G. (2021). Sabatolimab (MBG453) Combination Treatment Regimens for Patients (Pts) with Higher-Risk Myelodysplastic Syndromes (HR-MDS): The MDS Studies in the Stimulus Immuno-Myeloid Clinical Trial Program. *Blood, 138*(Supplement 1), 4669-4669. doi:10.1182/blood-2021-145626

Zeidan, A. M., Garcia, J. S., Fenaux, P., Platzbecker, U., Miyazaki, Y., Xiao, Z.-J., . . . Garcia-Manero, G. (2021). Phase 3 VERONA study of venetoclax with azacitidine to assess change in complete remission and overall survival in treatment-naïve higher-risk myelodysplastic syndromes. *Journal of Clinical Oncology, 39*(15_suppl), TPS7054-TPS7054. doi:10.1200/JCO.2021.39.15_suppl.TPS7054

Zhang, Y., Chen, X., Gueydan, C., & Han, J. (2018). Plasma membrane changes during programmed cell deaths. *Cell Res, 28*(1), 9-21. doi:10.1038/cr.2017.133

Zheng, Z., Li, L., Li, G., Zhang, Y., Dong, C., Ren, F., . . . Ma, Y. (2021). EZH2/EHMT2 Histone Methyltransferases Inhibit the Transcription of DLX5 and Promote the Transformation of Myelodysplastic Syndrome to Acute Myeloid Leukemia. *Front Cell Dev Biol, 9*, 619795. doi:10.3389/fcell.2021.619795

Appendix A

Genes Included in the NanoString nCounter® Human PanCancer Immune Profiling Panel

Gene name	Type	ProbeID
A2M	Probe	NM_000014.4
ABCB1	Probe	NM_000927.3
ABL1	Probe	NM_005157.3
ADA	Probe	NM_000022.2
ADORA2A	Probe	NM_000675.3
AICDA	Probe	NM_020661.1
AIRE	Probe	NM_000383.2
AKT3	Probe	NM_181690.1
ALCAM	Probe	NM_001627.3
AMBP	Probe	NM_001633.3
AMICA1	Probe	NM_153206.2
ANP32B	Probe	NM_006401.2
ANXA1	Probe	NM_000700.1
APOE	Probe	NM_000041.2
APP	Probe	NM_000484.3
ARG1	Probe	NM_000045.2
ARG2	Probe	NM_001172.3
ATF1	Probe	NM_005171.2
ATF2	Probe	NM_001256090.1
ATG10	Probe	NM_001131028.1
ATG12	Probe	NM_004707.2
ATG16L1	Probe	NM_198890.2
ATG5	Probe	NM_004849.2
ATG7	Probe	NM_001136031.2
ATM	Probe	NM_000051.3
AXL	Probe	NM_021913.2
BAGE	Probe	NM_001187.1
BATF	Probe	NM_006399.3
BAX	Probe	NM_138761.3
BCL10	Probe	NM_003921.2
BCL2	Probe	NM_000657.2
BCL2L1	Probe	NM_001191.2

BCL6	Probe	NM_001706.2
BID	Probe	NM_001196.2
BIRC5	Probe	NM_001168.2
BLK	Probe	NM_001715.2
BLNK	Probe	NM_013314.2
BMI1	Probe	NM_005180.5
BST1	Probe	NM_004334.2
BST2	Probe	NM_004335.2
BTK	Probe	NM_000061.1
BTLA	Probe	NM_181780.2
C1QA	Probe	NM_015991.2
C1QB	Probe	NM_000491.3
C1QBP	Probe	NM_001212.3
C1R	Probe	NM_001733.4
C1S	Probe	NM_001734.2
C2	Probe	NM_000063.3
C3	Probe	NM_000064.2
C3AR1	Probe	NM_004054.2
C4B	Probe	NM_001002029.3
C4BPA	Probe	NM_000715.3
C5	Probe	NM_001735.2
C6	Probe	NM_000065.2
C7	Probe	NM_000587.2
C8A	Probe	NM_000562.2
C8B	Probe	NM_000066.2
C8G	Probe	NM_000606.2
C9	Probe	NM_001737.3
CAMP	Probe	NM_004345.3
CARD11	Probe	NM_032415.2
CARD9	Probe	NM_052813.4
CASP1	Probe	NM_001223.3
CASP10	Probe	NM_032977.3
CASP3	Probe	NM_032991.2
CASP8	Probe	NM_001228.4
CCL1	Probe	NM_002981.1
CCL11	Probe	NM_002986.2
CCL13	Probe	NM_005408.2
CCL14	Probe	NM_032963.3
CCL15	Probe	NM_032965.3
CCL16	Probe	NM_004590.2
CCL17	Probe	NM_002987.2

CCL18	Probe	NM_002988.2
CCL19	Probe	NM_006274.2
CCL2	Probe	NM_002982.3
CCL20	Probe	NM_004591.1
CCL21	Probe	NM_002989.2
CCL22	Probe	NM_002990.3
CCL23	Probe	NM_145898.1
CCL24	Probe	NM_002991.2
CCL25	Probe	NM_005624.2
CCL26	Probe	NM_006072.4
CCL27	Probe	NM_006664.2
CCL28	Probe	NM_148672.2
CCL3	Probe	NM_002983.2
CCL3L1	Probe	NM_021006.4
CCL4	Probe	NM_002984.2
CCL5	Probe	NM_002985.2
CCL7	Probe	NM_006273.2
CCL8	Probe	NM_005623.2
CCND3	Probe	NM_001760.2
CCR1	Probe	NM_001295.2
CCR2	Probe	NM_001123041.2
CCR3	Probe	NM_001837.2
CCR4	Probe	NM_005508.4
CCR5	Probe	NM_000579.1
CCR6	Probe	NM_031409.2
CCR7	Probe	NM_001838.2
CCR9	Probe	NM_031200.1
CCRL2	Probe	NM_003965.4
CD14	Probe	NM_000591.2
CD160	Probe	NM_007053.2
CD163	Probe	NM_004244.4
CD164	Probe	NM_006016.4
CD180	Probe	NM_005582.2
CD19	Probe	NM_001770.4
CD1A	Probe	NM_001763.2
CD1B	Probe	NM_001764.2
CD1C	Probe	NM_001765.2
CD1D	Probe	NM_001766.3
CD1E	Probe	NM_001042583.1
CD2	Probe	NM_001767.3
CD200	Probe	NM_005944.5

CD207	Probe	NM_015717.2
CD209	Probe	NM_021155.2
CD22	Probe	NM_001771.2
CD24	Probe	NM_013230.2
CD244	Probe	NM_016382.2
CD247	Probe	NM_198053.1
CD27	Probe	NM_001242.4
CD274	Probe	NM_014143.3
CD276	Probe	NM_001024736.1
CD28	Probe	NM_001243078.1
CD33	Probe	NM_001177608.1
CD34	Probe	NM_001025109.1
CD36	Probe	NM_001001548.2
CD37	Probe	NM_001774.2
CD38	Probe	NM_001775.2
CD3D	Probe	NM_000732.4
CD3E	Probe	NM_000733.2
CD3EAP	Probe	NM_012099.1
CD3G	Probe	NM_000073.2
CD4	Probe	NM_000616.4
CD40	Probe	NM_001250.4
CD40LG	Probe	NM_000074.2
CD44	Probe	NM_001001392.1
CD46	Probe	NM_172350.1
CD47	Probe	NM_001777.3
CD48	Probe	NM_001778.2
CD5	Probe	NM_014207.2
CD53	Probe	NM_001040033.1
CD55	Probe	NM_000574.3
CD58	Probe	NM_001779.2
CD59	Probe	NM_000611.4
CD6	Probe	NM_006725.3
CD63	Probe	NM_001780.4
CD68	Probe	NM_001251.2
CD7	Probe	NM_006137.6
CD70	Probe	NM_001252.2
CD74	Probe	NM_001025159.1
CD79A	Probe	NM_001783.3
CD79B	Probe	NM_021602.2
CD80	Probe	NM_005191.3
CD81	Probe	NM_004356.3

CD83	Probe	NM_004233.3
CD84	Probe	NM_001184879.1
CD86	Probe	NM_175862.3
CD8A	Probe	NM_001768.5
CD8B	Probe	NM_004931.3
CD9	Probe	NM_001769.2
CD96	Probe	NM_005816.4
CD97	Probe	NM_078481.2
CD99	Probe	NM_002414.3
CDH1	Probe	NM_004360.2
CDH5	Probe	NM_001795.3
CDK1	Probe	NM_001786.4
CDKN1A	Probe	NM_000389.2
CEACAM1	Probe	NM_001712.3
CEACAM6	Probe	NM_002483.4
CEACAM8	Probe	NM_001816.3
CEBPB	Probe	NM_005194.2
CFB	Probe	NM_001710.5
CFD	Probe	NM_001928.2
CFI	Probe	NM_000204.3
CFP	Probe	NM_002621.2
CHIT1	Probe	NM_003465.2
CHUK	Probe	NM_001278.3
CKLF	Probe	NM_181640.2
CLEC4A	Probe	NM_194448.2
CLEC4C	Probe	NM_203503.1
CLEC5A	Probe	NM_013252.2
CLEC6A	Probe	NM_001007033.1
CLEC7A	Probe	NM_197954.2
CLU	Probe	NM_001831.2
CMA1	Probe	NM_001836.2
CMKLR1	Probe	NM_004072.1
COL3A1	Probe	NM_000090.3
COLEC12	Probe	NM_130386.2
CR1	Probe	NM_000651.4
CR2	Probe	NM_001006658.1
CREB1	Probe	NM_004379.3
CREB5	Probe	NM_182898.2
CREBBP	Probe	NM_004380.2
CRP	Probe	NM_000567.2
CSF1	Probe	NM_000757.4

CSF1R	Probe	NM_005211.2
CSF2	Probe	NM_000758.2
CSF2RB	Probe	NM_000395.2
CSF3	Probe	NM_000759.3
CSF3R	Probe	NM_156038.2
CT45A1	Probe	NM_001017417.1
CTAG1B	Probe	NM_001327.2
CTAGE1	Probe	NM_172241.2
CTCFL	Probe	NM_001269042.1
CTLA4	Probe	NM_005214.3
CTSG	Probe	NM_001911.2
CTSH	Probe	NM_004390.3
CTSL	Probe	NM_001912.4
CTSS	Probe	NM_004079.3
CTSW	Probe	NM_001335.3
CX3CL1	Probe	NM_002996.3
CX3CR1	Probe	NM_001337.3
CXCL1	Probe	NM_001511.1
CXCL10	Probe	NM_001565.1
CXCL11	Probe	NM_005409.4
CXCL12	Probe	NM_000609.5
CXCL13	Probe	NM_006419.2
CXCL14	Probe	NM_004887.4
CXCL16	Probe	NM_001100812.1
CXCL2	Probe	NM_002089.3
CXCL3	Probe	NM_002090.2
CXCL5	Probe	NM_002994.3
CXCL6	Probe	NM_002993.3
CXCL9	Probe	NM_002416.1
CXCR1	Probe	NM_000634.2
CXCR2	Probe	NM_001557.2
CXCR3	Probe	NM_001504.1
CXCR4	Probe	NM_003467.2
CXCR5	Probe	NM_001716.3
CXCR6	Probe	NM_006564.1
CYBB	Probe	NM_000397.3
CYFIP2	Probe	NM_001037332.2
CYLD	Probe	NM_015247.1
DDX43	Probe	NM_018665.2
DDX58	Probe	NM_014314.3
DEFB1	Probe	NM_005218.3

DMBT1	Probe	NM_007329.2
DOCK9	Probe	NM_001130048.1
DPP4	Probe	NM_001935.3
DUSP4	Probe	NM_057158.2
DUSP6	Probe	NM_001946.2
EBI3	Probe	NM_005755.2
ECSIT	Probe	NM_001142464.2
EGR1	Probe	NM_001964.2
EGR2	Probe	NM_000399.3
ELANE	Probe	NM_001972.2
ELK1	Probe	NM_005229.3
ENG	Probe	NM_001114753.1
ENTPD1	Probe	NM_001098175.1
EOMES	Probe	NM_005442.2
EP300	Probe	NM_001429.2
EPCAM	Probe	NM_002354.1
ETS1	Probe	NM_005238.3
EWSR1	Probe	NM_013986.3
F12	Probe	NM_000505.3
F13A1	Probe	NM_000129.3
F2RL1	Probe	NM_005242.3
FADD	Probe	NM_003824.2
FAS	Probe	NM_000043.3
FCER1A	Probe	NM_002001.2
FCER1G	Probe	NM_004106.1
FCER2	Probe	NM_002002.4
FCGR1A	Probe	NM_000566.3
FCGR2A	Probe	NM_021642.3
FCGR2B	Probe	NM_001002273.1
FCGR3A	Probe	NM_000569.6
FEZ1	Probe	NM_005103.4
FLT3	Probe	NM_004119.1
FLT3LG	Probe	NM_001459.3
FN1	Probe	NM_212482.1
FOS	Probe	NM_005252.2
FOXJ1	Probe	NM_001454.3
FOXP3	Probe	NM_014009.3
FPR2	Probe	NM_001462.3
FUT5	Probe	NM_002034.2
FUT7	Probe	NM_004479.3
FYN	Probe	NM_002037.3

GAGE1	Probe	NM_001040663.2
GATA3	Probe	NM_001002295.1
GNLY	Probe	NM_006433.2
GPI	Probe	NM_000175.2
GTF3C1	Probe	NM_001520.3
GZMA	Probe	NM_006144.2
GZMB	Probe	NM_004131.3
GZMH	Probe	NM_033423.3
GZMK	Probe	NM_002104.2
GZMM	Probe	NM_005317.2
HAMP	Probe	NM_021175.2
HAVCR2	Probe	NM_032782.3
HCK	Probe	NM_002110.2
HLA-A	Probe	NM_002116.5
HLA-B	Probe	NM_005514.6
HLA-C	Probe	NM_002117.4
HLA-DMA	Probe	NM_006120.3
HLA-DMB	Probe	NM_002118.3
HLA-DOB	Probe	NM_002120.3
HLA-DPA1	Probe	NM_033554.2
HLA-DPB1	Probe	NM_002121.4
HLA-DQA1	Probe	NM_002122.3
HLA-DQB1	Probe	NM_002123.3
HLA-DRA	Probe	NM_019111.3
HLA-DRB3	Probe	NM_022555.3
HLA-DRB4	Probe	NM_021983.4
HLA-E	Probe	NM_005516.4
HLA-G	Probe	NM_002127.4
HMGB1	Probe	NM_002128.4
HRAS	Probe	NM_005343.2
HSD11B1	Probe	NM_181755.1
ICAM1	Probe	NM_000201.2
ICAM2	Probe	NM_000873.3
ICAM3	Probe	NM_002162.3
ICAM4	Probe	NM_001039132.1
ICOS	Probe	NM_012092.2
ICOSLG	Probe	NM_015259.4
IDO1	Probe	NM_002164.3
IFI16	Probe	NM_005531.1
IFI27	Probe	NM_005532.3
IFI35	Probe	NM_005533.3

IFIH1	Probe	NM_022168.2
IFIT1	Probe	NM_001548.3
IFIT2	Probe	NM_001547.4
IFITM1	Probe	NM_003641.3
IFITM2	Probe	NM_006435.2
IFNA1	Probe	NM_024013.1
IFNA17	Probe	NM_021268.2
IFNA2	Probe	NM_000605.3
IFNA7	Probe	NM_021057.2
IFNA8	Probe	NM_002170.3
IFNAR1	Probe	NM_000629.2
IFNAR2	Probe	NM_000874.3
IFNB1	Probe	NM_002176.2
IFNG	Probe	NM_000619.2
IFNGR1	Probe	NM_000416.1
IFNL1	Probe	NM_172140.1
IFNL2	Probe	NM_172138.1
IGF1R	Probe	NM_000875.2
IGF2R	Probe	NM_000876.1
IGLL1	Probe	NM_020070.2
IKBKB	Probe	NM_001556.1
IKBKE	Probe	NM_014002.2
IKBKG	Probe	NM_003639.2
IL10	Probe	NM_000572.2
IL10RA	Probe	NM_001558.2
IL11	Probe	NM_000641.2
IL11RA	Probe	NM_147162.1
IL12A	Probe	NM_000882.2
IL12B	Probe	NM_002187.2
IL12RB1	Probe	NM_005535.1
IL12RB2	Probe	NM_001559.2
IL13	Probe	NM_002188.2
IL13RA1	Probe	NM_001560.2
IL13RA2	Probe	NM_000640.2
IL15	Probe	NM_172174.1
IL15RA	Probe	NM_002189.2
IL16	Probe	NM_004513.4
IL17A	Probe	NM_002190.2
IL17B	Probe	NM_014443.2
IL17F	Probe	NM_052872.3
IL17RA	Probe	NM_014339.6

IL17RB	Probe	NM_018725.3
IL18	Probe	NM_001562.2
IL18R1	Probe	NM_003855.2
IL18RAP	Probe	NM_003853.2
IL19	Probe	NM_013371.3
IL1A	Probe	NM_000575.3
IL1B	Probe	NM_000576.2
IL1R1	Probe	NM_000877.2
IL1R2	Probe	NM_173343.1
IL1RAP	Probe	NM_002182.2
IL1RAPL2	Probe	NM_017416.1
IL1RL1	Probe	NM_016232.4
IL1RL2	Probe	NM_003854.2
IL1RN	Probe	NM_000577.3
IL2	Probe	NM_000586.2
IL21	Probe	NM_021803.2
IL21R	Probe	NM_021798.2
IL22	Probe	NM_020525.4
IL22RA1	Probe	NM_021258.2
IL22RA2	Probe	NM_181310.1
IL23A	Probe	NM_016584.2
IL23R	Probe	NM_144701.2
IL24	Probe	NM_181339.1
IL25	Probe	NM_022789.2
IL26	Probe	NM_018402.1
IL27	Probe	NM_145659.3
IL2RA	Probe	NM_000417.1
IL2RB	Probe	NM_000878.2
IL2RG	Probe	NM_000206.1
IL3	Probe	NM_000588.3
IL32	Probe	NM_004221.4
IL34	Probe	NM_152456.1
IL3RA	Probe	NM_002183.2
IL4	Probe	NM_000589.2
IL4R	Probe	NM_000418.2
IL5	Probe	NM_000879.2
IL5RA	Probe	NM_000564.3
IL6	Probe	NM_000600.1
IL6R	Probe	NM_000565.2
IL6ST	Probe	NM_002184.2
IL7	Probe	NM_000880.2

IL7R	Probe	NM_002185.2
IL8	Probe	NM_000584.2
IL9	Probe	NM_000590.1
ILF3	Probe	NM_001137673.1
INPP5D	Probe	NM_005541.3
IRAK1	Probe	NM_001569.3
IRAK2	Probe	NM_001570.3
IRAK4	Probe	NM_016123.1
IRF1	Probe	NM_002198.1
IRF2	Probe	NM_002199.3
IRF3	Probe	NM_001571.5
IRF4	Probe	NM_002460.1
IRF5	Probe	NM_002200.3
IRF7	Probe	NM_001572.3
IRF8	Probe	NM_002163.2
IRGM	Probe	NM_001145805.1
ISG15	Probe	NM_005101.3
ISG20	Probe	NM_002201.4
ITCH	Probe	NM_001257138.1
ITGA1	Probe	NM_181501.1
ITGA2	Probe	NM_002203.2
ITGA2B	Probe	NM_000419.3
ITGA4	Probe	NM_000885.4
ITGA5	Probe	NM_002205.2
ITGA6	Probe	NM_000210.1
ITGAE	Probe	NM_002208.4
ITGAL	Probe	NM_002209.2
ITGAM	Probe	NM_000632.3
ITGAX	Probe	NM_000887.3
ITGB1	Probe	NM_033666.2
ITGB2	Probe	NM_000211.2
ITGB3	Probe	NM_000212.2
ITGB4	Probe	NM_001005731.1
ITK	Probe	NM_005546.3
JAK1	Probe	NM_002227.1
JAK2	Probe	NM_004972.2
JAK3	Probe	NM_000215.2
JAM3	Probe	NM_032801.3
KIR_Activating_Subgroup_1	Probe	NM_001083539.1
KIR_Activating_Subgroup_2	Probe	NM_014512.1
KIR_Inhibiting_Subgroup_1	Probe	NM_014218.2

KIR_Inhibiting_Subgroup_2	Probe	NM_014511.3
KIR3DL1	Probe	NM_013289.2
KIR3DL2	Probe	NM_006737.2
KIR3DL3	Probe	NM_153443.3
KIT	Probe	NM_000222.2
KLRB1	Probe	NM_002258.2
KLRC1	Probe	NM_002259.3
KLRC2	Probe	NM_002260.3
KLRD1	Probe	NM_002262.3
KLRF1	Probe	NM_016523.1
KLRG1	Probe	NM_005810.3
KLRK1	Probe	NM_007360.3
LAG3	Probe	NM_002286.5
LAIR2	Probe	NM_002288.3
LAMP1	Probe	NM_005561.3
LAMP2	Probe	NM_001122606.1
LAMP3	Probe	NM_014398.3
LBP	Probe	NM_004139.2
LCK	Probe	NM_005356.2
LCN2	Probe	NM_005564.3
LCP1	Probe	NM_002298.4
LGALS3	Probe	NM_001177388.1
LIF	Probe	NM_002309.3
LILRA1	Probe	NM_006863.1
LILRA4	Probe	NM_012276.3
LILRA5	Probe	NM_181879.2
LILRB1	Probe	NM_001081637.1
LILRB2	Probe	NM_005874.1
LILRB3	Probe	NM_006864.2
LRP1	Probe	NM_002332.2
LRRN3	Probe	NM_001099660.1
LTA	Probe	NM_000595.2
LTB	Probe	NM_002341.1
LTBR	Probe	NM_002342.1
LTF	Probe	NM_002343.2
LTK	Probe	NM_001135685.1
LY86	Probe	NM_004271.3
LY9	Probe	NM_001033667.1
LY96	Probe	NM_015364.2
LYN	Probe	NM_002350.1
MAF	Probe	NM_005360.4

MAGEA1	Probe	NM_004988.4
MAGEA12	Probe	NM_001166386.1
MAGEA3	Probe	NM_005362.3
MAGEA4	Probe	NM_001011548.1
MAGEB2	Probe	NM_002364.4
MAGEC1	Probe	NM_005462.4
MAGEC2	Probe	NM_016249.3
MAP2K1	Probe	NM_002755.2
MAP2K2	Probe	NM_030662.2
MAP2K4	Probe	NM_003010.2
MAP3K1	Probe	NM_005921.1
MAP3K5	Probe	NM_005923.3
MAP3K7	Probe	NM_145333.1
MAP4K2	Probe	NM_004579.2
MAPK1	Probe	NM_138957.2
MAPK11	Probe	NM_002751.5
MAPK14	Probe	NM_001315.1
MAPK3	Probe	NM_001040056.1
MAPK8	Probe	NM_002750.2
MAPKAPK2	Probe	NM_004759.3
MARCO	Probe	NM_006770.3
MASP1	Probe	NM_139125.3
MASP2	Probe	NM_139208.1
MAVS	Probe	NM_020746.3
MBL2	Probe	NM_000242.2
MCAM	Probe	NM_006500.2
MEF2C	Probe	NM_002397.3
MEFV	Probe	NM_000243.2
MERTK	Probe	NM_006343.2
MFGE8	Probe	NM_001114614.1
MICA	Probe	NM_000247.1
MICB	Probe	NM_005931.3
MIF	Probe	NM_002415.1
MME	Probe	NM_000902.2
MNX1	Probe	NM_005515.3
MPPED1	Probe	NM_001044370.1
MR1	Probe	NM_001531.2
MRC1	Probe	NM_002438.2
MS4A1	Probe	NM_152866.2
MS4A2	Probe	NM_000139.3
MSR1	Probe	NM_002445.3

MST1R	Probe	NM_002447.1
MUC1	Probe	NM_001018017.1
MX1	Probe	NM_002462.2
MYD88	Probe	NM_002468.3
NCAM1	Probe	NM_000615.5
NCF4	Probe	NM_000631.4
NCR1	Probe	NM_004829.5
NEFL	Probe	NM_006158.3
NFATC1	Probe	NM_172389.1
NFATC2	Probe	NM_012340.3
NFATC3	Probe	NM_004555.2
NFATC4	Probe	NM_001136022.2
NFKB1	Probe	NM_003998.2
NFKB2	Probe	NM_002502.2
NFKBIA	Probe	NM_020529.1
NLRC5	Probe	NM_032206.4
NLRP3	Probe	NM_001079821.2
NOD1	Probe	NM_006092.1
NOD2	Probe	NM_022162.1
NOS2A	Probe	NM_153292.1
NOTCH1	Probe	NM_017617.3
NRP1	Probe	NM_003873.5
NT5E	Probe	NM_002526.2
NUP107	Probe	NM_020401.2
OAS3	Probe	NM_006187.2
OSM	Probe	NM_020530.4
PASD1	Probe	NM_173493.2
PAX5	Probe	NM_016734.1
PBK	Probe	NM_018492.2
PDCD1	Probe	NM_005018.1
PDCD1LG2	Probe	NM_025239.3
PDGFC	Probe	NM_016205.2
PDGFRB	Probe	NM_002609.3
PECAM1	Probe	NM_000442.3
PIK3CD	Probe	NM_005026.3
PIK3CG	Probe	NM_002649.2
PIN1	Probe	NM_006221.2
PLA2G1B	Probe	NM_000928.2
PLA2G6	Probe	NM_001004426.1
PLAU	Probe	NM_002658.2
PLAUR	Probe	NM_001005376.1

PMCH	Probe	NM_002674.2
PNMA1	Probe	NM_006029.4
POU2AF1	Probe	NM_006235.2
POU2F2	Probe	NM_002698.2
PPARG	Probe	NM_015869.3
PPBP	Probe	NM_002704.2
PRAME	Probe	NM_006115.3
PRF1	Probe	NM_005041.3
PRG2	Probe	NM_002728.4
PRKCD	Probe	NM_006254.3
PRKCE	Probe	NM_005400.2
PRM1	Probe	NM_002761.2
PSEN1	Probe	NM_000021.2
PSEN2	Probe	NM_000447.2
PSMB10	Probe	NM_002801.2
PSMB7	Probe	NM_002799.2
PSMB8	Probe	NM_004159.4
PSMB9	Probe	NM_002800.4
PSMD7	Probe	NM_002811.3
PTGDR2	Probe	NM_004778.1
PTGS2	Probe	NM_000963.1
PTPRC	Probe	NM_080921.3
PVR	Probe	NM_006505.3
PYCARD	Probe	NM_013258.3
RAG1	Probe	NM_000448.2
REL	Probe	NM_002908.2
RELA	Probe	NM_021975.2
RELB	Probe	NM_006509.2
REPS1	Probe	NM_001128617.2
RIPK2	Probe	NM_003821.5
ROPN1	Probe	NM_017578.2
RORA	Probe	NM_134261.2
RORC	Probe	NM_001001523.1
RPS6	Probe	NM_001010.2
RRAD	Probe	NM_004165.1
RUNX1	Probe	NM_001754.4
RUNX3	Probe	NM_004350.1
S100A12	Probe	NM_005621.1
S100A7	Probe	NM_002963.2
S100A8	Probe	NM_002964.3
S100B	Probe	NM_006272.1

SAA1	Probe	NM_199161.1
SBNO2	Probe	NM_014963.2
SELE	Probe	NM_000450.2
SELL	Probe	NR_029467.1
SELPLG	Probe	NM_001206609.1
SEMG1	Probe	NM_003007.2
SERPINB2	Probe	NM_002575.1
SERPING1	Probe	NM_000062.2
SH2B2	Probe	NM_020979.3
SH2D1A	Probe	NM_001114937.2
SH2D1B	Probe	NM_053282.4
SIGIRR	Probe	NM_021805.2
SIGLEC1	Probe	NM_023068.3
SLAMF1	Probe	NM_003037.2
SLAMF6	Probe	NM_001184714.1
SLAMF7	Probe	NM_021181.3
SLC11A1	Probe	NM_000578.2
SMAD2	Probe	NM_005901.5
SMAD3	Probe	NM_005902.3
SMPD3	Probe	NM_018667.3
SOCS1	Probe	NM_003745.1
SPA17	Probe	NM_017425.3
SPACA3	Probe	NM_173847.3
SPANXB1	Probe	NM_032461.2
SPINK5	Probe	NM_006846.3
SPN	Probe	NM_003123.3
SPO11	Probe	NM_198265.1
SPP1	Probe	NM_000582.2
SSX1	Probe	NM_005635.2
SSX4	Probe	NM_005636.3
ST6GAL1	Probe	NM_003032.2
STAT1	Probe	NM_007315.2
STAT2	Probe	NM_005419.2
STAT3	Probe	NM_139276.2
STAT4	Probe	NM_003151.2
STAT5B	Probe	NM_012448.3
STAT6	Probe	NM_003153.3
SYCP1	Probe	NM_003176.2
SYK	Probe	NM_003177.3
SYT17	Probe	NM_016524.2
TAB1	Probe	NM_153497.2

TAL1	Probe	NM_003189.2
TANK	Probe	NM_004180.2
TAP1	Probe	NM_000593.5
TAP2	Probe	NM_000544.3
TAPBP	Probe	NM_003190.4
TARP	Probe	NM_001003799.1
TBK1	Probe	NM_013254.2
TBX21	Probe	NM_013351.1
TCF7	Probe	NM_003202.2
TFE3	Probe	NM_006521.3
TFEB	Probe	NM_007162.2
TFRC	Probe	NM_003234.1
TGFB1	Probe	NM_000660.3
TGFB2	Probe	NM_003238.2
THBD	Probe	NM_000361.2
THBS1	Probe	NM_003246.2
THY1	Probe	NM_006288.2
TICAM1	Probe	NM_014261.1
TICAM2	Probe	NM_021649.4
TIGIT	Probe	NM_173799.2
TIRAP	Probe	NM_148910.2
TLR1	Probe	NM_003263.3
TLR10	Probe	NM_030956.2
TLR2	Probe	NM_003264.3
TLR3	Probe	NM_003265.2
TLR4	Probe	NM_138554.2
TLR5	Probe	NM_003268.3
TLR6	Probe	NM_006068.2
TLR7	Probe	NM_016562.3
TLR8	Probe	NM_016610.2
TLR9	Probe	NM_017442.2
TMEFF2	Probe	NM_016192.2
TNF	Probe	NM_000594.2
TNFAIP3	Probe	NM_006290.2
TNFRSF10B	Probe	NM_003842.3
TNFRSF10C	Probe	NM_003841.3
TNFRSF11A	Probe	NM_003839.2
TNFRSF11B	Probe	NM_002546.2
TNFRSF12A	Probe	NM_016639.1
TNFRSF13B	Probe	NM_012452.2
TNFRSF13C	Probe	NM_052945.3

TNFRSF14	Probe	NM_003820.2
TNFRSF17	Probe	NM_001192.2
TNFRSF18	Probe	NM_004195.2
TNFRSF1A	Probe	NM_001065.2
TNFRSF1B	Probe	NM_001066.2
TNFRSF4	Probe	NM_003327.2
TNFRSF8	Probe	NM_152942.2
TNFRSF9	Probe	NM_001561.4
TNFSF10	Probe	NM_003810.2
TNFSF11	Probe	NM_003701.2
TNFSF12	Probe	NM_003809.2
TNFSF13	Probe	NM_003808.3
TNFSF13B	Probe	NM_006573.4
TNFSF14	Probe	NM_003807.3
TNFSF15	Probe	NM_001204344.1
TNFSF18	Probe	NM_005092.2
TNFSF4	Probe	NM_003326.2
TNFSF8	Probe	NM_001244.3
TOLLIP	Probe	NM_019009.2
TP53	Probe	NM_000546.2
TPSAB1	Probe	NM_003294.3
TPTE	Probe	NM_199259.2
TRAF2	Probe	NM_021138.3
TRAF3	Probe	NM_145725.1
TRAF6	Probe	NM_145803.1
TREM1	Probe	NM_018643.3
TREM2	Probe	NM_018965.3
TTK	Probe	NM_003318.3
TXK	Probe	NM_003328.1
TXNIP	Probe	NM_006472.1
TYK2	Probe	NM_003331.3
UBC	Probe	NM_021009.3
ULBP2	Probe	NM_025217.2
USP9Y	Probe	NM_004654.3
VCAM1	Probe	NM_001078.3
VEGFA	Probe	NM_001025366.1
VEGFC	Probe	NM_005429.2
XCL2	Probe	NM_003175.3
XCR1	Probe	NM_005283.2
YTHDF2	Probe	NM_001172828.1
ZAP70	Probe	NM_001079.3

ZNF205	Probe	NM_001031686.1
ABCF1	Internal Reference	NM_001090.2
AGK	Internal Reference	NM_018238.3
ALAS1	Internal Reference	NM_000688.4
AMMECR1L	Internal Reference	NM_001199140.1
CC2D1B	Internal Reference	NM_032449.2
CNOT10	Internal Reference	NM_001256741.1
CNOT4	Internal Reference	NM_001190848.1
COG7	Internal Reference	NM_153603.3
DDX50	Internal Reference	NM_024045.1
DHX16	Internal Reference	NM_001164239.1
DNAJC14	Internal Reference	NM_032364.5
EDC3	Internal Reference	NM_001142443.1
EIF2B4	Internal Reference	NM_172195.3
ERCC3	Internal Reference	NM_000122.1
FCF1	Internal Reference	NM_015962.4
G6PD	Internal Reference	NM_000402.2
GPATCH3	Internal Reference	NM_022078.2
GUSB	Internal Reference	NM_000181.1
HDAC3	Internal Reference	NM_003883.2
HPRT1	Internal Reference	NM_000194.1
MRPS5	Internal Reference	NM_031902.3
MTMR14	Internal Reference	NM_022485.3
NOL7	Internal Reference	NM_016167.3
NUBP1	Internal Reference	NM_001278506.1
POLR2A	Internal Reference	NM_000937.2
PPIA	Internal Reference	NM_021130.2
PRPF38A	Internal Reference	NM_032864.3
SAP130	Internal Reference	NM_024545.3
SDHA	Internal Reference	NM_004168.1
SF3A3	Internal Reference	NM_006802.2
TBP	Internal Reference	NM_001172085.1
TLK2	Internal Reference	NM_006852.2
TMUB2	Internal Reference	NM_024107.2
TRIM39	Internal Reference	NM_021253.3
TUBB	Internal Reference	NM_178014.2
USP39	Internal Reference	NM_001256725.1
ZC3H14	Internal Reference	NM_001160103.1
ZKSCAN5	Internal Reference	NM_014569.3
ZNF143	Internal Reference	NM_003442.5
ZNF346	Internal Reference	NM_012279.2

Appendix B

Detailed Mutational Data of Pediatric Patients with GATA2 Deficiency

Patient ID	Sex	Age at onset (years)	MDS subtype, GATA2^{mut}	Genotype		Karyo-type
D722	M	12	RCC	c.981G>A	p.G327G	normal
D801	M	18	RCC	c.1187G>A	p.R396Q	+8
D807	M	15	RCC	c.1018-10_1037del30		normal
D1010	M	13	RCC	c.1128C>G	p.Y376X	normal
D1072	F	17	RCC	c.1143+1G>A		-7
D1119	F	16	RCC	c.1084C>T	p.R362*	+8
D1140	M	13	RCC	c.1045T>A	p.C349S	+8
D1141	M	17	RCC	c.1045T>A	p.C349S	normal
D1144	F	12	RCC	c.1037_1046 del	p.G346Vfs*38	+8
D1239	F	13	RCC	c.351C>G	p.T117T	-7
D1372	F	10	RCC	c. 1061C>T	p.T354M	normal
D1428	M	17	RCC	c.1109G>T	p.C370F	+8
D1443	M	10	RCC	c.341delA	p.N114Tfs*5	-7
D1504	M	4	RCC	c.1084C>T	p.R362*	-7
I305	M	18	RCC	c.161C>A	p.S54X	-7
I306	M	13	RCC	c.1186C>T	p.R396W	normal
I312	M	10	RCC	c.414_417del CTCT	p.S139CfsX78	normal
I359	F	16	RCC	c.1084C>T	p.R362fsx*	normal
I377	F	20	RCC	unknown		+8
	F	19	RCC	unknown		+8
I391	M	8	RCC	c.1215G>T	p.K405N	normal

D770	F	11	MDS-EB	C599delG	p.G200VfsX18	-7
D1064	F	7	MDS-EB	c.1113C>A	p.N371K	-7
D1302	M	15	MDS-EB	c.599dupG	p.S201*	-7
D1319	F	16	MDS-EB	c.303delC	p.A103Qfs*16	-7
D1521	M	12	MDS-EB	c.416_417delCT	p.S139Cfs-Ter45	-7
D1542	F	10	MDS-EB	c.448G>T	p.G150*	-7

-7: Monosomy 7; +8: Trisomy 8; F: female; M: male

Detailed mutational data lacking for n=3 patients in the GATA2-RCC group

Appendix C

Detailed Overview of mIF Panels and IHC Markers

Table C 1: Overview of mIF panels and their composition.

Target	Characteristic for	Opal	Filter	Dilution	Antigen retrieval
Panel A					
MPO	Myeloid cells	620	Texas Red	1:100	None
MCT	Mast cells	690	Cy5	1:200	AR6
CD34	Hematopoietic progenitor cells	650	Cy5	1:100	AR6
TdT	Hematogonic cells	540	Cy3	1:50	AR9
Panel B					
CD42b	Megakaryocytes	690	Cy5	1:100	AR9
CD123	Dendritic cells	620	Texas Red	1:50	AR9
CD3	T lymphocytes	570	Cy3	1:150	AR9
CD14	Monocytes	650	Cy5	1:100	AR6
Panel C					
CD34	Hematopoietic progenitor cells	570	DAPI/ 570/690	1:100	AR6
H3K27me3	Trimethylation of Lysine 27, Histone H3	520	520	1:100	AR9
Panel D					
CD8	Cytotoxic T lymphocytes	520	520	1:150	AR9
BCL2	Regulation of apoptosis	570	DAPI/ 570/690	1:25	AR9
Panel E					
EPX	Eosinophilic granulocytes	690	DAPI/ 570/690	1:180	TRS6

BCL2	Regulation of apoptosis	570	DAPI/ 570/690	1:25	CC1
CD71	Erythrocytes	520	520	1:400	CC1
CD14	Monocytes	780	480/620/ 780	1:100	AR6
Panel F					
MPO	Myeloid cells	620	480/620/ 780	1:100	None
CD34	Hematopoietic progenitor cells	690	DAPI/ 570/690	1:100	AR6
CD3	T lymphocytes	520	520	1:150	AR9
BCL2	Regulation of apoptosis	570	DAPI/ 570/690	1:25	CC1
MCT	Mast cells	780	480/620/ 780	1:200	AR6
Panel G					
Bcl-XL	Regulation of Apoptosis	520	520	1:75	AR9
BCL2	Regulation of Apoptosis	570	DAPI/ 570/690	1:25	CC1
MCL1	Regulation of Apoptosis	690	DAPI/ 570/690	1:75	AR6
Panel H					
CASP1	Pyroptosis	620	Texas Red	1:50	ProTaqs I
NLRP3	Pyroptosis	570	Cy3	1:200	TRS6
CASP3	Apoptosis	650	Cy5	1:50	AR9
PLIN1	Adipose tissue	540	Cy3	1:150	AR6
S100A9	Pyroptosis	690	Cy5	1:300	AR6
Panel I					
PD-1	Exhausted T lymphocytes	520	520	1:80	TRS6
CD8	Cytotoxic T lymphocytes	690	DAPI/ 570/690	1:150	AR9

FOXP3	Regulatory T lymphocytes	620	480/620/ 780	1:50	TRS6
BCL2	Regulation of Apoptosis	570	DAPI/ 570/690	1:25	CC1
TIM-3	Exhausted T lymphocytes	780	480/620/ 780	1:200	AR9
Panel J					
CD3	T lymphocytes	690	DAPI/ 570/690	1:150	AR9
TIM-3	Exhausted T lymphocytes	620	480/620/ 780	1:200	AR9
CD163	Macrophages	570	DAPI/ 570/690	1:150	AR9
MCT	Mast cells	780	480/620/ 780	1:200	AR6
Panel K					
MPO	Myeloid cells	690	DAPI/ 570/690	1:400	None
CD14	Monocytes	570	DAPI/ 570/690	1:100	AR6
TIM-3	Exhausted T lymphocytes	780	480/620/ 780	1:200	AR9
Panel L					
MPO	Myeloid cells	520	520	1:100	TRS6
SCF	Growth factor in hematopoiesis	690	DAPI/ 570/690	1:50	AR6
CD117	Myeloid progenitors	570	DAPI/ 570/690	1:100	AR6
CCL18	C-C motif chemokine ligand 18	780	480/620/ 780	1:75	TRS6
Panel M					
MPO	Myeloid cells	520	520	1:100	TRS6

SCF	Growth factor in hematopoiesis	690	DAPI/ 570/690	1:50	AR6
CD34	Hematopoietic progenitor cells	570	DAPI/ 570/690	1:100	AR6
CCL18	C-C motif chemokine ligand 18	780	480/620/ 780	1:75	TRS6

Table C 2: Overview of IHC marker.

Target	Characteristic for	Chromogen	Dilution	Antigen retrieval
Cleaved CASP1	Pyroptosis	DAB	1:200	ProTaqs I
CCL18	C-C motif chemokine ligand 18	DAB	1:125	TRS6
CD20	B lymphocytes	DAB	1:400	CC1
EPX	Eosinophilic granulocytes	DAB	1:180	TRS6
Cleaved GSDMD	Pyroptosis	DAB	1:200	AR9
H3K27me3	Trimethylation of Lysine 27, Histone H3	DAB	1:4000	AR9
Ki-67	Proliferating cells	DAB	1:100	CC1

Appendix D

Analysis of the Influence of Monosomy 7 on Expression Profiles of Distinct Cell Populations within the Bone Marrow

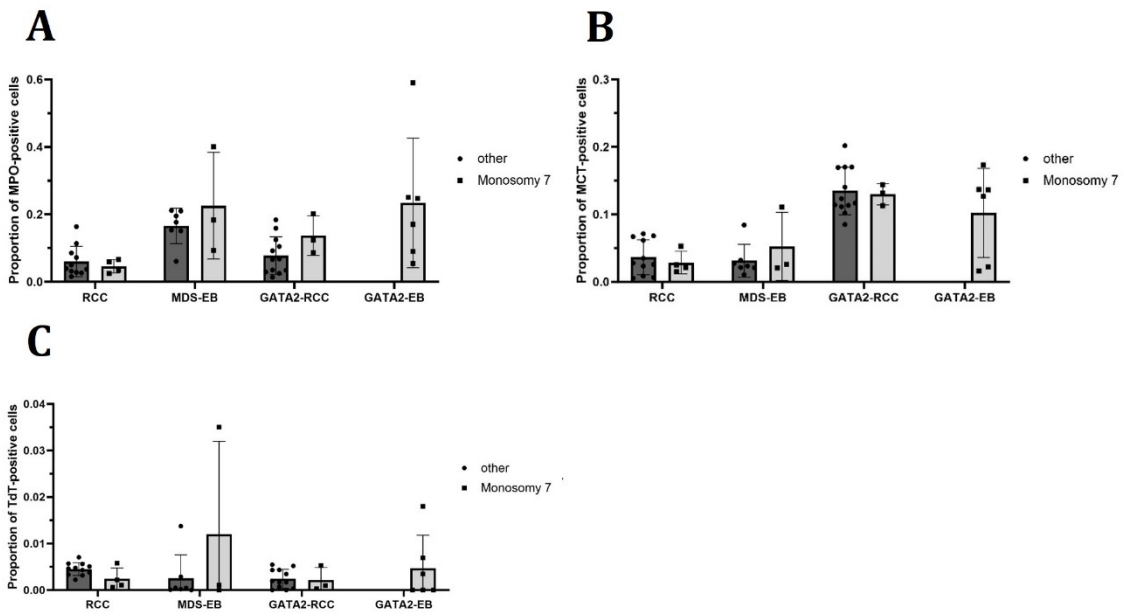

Figure D 1: Distribution of myeloid cells, mast cells, and hematogonic cells within the bone marrow. Cell quantification is presented for myeloid cells (MPO) **(A)**, mast cells (MCT) **(B)**, and hematogonic cells (TdT) **(C)** in patients with refractory cytopenia of childhood (RCC) and myelodysplastic syndrome with excess blasts (MDS-EB), and patients with additional *GATA2* mutation (GATA2-RCC; GATA2-EB). Monosomy 7 is compared to other karyotypes present in the cohort, including trisomy 8, normal karyotype, and random aberrations.

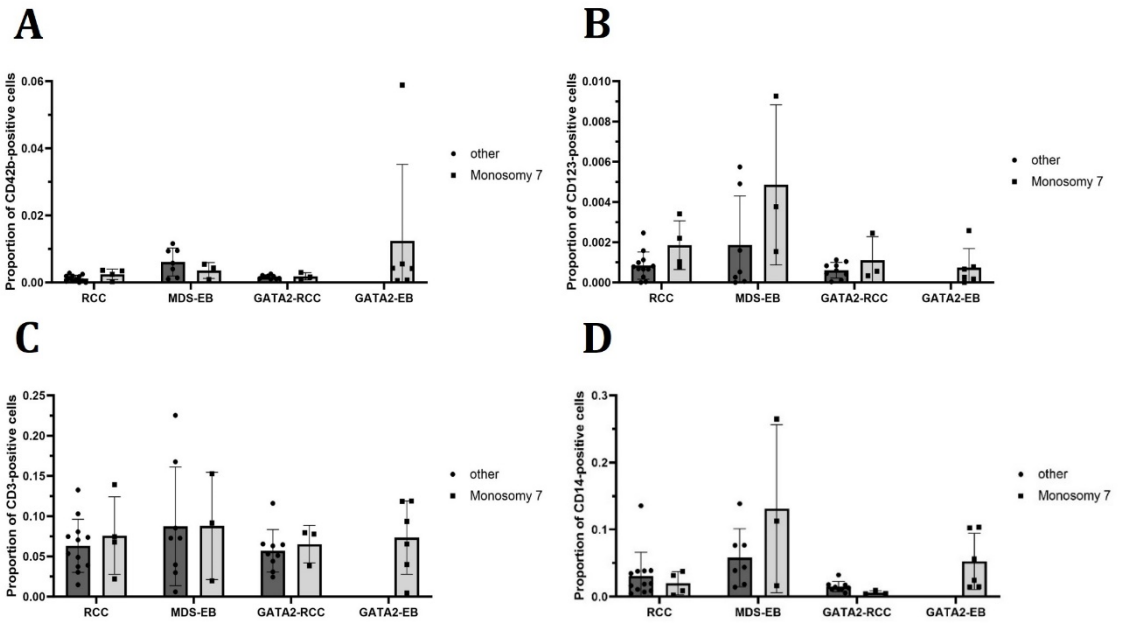

Figure D 2: Distribution of megakaryocytes, dendritic cells, T lymphocytes, and monocytes with respect to karyotypic differences. Proportion of megakaryocytes (CD42b) **(A)**, dendritic cells (CD123) **(B)**, T lymphocytes (CD3) **(C)**, and monocytes (CD14) **(D)** in patients with monosomy 7 compared to those with other karyotypes.

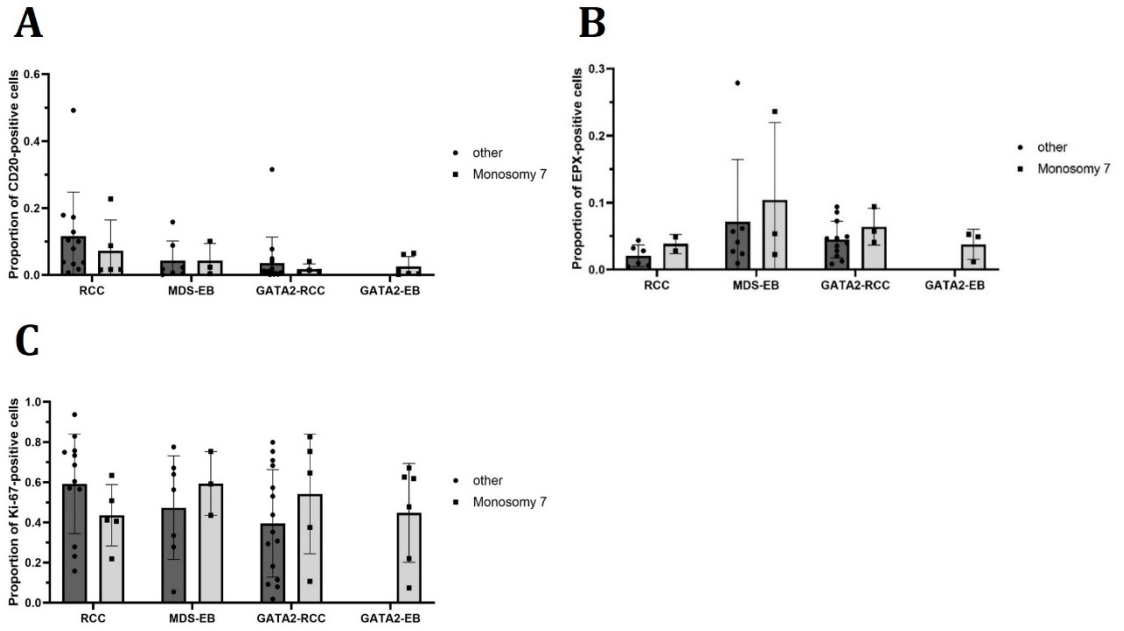

Figure D 3: Distribution of B lymphocytes, eosinophilic granulocytes, and proliferating cells. Quantification of B lymphocytes (CD20) **(A)**, eosinophilic granulocytes (EPX) **(B)**, and proliferating cells (Ki-67) **(C)**, specifically comparing monosomy 7 to alternate karyotypes.

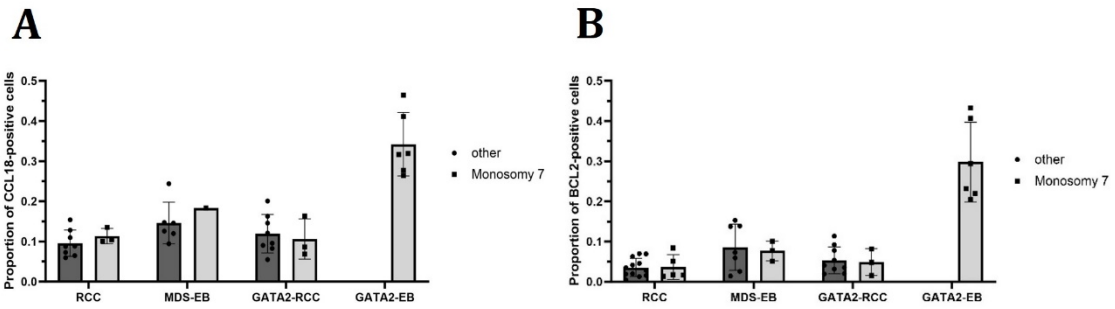

Figure D 4: Protein expression profiles for CCL18 and BCL2, illustrating karyotypic differences. Proportion of cells positive for CCL18 **(A)**, and BCL2 **(B)**, specifically comparing the impact of monosomy 7 versus different karyotypes.

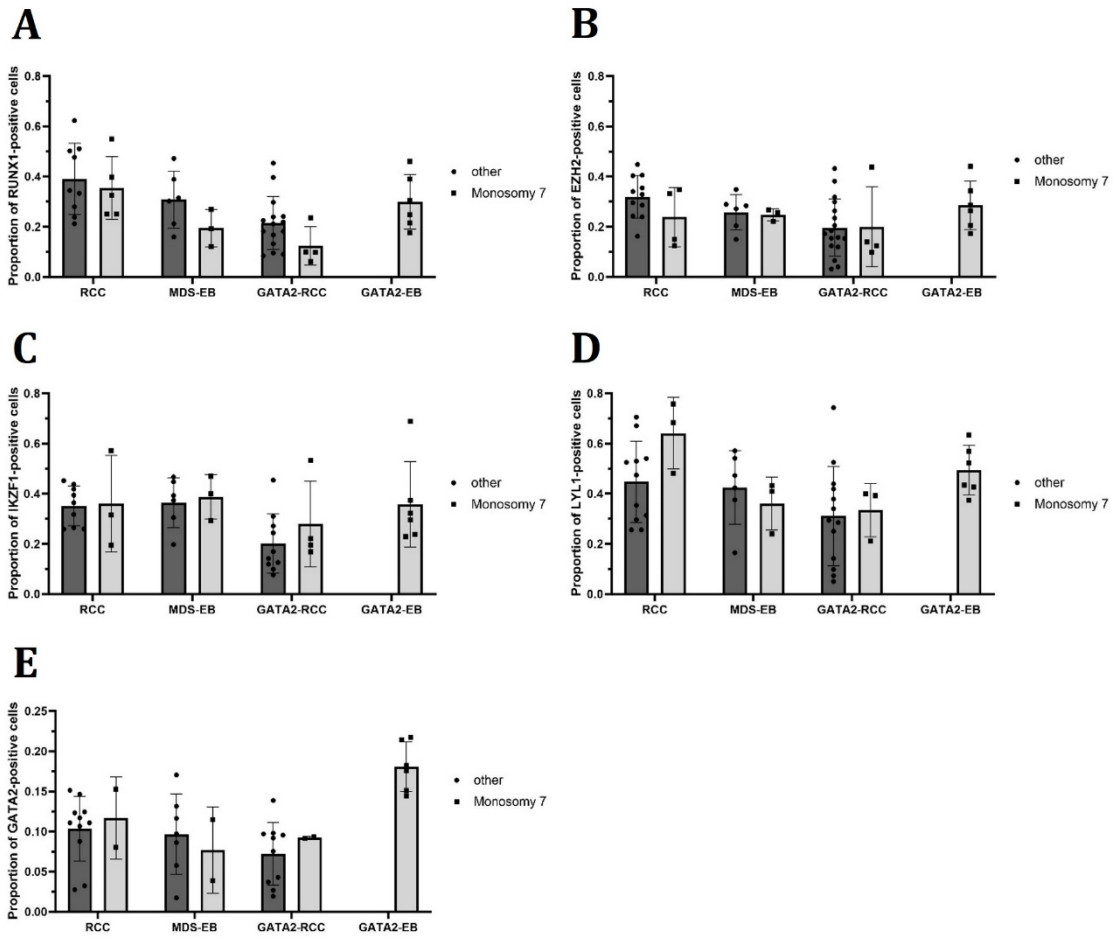

Figure D 5: mRNA expression patterns of *GATA2* and its target genes within the bone marrow. Cell quantification is shown for GATA2 targets *RUNX1* **(A)**, *EZH2* **(B)**, *IKZF1* **(C)**, *LYL1* **(D)** and *GATA2* itself **(E)** in relation to patient karyotypes.

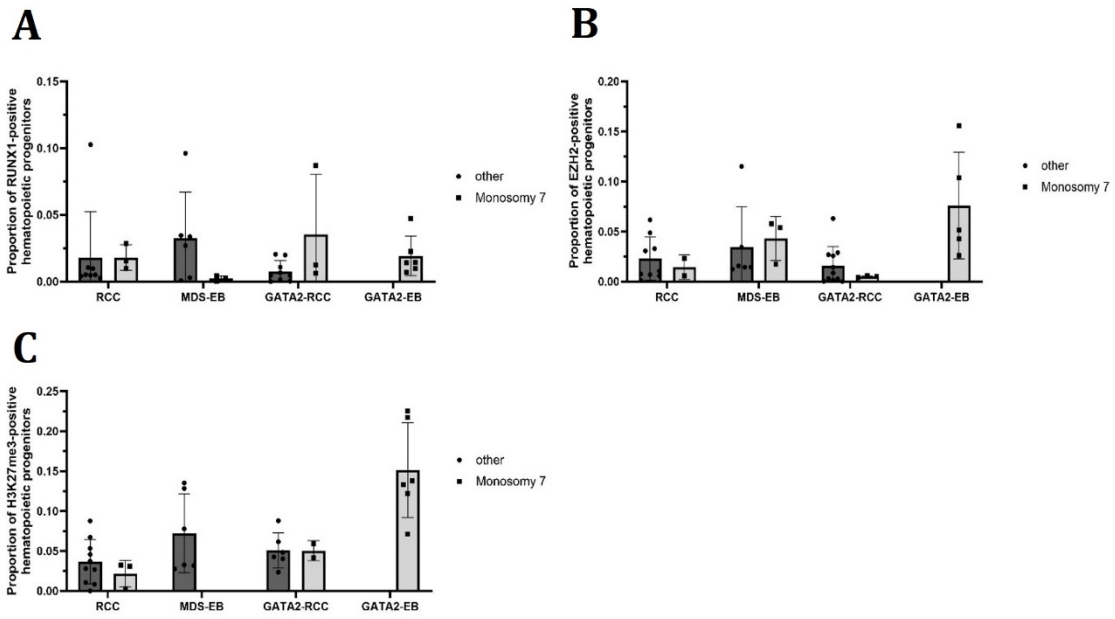

Figure D 6: Expression of GATA2 target genes *RUNX1* and *EZH2*, alongside the *EZH2*-dependent gene silencing mark H3K27me3 in hematopoietic progenitors. The figure presents the proportion of positive hematopoietic progenitors for mRNA expression of *RUNX1* **(A)**, and *EZH2* **(B)**, as well as protein expression of H3K27me3 **(C)** in CD34-positive cells.

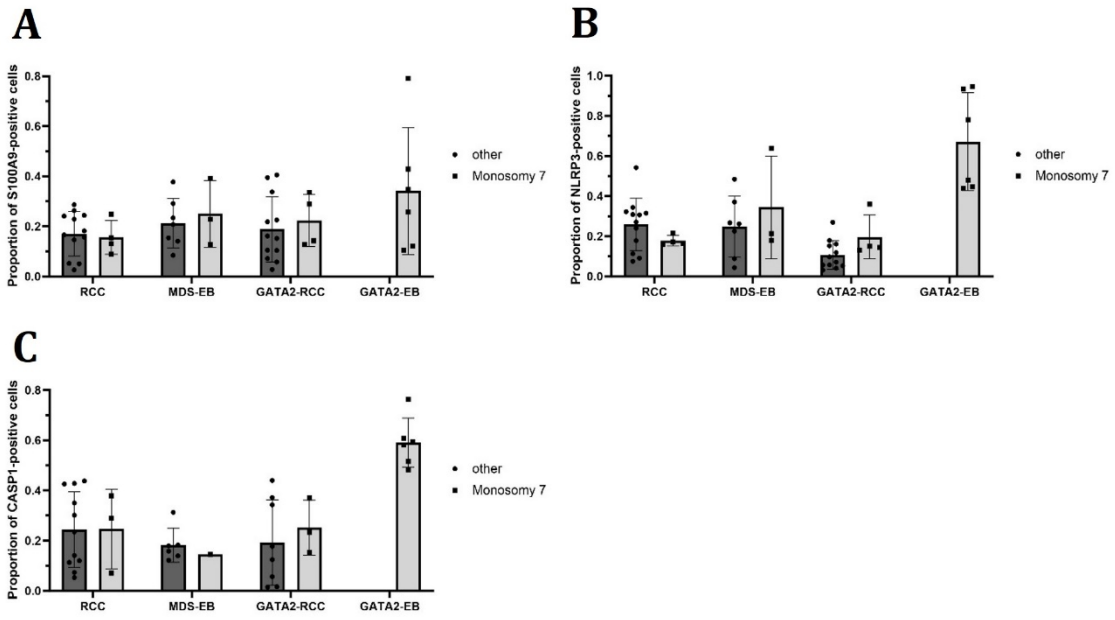

Figure D 7: Expression profiles of pivotal players in pyroptosis, illustrating karyotypic differences. Quantification of cells positive for S100A9 **(A)**, NLRP3 **(B)**, and CASP1 **(C)** in patients with monosomy 7 in comparison to other karyotypes.

Appendix E

Western Blot Analysis of KG-1 and K-562 Cells after PMA Stimulation

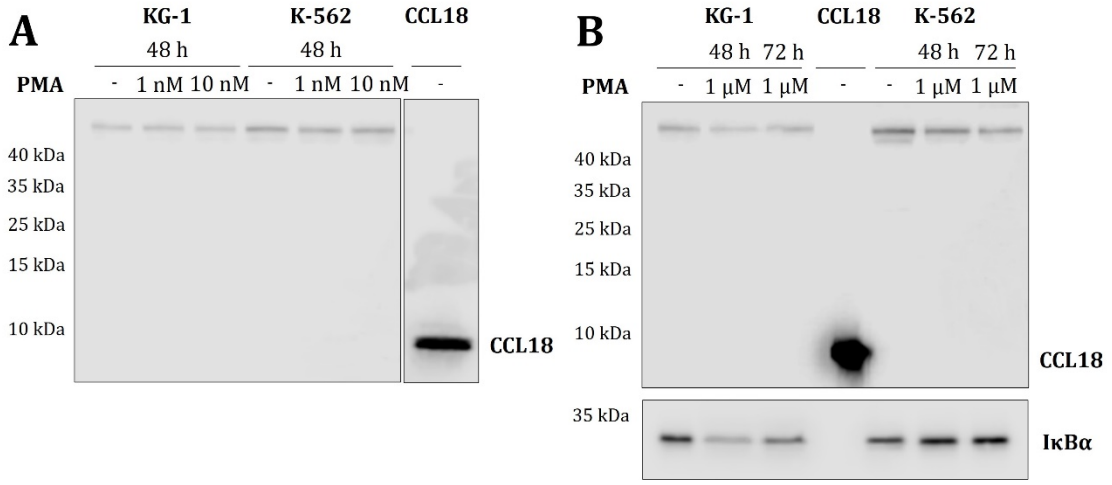

Figure E : Western blot analysis of KG-1 and K-562 cells subsequent to PMA stimulation for 48 h and 72 h. Unstimulated cells are denoted as - , while human recombinant CCL18 protein serves as positive control on 20% acrylamide gels. For cells stimulated with 1 nM or 10 nM PMA over 48 h **(A)**, no discernible CCL18 band of the anticipated size of 8 kDa is observed in either KG-1 or K-562 cells. Additionally, after 1 µM PMA stimulation for 48 h and 72 h **(B)**, no CCL18 is visualized when compared to the CCL18 protein control. The IκBα band is included as control for PMA stimulation.

Acknowledgements

I would like to express my deepest and sincere gratitude to my mentor Prof. Dr. Martina Rudelius for her invaluable guidance and encouragement throughout the years. Her patience and support, her knowledge and expertise, as well as her passion and commitment for her patients and for science have been a great inspiration for me, and taught me so many lessons to become the scientist I am now.

I would like to extend my sincere thanks to Prof. Dr. Andreas Jung, for supervision of my work at the Institute of Pathology at the Ludwig-Maximilians University Munich.

Additionally, I want to thank the “deutsche José Carreras Leukämie-Stiftung” for generous financial support for my research.

I am grateful for the productive scientific discussions from our EWOG-MDS collaborators and partners, and I would especially like to thank PD Dr. Miriam Erlacher for her dedication and support for the project.

This endeavour was fuelled by the consistent and powerful scientific, technical and social support of my colleagues Guido Piontek and Yuki Schneider-Kimoto. My heartfelt thanks for their sincerity and friendship, which greatly enhanced my time in the lab and made it truly memorable.

I would like to thank my parents, Brigitte and Franz Schreiber, from the bottom of my heart. Their unwavering support and strong belief in me has carried me through all these years.

Finally, to my husband, Niklas Teichert: words can hardly express the depth of my love. Thank you for being my source of strength, without you this journey would not have been possible.

LMU LUDWIG-MAXIMILIANS-UNIVERSITÄT MÜNCHEN

Dekanat Medizinische Fakultät
Promotionsbüro

Affidavit

Schreiber-Teichert, Franziska Elisabeth

Surname, first name

I hereby declare, that the submitted thesis entitled

Phenomics and Transcriptomics of the Hematopoietic Niche for Understanding Malignant Transformation in GATA2 Deficiency

is my own work. I have only used the sources indicated and have not made unauthorised use of services of a third party. Where the work of others has been quoted or reproduced, the source is always given.

I further declare that the dissertation presented here has not been submitted in the same or similar form to any other institution for the purpose of obtaining an academic degree.

Munich, 05 February 2026

Place, Date

Franziska Elisabeth Schreiber-Teichert

Signature doctoral candidate

LMU LUDWIG-MAXIMILIANS-UNIVERSITÄT MÜNCHEN

Dekanat Medizinische Fakultät
Promotionsbüro

Confirmation of congruency between printed and electronic version of the doctoral thesis

Doctoral candidate: Franziska Elisabeth Schreiber-Teichert

Address: Thalkirchner Str. 36, 80337 Munich

I hereby declare that the electronic version of the submitted thesis, entitled

Phenomics and Transcriptomics of the Hematopoietic Niche for Understanding Malignant Transformation in GATA2 Deficiency

is congruent with the printed version both in content and format.

Munich, 05 February 2026 — Franziska Elisabeth Schreiber-Teichert

Place, Date — Signature doctoral candidate

List of Publications

Molnar, C., Rajak, J., Weiss, J. M., Gonzalez-Menendez, I., Andrieux, G., **Schreiber, F.,** Kornemann, E. M., Wendeburg, L., Göhring, G., Strahm, B., Beier, F., Steinemann, D., Börries, M., Rudelius, M., Quintanilla-Martinez, L., Niemeyer, C. M., Niewisch, M. R., Labi, V., Bohler, S., & Erlacher, M. (2026). PUMA-induced apoptosis drives bone marrow failure and genomic instability in telomerase-deficient mice. ***Cell death and differentiation***, *33*(1), 38–50.

Schreiber, F., Piontek, G., Schneider-Kimoto, Y., Schwarz-Furlan, S., De Vito, R., Locatelli, F., Gengler, C., Yoshimi, A., Jung, A., Klauschen, F., Niemeyer, C. M., Erlacher, M. & Rudelius, M. (2023). Development of MDS in pediatric patients with GATA2 deficiency: Increased histone trimethylation and deregulated apoptosis as potential drivers of transformation. ***Cancers***, *15*(23), 5594.

Reha Dodurgali, M., Coll- Fernández, R., Queiroz Petrus, F., Kawano, M., **Schreiber, F.**, De Lima Froio, N., Lacerda, G., Lopez, E., Martins, A., Flores Flores, A., Machado, B., Soares dos Santos, B., Parron, B., Tapia Argudo, C., Dos Santos Barros, C., Stephan, C., Bouzas Rodeiro, D., Mucci, G., Carvajal Acosta, J. A., Rabelo Laporte, L., De Leon Benedetti, L., Morales Ojeda, L., Raso Bastos, P., Villalobos, R., Trindade Gomes da Silva, V., Haseeb, A., Gasparoto Pereira Valério, M., Junqueira Moll-Bernardes, R., Ferreira de Freitas Euzébio, R., Rangel Olivera, G., Dos Santos Kasai, C., Minisha, F. & Silva Godinez, J. C. (2023). Effects of neuromuscular electrical stimulation in patients with post-stroke related dysarthria: A double-blinded, phase-II randomized sham-controlled trial protocol – ULYSSES trial. ***Principles and practice of clinical research***, *9*(2).

Schreiber, F., De Lima Froio, N., Coll-Fernández, R., Queiroz Petrus, F., Soares dos Santos, B., Flores Flores, A., Morales Ojeda, L., De Leon Benedetti, L., Trindade Gomes da Silva, V., Reha Dodurgali, M., Dos Santos Barros, C., Barros Parron Fernandes, B., Tapia Argudo, C., Stephan, C. & Buffone, F. (2023). Neuromuscular electrical stimulation for dysphonia and dysarthria: A systematic review. ***Principles and practice of clinical research***, *8*(4).

Paul, T., Ledderose, S., Bartsch, H., Sun, N., Soliman, S., Märkl, B., Ruf, V., Herms, J., Stern, M., Keppler, O. T., Delbridge, C., Müller, S., Piontek, G., Schneider-Kimoto, Y., **Schreiber, F.**, Williams, T. A., Neumann, J., Knösel, T., Schulz, H., Spallek, R., Graw, M., Kirchner, T., Walch, A. & Rudelius, M. (2022). Adrenal tropism of SARS-CoV-2 and

adrenal findings in a post-mortem case series of patients with severe fatal COVID-19. ***Nature communications***, *13*(1), 1589.

Schludi, M. H., Becker, L., Garrett, L., Gendron, T. F., Zhou, Q., **Schreiber, F.**, Popper, B., Dimou, L., Strom, T. M., Winkelmann, J., von Thaden, A., Rentzsch, K., May, S., Michaelsen, M., Schwenk, B. M., Tan, J., Schoser, B., Dieterich, M., Petrucelli, L., Hölter, S. M., Wurst, W., Fuchs, H., Gailus-Durner, V., De Angelis, M. H., Klopstock, T., Arzberger, T. & Edbauer, D. (2017). Spinal poly-GA inclusions in a C9orf72 mouse model trigger motor deficits and inflammation without neuron loss. ***Acta neuropathologica***, *134*(2), 241–254.

Zhou, Q., Lehmer, C., Michaelsen, M., Mori, K., Alterauge, D., Baumjohann, D., Schludi, M. H., Greiling, J., Farny, D., Flatley, A., Feederle, R., May, S., **Schreiber, F.**, Arzberger, T., Kuhn, C., Klopstock, T., Hermann, A., Haass, C., & Edbauer, D. (2017). Antibodies inhibit transmission and aggregation of *C9orf72* poly-GA dipeptide repeat proteins. ***EMBO molecular medicine***, *9*(5), 687–702.

Schwenk, B. M., Hartmann, H., Serdaroglu, A., Schludi, M. H., Hornburg, D., Meissner, F., Orozco, D., Colombo, A., Tahirovic, S., Michaelsen, M., **Schreiber, F.**, Haupt, S., Peitz, M., Brüstle, O., Küpper, C., Klopstock, T., Otto, M., Ludolph, A. C., Arzberger, T., Kuhn, P. H. & Edbauer, D. (2016). TDP-43 loss of function inhibits endosomal trafficking and alters trophic signaling in neurons. ***The EMBO journal***, *35*(21), 2350–2370.

Müller, C., Hemmers, S., **Schreiber, F.**, Körner, A., Mirakaj, V., Giera, M., & Bracher, F. (2016). A new class of selective and potent inhibitors of human Δ^{24} dehydrocholesterol reductase. Poster presented at the Annual Meeting of the German Pharmaceutical Society (DPhG), Munich, Germany.

Conference Presentations

"Pediatric MDS in GATA2 deficiency: Enhanced histone trimethylation and deregulated apoptosis as driver?"

Conference: 10th International Symposium on MDS and SAA in Childhood
Date: September 2023
Role: Presenter
Location: Museu da Electricidade, Lisbon, Portugal

Munich, 05 February 2026 — Franziska Elisabeth Schreiber-Teichert

Place, Date — Signature doctoral candidate